Collective phenomena in (multi)strange-hadron production at high μ_B: performance of the CBM experiment at FAIR

Dissertation
zur Erlangung des Doktorgrades
der Naturwissenschaften

vorgelegt beim Fachbereich Physik
der Johann Wolfgang Goethe-Universität
in Frankfurt am Main

von
Oleksii Lubynets
aus Kramatorsk, Ukraine

Frankfurt am Main 2024
D30

vom Fachbereich Physik der

Johann Wolfgang Goethe-Universität als Dissertation angenommen.

Dekan: Prof. Dr. Roger Erb

Betreuer: Dr. Ilya Selyuzhenkov
Gutachter: Prof. Dr. Christoph Blume
Apl. Prof. Dr. Peter Senger

Datum der Disputation: 18. April 2024

Abstract

The strong force is one of the four fundamental interactions, and the theory of it is called Quantum Chromodynamics (QCD). A many-body system of strongly interacting particles (QCD matter) can exist in different phases depending on temperature (T) and baryonic chemical potential (μ_B). The phases and transitions between them can be visualized as $\mu_B - T$ phase diagram. Extraction of the properties of the QCD matter, such as compressibility, viscosity and various susceptibilities, and its Equation of State (EoS) is an important aspect of the QCD matter study. In the region of near-zero baryonic chemical potential and low temperatures the QCD matter degrees of freedom are hadrons, in which quarks and gluons are confined, while at higher temperatures partonic (quarks and gluons) degrees of freedom dominate. This partonic (deconfined) state is called quark-gluon plasma (QGP) and is intensively studied at CERN and BNL. According to lattice QCD calculations at $\mu_B = 0$ the transition to QGP is smooth (cross-over) and takes place at $T \approx 156\,\mathrm{MeV}$. The region of the QCD phase diagram, where matter is compressed to densities of a few times normal nuclear density (μ_B of several hundreds MeV), is not accessible for the current lattice QCD calculations, and is a subject of intensive research. Some phenomenological models predict a first order phase transition between hadronic and partonic phases in the region of $T \lesssim 100\,\mathrm{MeV}$ and $\mu_B \gtrsim 500\,\mathrm{MeV}$. Search for signs of a possible phase transition and a critical point or clarifying whether the smooth cross-over is continuing in this region are the main goals of the near future explorations of the QCD phase diagram.
In the laboratory a scan of the QCD phase diagram can be performed via heavy-ion collisions. The region of the QCD phase diagram at $T \gtrsim 150\,\mathrm{MeV}$ and $\mu_B \approx 0$ is accessible in collisions at LHC energies ($\sqrt{s_{NN}}$ of several TeV), while the region of $T \lesssim 100\,\mathrm{MeV}$ and $\mu_B \gtrsim 500\,\mathrm{MeV}$ can be studied with collisions at $\sqrt{s_{NN}}$ of a few GeV. The QCD matter created in the overlap region of colliding nuclei (fireball) is rapidly expanding during the collision evolution. In the fireball there are strong temperature and pressure gradients, extreme electromagnetic fields and an exchange of angular momentum and spin between the system constituents. These effects result in various collective phenomena. Pressure gradients and the scattering of particles, together with the initial spatial anisotropy of the density distribution in the fireball, form an anisotropic

flow - a momentum (azimuthal) anisotropy in the emission of produced particles. The correlation of particle spin with the angular momentum of colliding nuclei leads to a global polarization of particles. A strong initial magnetic field in the fireball results in a charge dependence and particle-antiparticle difference of flow and polarization.

Anisotropic flow is quantified by the coefficients v_n from a Fourier decomposition of the azimuthal angle distribution of emitted particles relative to the reaction plane spanned by beam axis and impact parameter direction. The first harmonic coefficient v_1 quantifies the directed flow - preferential particle emission either along or opposite to the impact parameter direction. The v_1 is driven by pressure gradients in the fireball and thus probes the compressibility of the QCD matter. The change of the sign of v_1 at $\sqrt{s_{NN}}$ of several GeV is attributed to a softening of the EoS during the expansion, and thus can be an evidence of the first order phase transition. The global polarization coefficient P_H is an average value of the hyperon's spin projection on the direction of the angular momentum of the colliding system. It probes the dynamics of the QCD matter, such as vorticity, and can shed light on the mechanism of orbital momentum transfer into the spin of produced particles.

In collisions at $\sqrt{s_{NN}}$ of several GeV, which probe the region of the QCD phase diagram at $T \lesssim 100\,\mathrm{MeV}$ and $\mu_B \gtrsim 500\,\mathrm{MeV}$, hadron production is dominated by u and d quarks. Hadrons with strange quarks are produced near the threshold, what makes their yields and dynamics sensitive to the density of the fireball. Thus measurement of flow and polarization, in particular of (multi-)strange particles, provides experimental constraints on the EoS, that allows to extract transport coefficients of the QCD matter from comparison of data with theoretical model calculations of heavy-ion collisions.

Experimental exploration of the QCD phase diagram in the region of $T \lesssim 100\,\mathrm{MeV}$ and $\mu_B \gtrsim 500\,\mathrm{MeV}$ is currently being performed by the HADES experiment at SIS-18 and STAR FXT at RHIC. The Compressed Baryonic Matter (CBM) experiment at the Facility of Antiproton and Ion Research (FAIR) will perform such exploration in the near future. The CBM is a fixed target experiment which will study heavy-ion collisions at $\sqrt{s_{NN}} = 2.9 - 4.9\,\mathrm{GeV}$. Multidifferential measurements of yields and especially of azimuthal modulations (flow) of rarely produced multi-strange hadrons require large statistics. They will become available with CBM due to its peak interaction rate of $10^7\,\mathrm{Hz}$, which is by $2 - 3$ orders of magnitude higher than at current experiments.

The current doctoral work is devoted to the CBM performance for measurements of anisotropic flow and global polarization of $\Lambda, \bar{\Lambda}$ and multistrange Ξ^- hyperons. As a part of this thesis work a software package PFSimple, based on Kalman Filter Particle mathematics, was developed for the reconstruction and selection of weak decays. Using PFSimple and Geant4 Monte-Carlo (MC) simulations it was demonstrated that the CBM acceptance for (anti-)Λ and Ξ^- baryons covers both, mid- and forward- rapidity $y \in (0 - 1)$, and a transverse momentum range $p_T \in (0 - 1.5)\,\mathrm{GeV}/c$ with high signal-to-background ratio for Ξ^- ($S/B \approx 15$) and Λ ($S/B \approx 5$). The reduction of systematic uncertainties of flow measurements, associated with the symmetry of v_n, is possible with the CBM acceptance coverage of backward rapidity region, which is the largest at $\sqrt{s_{NN}} = 4.9\,\mathrm{GeV}$. The reconstruction efficiency for Ξ^- (Λ and $\bar{\Lambda}$ with the same selection) reaches values of 20% (50%), with a maximum shifting from $y \approx 0$ at $\sqrt{s_{NN}} = 4.9\,\mathrm{GeV}$ to $y \approx 1$ at $\sqrt{s_{NN}} = 2.9\,\mathrm{GeV}$.

An estimation of the reaction plane for flow and polarization measurements in CBM is done using nucleons not participating in the collision (spectators), registered with the Projectile Spectator Detector (PSD). The QnTools framework, which implements procedures to correct for event plane resolution and detector non-uniformity, was used for flow calculation. It was extended within this thesis with an invariant mass fit method for the flow extraction which employs the subtraction of the combinatorial background contribution. The developed analysis procedure was validated with the flow of Λ-baryons and K^0_S-mesons as the most abundant strange hadrons.

In this work the performance of the CBM experiment for the measurement of directed flow and global polarization of Λ, $\bar{\Lambda}$, Ξ^--baryons is quantified. Directed flow of Λ and Ξ^- was extracted using data-driven procedures multidifferentially in transverse momentum, rapidity and centrality classes for different collision energies. A realistic model of heavy-ion collision and Geant4 transport through CBM material was used. It was demonstrated that reconstructed values reproduce the MC input within 2 standard deviations in the rapidity range $y \in$ (-0.5 $-$ 0.7), the agreement between evaluated and MC-true values is the best in 10$-$40% central events. Systematic uncertainties originate from correlations not related to the geometry of the collision, such as short-range correlations, resonance decays and global momentum conservation. Projections of statistical uncertainties for directed flow and global polarization of Ξ^- and (anti-)Λ-baryons were calculated using thermal model predictions for particle yields. The conclusion from the evaluation of statistical and systematic uncertainties is that directed flow data from high-rate operation of CBM in the first few years ($\approx 10^{13}$ events in 20 days), will allow to discriminate between models implementing EoS with and without first order phase transition. Also measurements of the particle-antiparticle difference of flow and polarization will be possible, which are needed to quantify effects of the magnetic field in the fireball.

Kurzfassung

Die starke Kraft ist eine der vier fundamentalen Wechselwirkungen und wird durch die Theorie der Quantenchromodynamik (QCD) beschrieben. Ein Vielteilchensystem aus stark wechselwirkenden Teilchen (QCD Materie) kann in verschiedenen Phasen existieren, abhängig von der Temperatur (T) und dem baryo-chemischen Potential (μ_B). Diese Phasen sowie die Übergänge zwischen ihnen können im $\mu_B - T -$Phasendiagramm dargestellt werden. Wichtige Aspekte beim Studium der QCD Materie sind ihre Zustandsgleichung (EoS vom englischen *equation of state*) sowie weitere Eigenschaften, wie die Kompressibilität, Viskosität und verschiedene Suszeptibilitäten. Im Bereich verschwindend geringem baryo-chemischen Potentials und niedriger Temperatur sind die Freiheitsgrade der QCD Materie die Hadronen, in welchen die Quarks und Gluonen gebunden sind, während bei höheren Temperaturen die partonischen Freiheitsgrade (Quarks und Gluonen) dominieren. Dieser partonische (asymptotisch-freie) Zustand nennt sich Quark-Gluon-Plasma (QGP) und wird intensiv am CERN und BNL untersucht. Gitter-QCD Berechungen zufolge ist der Phasenübergang zum QGP für $\mu_B = 0$ kontinuierlich (Crossover) und tritt bei $T \approx 156\,\mathrm{MeV}$ auf. Die Region des QCD Phasendiagramms, wo die Materie bis zu einem Vielfachen der normalen nuklearen Dichte komprimiert wird (μ_B von mehreren hundert MeV), ist für die aktuellen Gitter-QCD Berechnungen unzugänglich und Gegenstand intensiver Forschung. Einige phänomenologischen Modelle sagen einen Phasenübergang erster Ordnung zwischen der hadronischen und der partonischen Phase im Bereich von $T \lesssim 100\,\mathrm{MeV}$ und $\mu_B \gtrsim 500\,\mathrm{MeV}$ vorher. Die Suche nach Hinweisen auf einen möglichen Phasenübergang sowie kritischen Punkt oder die Klärung eines sich in diese Region fortsetzenden, kontinuierlichen Crossovers, sind die primären Ziele der zukünftigen Erforschung des QCD Phasendiagramms. Ein Scan des QCD Phasendiagramms kann im Labor mittels Schwerionenkollisionen durchgeführt werden. Der Bereich des QCD Phasendiagramms von $T \gtrsim 150\,\mathrm{MeV}$ und $\mu_B \approx 0$ ist durch Kollisionen von LHC Energien ($\sqrt{s_{NN}}$ von einigen TeV) zugänglich, während der Bereich von $T \lesssim 100\,\mathrm{MeV}$ und $\mu_B \gtrsim 500\,\mathrm{MeV}$ durch Kollisionen von einigen GeV $\sqrt{s_{NN}}$ erforscht werden kann. Die in der Überlappungsregion der kollidierenden Atomkerne (Feuerball) erzeugte QCD Materie dehnt sich rapide während der Evolution der Kollision aus. Im Feuerball entstehen hohe Tem-

peraturen und Druckgradienten sowie extreme magnetische Felder und ein Austausch von Drehimpuls und Spin zwischen den Konstituenten des Systems findet statt. Aus diesen Effekten resultieren verschiedene kollektive Phänomene. Druckgradienten und die Streuung von Teilchen, zusammen mit der anfänglichen räumlichen Anisotropie der Dichteverteilung des Feuerballs, verursacht einen anisotropen kollektiven Fluss - eine (azimuthale) Impulsanisotropie in der Emission der erzeugten Teilchen. Die Korrelation der Teilchenspins mit dem Drehimpuls der kollidierenden Atomkerne führt zu einer globalen Spinpolarization der Teilchen. Ein anfänglich starkes magnetisches Feld im Feuerball generiert einen ladungs- und Teilchen-Antiteilchen abhängigen Unterschied des Flusses und der Polarisation.

Der anisotropische Fluss wird durch die Koeffizienten v_n einer Fourierreihenentwicklung der azimuthalen Winkelverteilung der emittierten Teilchen relativ zur Reaktionebene, welche durch die Richtung der Strahlachse und des Stoßparameters aufgespannt wird, beschrieben. Der erste harmonische Koeffizient v_1 misst den direkten Fluss - bevorzugte Teilchenemission entweder entlang oder entgegen der Richtung des Stoßparameters. v_1 wird maßgeblich durch die Druckgradienten im Feuerball bestimmt und ist daher sensitiv zur Kompressibilität der QCD Materie. Der Vorzeichenwechsel von v_1 im Bereich von einem GeV $\sqrt{s_{NN}}$, wird einem Aufweichen des EoS während der Expansion zugeschrieben und kann deshalb ein Hinweis auf einen Phasenübergang erster Ordnung sein. Der Koeffizient der globalen Polarisation P_H ist ein gemittelter Wert der Projektion des Hyperonenspins auf den Drehimpuls des kollidierenden Systems. Er untersucht die Dynamik der QCD Materie, wie die Vortizität und kann Licht ins Dunkel bringen, was den Mechanismus des Bahndrehimpulsübertrags auf den Spin erzeugter Teilchen angeht.

In Kollisionen von einigen GeV $\sqrt{s_{NN}}$, welche den Bereich des QCD Phasendiagramms $T \lesssim 100\,\mathrm{MeV}$ und $\mu_B \gtrsim 500\,\mathrm{MeV}$ untersuchen, wird die Hadronenproduktion von u- und d-Quarks dominiert. Hadronen, die ein seltsames Quark enthalten, werden nahe ihrer Produktionsschwelle erzeugt, wodurch ihre Anzahl und Dynamik sensitiv zur Dichte des Feuerballs wird. Folglich liefern Messungen von Fluss und Polarisation, insbesondere von (mehrfach-)seltsamen Teilchen, experimentelle Einschränkungen der EoS, was die Extraktion von Transportkoeffizienten der QCD Materie durch Vergleich der Daten mit theoretischen Modellrechnungen der Schwerionenkollisionen ermöglicht.

Die experimentelle Untersuchung des QCD Phasendiagramms im Bereich von $T \lesssim 100\,\mathrm{MeV}$ und $\mu_B \gtrsim 500\,\mathrm{MeV}$ wird aktuell durch das HADES Experiment am SIS-18 und das STAR FXT Experiment am RHIC durchgeführt. Das *Compressed Baryonic Matter* (CBM) Experiment an der internationalen Teilchenbeschleunigeranlage FAIR wird diese Untersuchung in naher Zukunft fortsetzen. Das CBM ist ein Experiment mit festem Ziel, welches Schwerionenkollisionen von $\sqrt{s_{NN}} = 2.9 - 4.9\,\mathrm{GeV}$ studieren wird. Multi-differentielle Messungen von Teilchenanzahl und insbesondere azimuthalen Modulationen (Flow) von selten produzierten, mehrfach-seltsamen Hadronen bedürfen hoher Statistik. Dies wird mit CBM möglich, aufgrund seiner maximalen Interaktionsrate von 10^7 Hz, was $2-3$ Größenordnungen über denen aktueller Experimente liegt. Die vorliegende Doktorarbeit widmet sich der Leistungsfähigkeit von CBM, Messungen von anisotropischen Fluss und globaler Polarisation von $\Lambda, \bar{\Lambda}$ sowie mehrfach-seltsamen Ξ^- Hyperonen durchzuführen. Als Teil dieser Arbeit wurde das Softwarepaket PFSimple für die Rekonstruktion und Selektion von schwach zerfallenden Teilchen entwickelt, welches auf der Mathematik von Kalman Filter Teilchen basiert. Unter Verwendung von PFSimple und Geant4 Monte-Carlo (MC) Simulationen wurde gezeigt, dass die CBM Akzeptanz für (Anti-)Λ und Ξ^--Baryonen sowohl die mittlere, also auch die vorwärtsgerichtete Rapidität $y \in (0-1)$ und einen transversale Impulsbereich von $p_T \in (0-1.5)\,\mathrm{GeV}/c$ mit hohem Signal-zu-Untergrund Verhältnis für Ξ^- $(S/B \approx 15)$ und Λ $(S/B \approx 5)$ abdeckt. Die Reduktion systematischer Unsicherheiten der Flowmessungen verbunden mit der Symmetrie der v_n ist möglich mit der CBM Akzeptanzabdeckung des rückwärtigen Rapiditätsbereich, welcher bei $\sqrt{s_{NN}} = 4.9\,\mathrm{GeV}$ am größten ist. Die Rekonstruktionseffizienz für Ξ^- (Λ und gleiche Selektion für $\bar{\Lambda}$) erreicht Werte von 20 % (50 %), wobei sich das Maximum von $y \approx 0$ bei $\sqrt{s_{NN}} = 4.9\,\mathrm{GeV}$ zu $y \approx 1$ bei $\sqrt{s_{NN}} = 2.9\,\mathrm{GeV}$ verschiebt.

Eine Abschätzung der Reaktionsebene für Fluss- und Polarisationsmessungen wird in CBM durch jene Nukleonen vorgenommen, welche nicht an der Kollision beteiligt sind (Spektatoren), verzeichnet durch den *Projectile Spectator Detektor* (PSD). Für die Flowberechnung wurde das QnTools Paket verwendet, welches das Verfahren zur Korrektur der Auflösung der Eventebene und Ungleichmäßigkeiten im Detektor implementiert. Im Rahmen dieser Arbeit wurde die Software um die Methode des invarianten Massenfits zur Extrahierung der Flowkoeffizienten erweitert, mit welcher sich der kombinatorische Untergrund abziehen lässt. Das entwickelte Analyseverfahren wurde mittels Fluss der am häufigsten auftretenden Teilchen der Λ-Baryonen und K^0_S-Mesonen validiert.

In dieser Arbeit wird die Leistungsfähigkeit des CBM Experiments im Bezug auf die Messungen von direktem Fluss und globaler Polarisation von $\Lambda, \bar{\Lambda}, \Xi^-$-Baryonen quantifiziert. Der direkte Fluss von Λ und Ξ^- wurde mittels eines datengetriebenen Verfahrens, multi-differentiell im Bezug auf den transversalen Impuls, die Rapidität und die Zentralitätsklasse für unterschiedliche Kollisionsenergien extrahiert. Ein realistisches Modell der Schwerionenkollisionen und Geant4 zum Transport durch das CBM Material wurde verwendet. Es wurde gezeigt, dass die rekonstruierten Werte den MC Eingangswert innerhalb zweier Standardabweichungen im Rapiditätsbereich von $y \in$ (-0.5 $-$ 0.7) reproduzieren, wobei die genauste Übereinstimmung der rekonstruierten mit den wahren (MC) Werten in zentralen Kollisionen von $10-40$ % auftrat. Die systematischen Unsicherheiten beruhen auf Korrelationen, die nicht mit der Kollisionsgeometrie zusammenhängen, wie kurz-reichweitige Korrelationen, Zerfälle von Resonanzen und globaler Impulserhaltung. Eine Hochrechnung der statistischen Unsicherheiten für den direkten Fluss und die globale Polarisation von Ξ^- und (Anti-)Λ-Baryonen wurde durch Vorhersagen thermischer Modelle für die Teilchenzahlen berechnet. Die Schlussfolgerung der Bestimmung statistischer und systematischer Unsicherheiten ist, dass die Messungen des direkten Flusses durch die Operation von CBM bei hohen Kollisionsraten in den ersten Jahren ($\approx 10^{13}$ Events in 20 Tagen) eine Unterscheidung zwischen Modellen basierend auf einer EoS mit oder ohne Phasenübergang erster Ordnung erlauben wird. Zudem sind Messungen von Teilchen-Antiteilchen Unterschieden des Flusses und der Polarisation möglich, welche notwendig sind, um die Auswirkungen des magnetischen Feldes im Feuerball zu quantifizieren.

Contents

Chapter 1

Introduction

The Universe is a very complicated system, and only a small part of it is now known to the mankind. Only 4% of matter in the universe belongs to that type which we observe in everyday life. 22% belongs to the so-called *dark matter*, and we do not know almost anything about it. Indirect evidences indicate its presence and major role in the formation of galaxies and structures of them. The remaining 74% is *dark energy* which makes the universe to expand with acceleration despite the gravity and is even less known than dark matter.

Normal matter consists of atoms, that means in Greek language “indivisible”. However, it is not true. Atoms consist of a small nucleus and cloud of electrons around it. Nuclei, in their turn, consist of protons and neutrons named nucleons. Nucleons consist of quarks, which seem to be elementary, at least at the current level of our knowledge. One way to investigate matter around us is by observing it (passive approach) - optically or using modern equipment such as telescopes or gravitational waves detectors. But in this case we cannot influence the observed system - only wait when an interesting event happens. Another way (active approach) is to decompose matter into elements by introducing a huge amount of energy to it and observe what happens next. The smaller scales of matter one wants to explore, the higher energy is needed to be introduced to the system. This is done in high energy physics experiments when colliding particles. Another important side of investigation process is to make conclusions from the observations, build models and check their predictive power. A bright example of this is the discovery of the widely-known Higgs boson which was predicted several decades before.

1.1 Standard model and fundamental forces

The Standard Model of particle physics is the theory describing three of the four known fundamental forces (electromagnetic, weak and strong interactions - excluding gravity) in the universe and classifying all known elementary particles.

Particles in Standard Model

All elementary particles can be divided into two main groups, see Fig. 1.1: fermions with a half-integer spin and bosons with an integer spin.
Fermions are represented by quarks and leptons, and leptons in their turn can be charged or neutral. Both quarks and leptons are divided into flavors grouped into 3 generations, with a tendency of increasing mass with generation number:

- 1-st generation: up (u) and down (d) quarks, electron and electron neutrino;
- 2-nd generation: charm (c) and strange (s) quarks, muon and muon neutrino;
- 3-d generation: top (t) and bottom (b) quarks, tau-lepton and tau-neutrino.

Each of the fermion has its antiparticle - the particle with the same mass and lifetime, but opposite quantum numbers - electric charge, lepton number, baryon number, strangeness etc. u, c and t quarks have charge +2/3 and d, s and b quarks -1/3 in units of elementary charge. Also each quark can have one of so-called color charges: red, green or blue. Quarks never exist in a free state but form clusters named hadrons with integer electric charge and “white” color. This phenomenon is called confinement. Hadrons are divided into two groups:

- mesons: quark-antiquark pair (not necessarily of the same flavor) with charge -1, 0 or +1 and being “white” because of neutralizing color by anti-color;
- baryons: group of three quarks or antiquarks with charge -2, -1, 0, +1 or +2 and being “white” because of mixing red, green and blue into white.

Matter observed in everyday life consists of the fermions of first generation: nuclei contain protons (*uud*) and neutrons (*udd*) and are surrounded by electrons.

Bosons are those particles which are responsible for interaction. There are vector bosons with spin 1: gluon, photon, W and Z bosons. Gluon, photon and Z are truly neutral (particles are identical to their antiparticles), while W-boson can have charge +1 or -1. Gluons and photons are massless particles. There is also a scalar (with zero spin) Higgs boson - a quantum of the Higgs field which is responsible for masses of elementary particles (except of neutrinos). Also there is a hypothesis of graviton - a quantum of gravitational field. If it exists, it should be a massless tensor boson with spin 2.

Fundamental forces

All interactions between matter belong to one of four fundamental forces: strong, electromagnetic, weak and gravitational. They vary by relative intensity, characteristic radius of interaction and carriers.

Strong interaction is provided by gluons and it influences quarks, but not leptons. This is the force which keeps quarks together in hadrons and hadrons in nuclei as well. It is the strongest force among the four but has very small radius

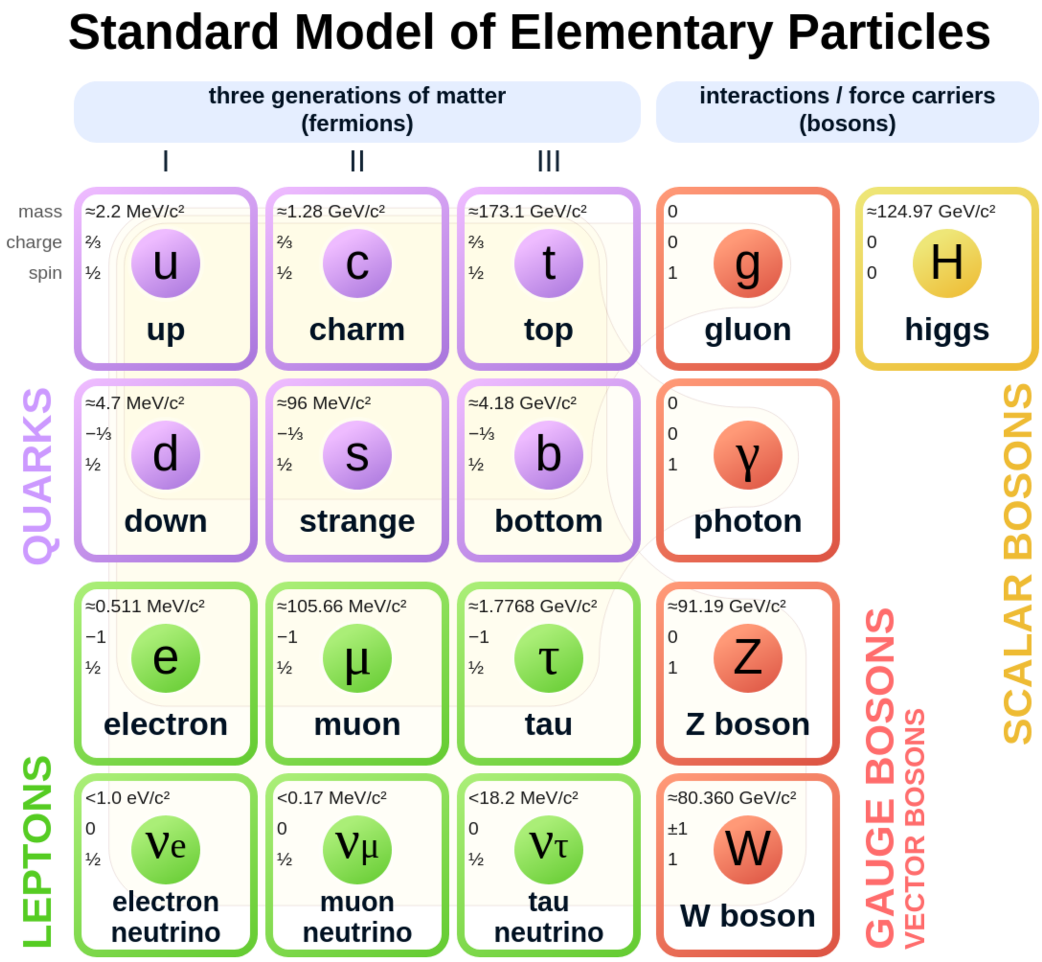

Figure 1.1: Particles of the Standard Model.

of interaction of about 10^{-15} m thus it is sometimes called “a giant with short arms”. Quark color plays a role of charge of the strong interaction. The branch of physics which studies strong interaction is called quantum chromodynamics (QCD).

Electromagnetic interaction is an interaction of particles with electric charge. The carrier of the electromagnetic interaction is a photon. Electromagnetic interaction is much weaker than strong interaction, but in contrast to the last it is a long range one. It keeps together nuclei and electrons forming atoms. Moreover, all chemical bonds of atoms inside molecules and even elastic forces observed in everyday life are provided by electromagnetic interaction.

Weak interaction has its name because it is much less intensive than both strong and electromagnetic interactions. It is responsible for some decays, one of the most well-known is β-decay. The carriers of the weak interaction are $W^{\pm}$ and Z^0 bosons, and it influences both quarks and leptons. A notable feature of the weak interaction discovered by famous madam Wu experiment [1] is that it can break parity. Weak interaction like strong one also has short range of about 10^{-18} m, and its "charge" is called weak isospin.

Gravitational interaction or just gravity is the weakest interaction, but it plays the most important role at large scales from planets to clusters of galaxies. It acts on all massive objects making them to attract to each other. Mass plays a role of "charge" for gravity. It is worth noting that gravity is not a part of the Standard Model, and its carrier, graviton, has not been discovered yet. Moreover, general relativity does not consider gravity as a force at all but as a deformation of space-time by massive objects.

There is a theory, developed by Weinberg, Salam and Glashow [2, 3, 4], which unites electromagnetic and weak interaction into a single one - electroweak. There are intensive attempts to build a common theory of electroweak and strong interaction but they have not succeed yet.

Table 1.1 summarizes fundamental forces and their main characteristics.

Standard Model is a self-consistent theory which describes the world of particles and interactions well and has a strong predictive power (it is worth noting that t-quark, $W^{\pm}$, Z^0 and Higgs bosons were predicted much earlier than discovered experimentally). However, it is not complete because it does not explain such phenomena as: baryonic asymmetry, gravity, neutrino mass generation, neutrino oscillations, dark matter and energy.

There is one more issue with the Standard Model which is not a shortcoming

Force	**Theory**	**Charge**	**Carrier**	**Relative strength**	**Radius, m**
Strong	Quantum chromodynamics	Color	Gluon	10^{38}	10^{-15}
Electromagnetic	Quantum electrodynamics	Electric charge	Photon	10^{36}	∞
Weak	Theory of weak interaction	Weak isospin	$W^{\pm}$ and Z^0 bosons	10^{33}	10^{-18}
Gravitational	General relativity	Mass	Graviton(?)	1	∞

Table 1.1: Fundamental forces: main characteristics.

but rather an evidence that people do not fully understand it: number of free parameters which is too large - 19. It can be that the actual number is lower, but some logic which stands behind them is not known yet.

1.2 Quantum chromodynamics

The strong interaction applies only to those particles which carry color charge, i.e. quarks and gluons. Theory describing this interaction is named quantum chromodynamics (QCD). The main features of the QCD theory are:

- Confinement - quarks do not exist in a free state but always clusterize into hadrons;
- Asymptotic freedom[1] - interaction between quarks becomes weaker at short distances and large energies;
- Chiral symmetry breaking which generates masses for hadrons far above the masses of the quarks, and makes pseudoscalar mesons light compared to vector mesons.

---

[1] It was discovered in 1973 by D. Gross, F. Wilczek [5] and independently by D. Politzer [6] and for this discovery they were awarded with Nobel Prize in 2004

The dynamics of the quarks and gluons is described by the Lagrangian:

$$\mathcal{L}_{QCD} = \sum_q \bar{\psi}_{q,i}(i\gamma^\mu (D_\mu)_{ij} - m_q \delta_{ij})\psi_{q,j} - \frac{1}{4} G^a_{\mu\nu} G^{\mu\nu}_a. \tag{1.1}$$

ψ is a spinor of quark, q denotes flavour and $i, j = \overline{1, 2, 3}$ denote color; γ^μ is a Dirac matrix; m_q is a quark mass; $(D_\mu)_{ij} = \partial_\mu \delta_{ij} - ig(T_a)_{ij} A^a_\mu$ is a gauge covariant derivative coupling the quark field with a coupling strength g, to the gluon fields A^a_μ via the infinitesimal SU(3) generators $T_a = \lambda_a/2$ where λ_a are Gell-Mann matrices with $a = \overline{1, ..., 8}$; $G^a_{\mu\nu} = \partial_\mu \mathcal{A}^a_\nu - \partial_\nu \mathcal{A}^a_\mu + g f^{abc} \mathcal{A}^b_\mu \mathcal{A}^c_\nu$ is the gauge invariant gluon field strength tensor, where f^{abc} are the structure constants of SU(3), $a, b, c = \overline{1, ..., 8}$.

The QCD theory cannot be solved analytically. Therefore various techniques have been developed to work with QCD:

- Perturbative QCD - an approach based on asymptotic freedom and making perturbation theory applicable to describe experiments at very high energies;
- Lattice QCD - an approach to reduce the analytically intractable path integrals of the continuum theory to numerical calculations in a discrete set of spacetime points (called the lattice);
- Effective theories for certain limits. They may be presented as expansions in some parameter of the QCD Lagrangian. An example is a chiral perturbation theory at low energies.

1.3 QCD phase diagram

Matter under those conditions and at those scales where the strong interaction plays major role and defines its behaviour, is called QCD matter. Depending on thermodynamic conditions, the many-body system of the QCD matter can

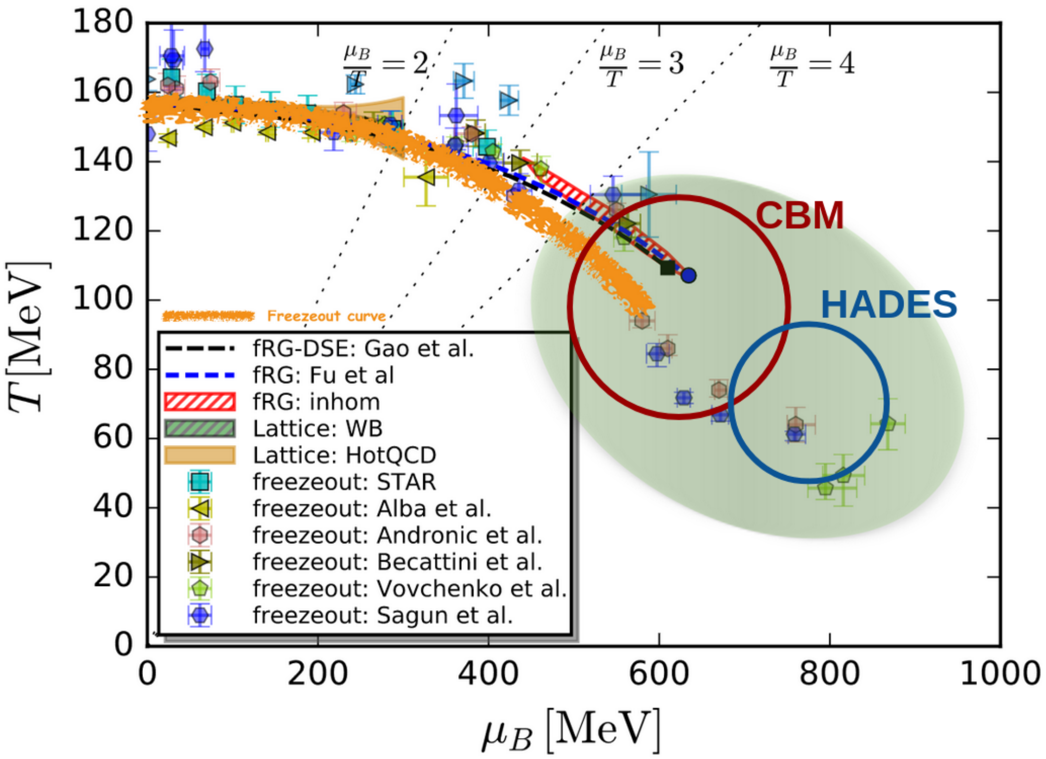

Figure 1.2: QCD matter phase diagram. Red and blue circles show area of CBM and HADES study respectively [7].

exist in different phases that is presented in a phase diagram, Fig. 1.2. On the horizontal axis there is baryonic chemical potential μ_B (which is proportional to net baryon density) while on the vertical axis temperature T is shown. At low T matter exists in the form of hadrons, mostly protons and neutrons. These are “usual” conditions - matter of that state surrounds us in everyday life. At temperatures around 150 MeV and near-zero baryon chemical potential (move upwards from the lower left corner) a smooth cross-over transition to quark and gluon degrees of freedom occurs as we know from lattice QCD calculations. It is schematically shown in Fig. 1.3, left. This state of matter is also known as quark-gluon plasma. It is assumed to exist in the early universe and is produced at high energy heavy-ion collisions (like LHC energies). When one increases both the temperature and net baryon density, the QCD matter also comes into deconfined state; but at some densities it happens in another way - not smoothly but possibly with phase transition, see Fig. 1.3, right. If there is a phase transition at high μ_B and cross-over at lower μ_B, there should exist a critical point separating these two regions. Neither phase transition nor critical point were discovered experimentally yet, and it is a part of the physics program of HADES and CBM experiments which allow to produce matter at high net baryon densities. Matter at high μ_B and low T exists in neutron stars. At even higher net baryon densities a color superconductivity is predicted (which is a QCD analogues of electrical superconductivity).

It is worth noting that QCD matter is characterized with more quantities besides temperature and baryonic chemical potential (e.g. isospin- or strangeness-chemical potential). In particular, in neutron stars an isospin chemical potential is different from that of symmetric nuclear matter. In a current representation of the QCD phase diagram a $\mu_B - T$ projection is considered.

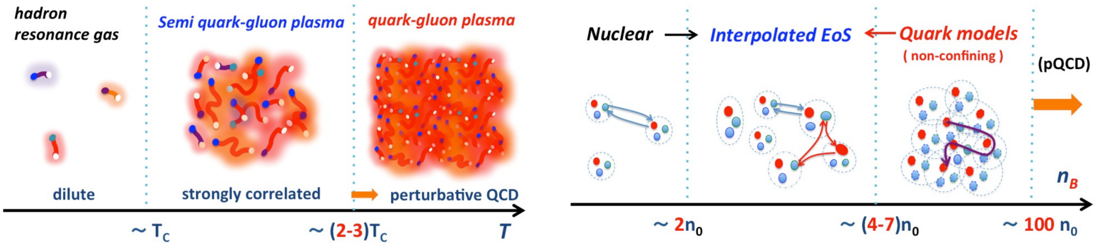

Figure 1.3: Schematic picture of (**left**) smooth crossover from the hadronic to quark-gluon plasma state with increasing temperature, (**right**) the transition from nuclear to deconfined quark matter with increasing density [8].

Each kind of matter, and QCD matter as well, is described with an Equation of State (EoS) - a relation between thermodynamic characteristics such as pressure, volume, temperature etc. Determination of EoS of different states of QCD matter is possible from observations of neutron stars, neutron stars mergers and heavy-ion collisions, see Fig. 1.4.

Conditions in physical systems are very different, see Tab. 1.2, that will allow to study QCD matter comprehensively.

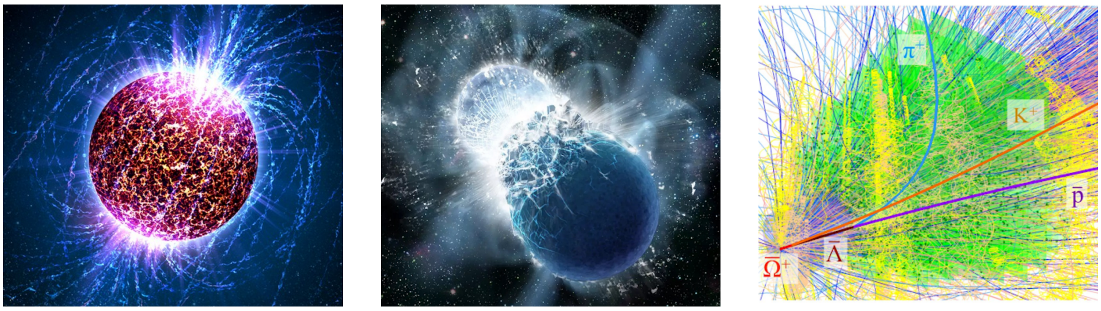

Figure 1.4: (**left**) neutron star [9], (**middle**) neutron star merger [10], (**right**) heavy-ion collision. Pictures are obtained from computer modeling.

	Neutron stars	**Neutron star mergers**	**Heavy-ion collisions**
Temperature, MeV	< 10	$10 - 100$	$100 - 150$
Density, ρ_0	< 10	$2 - 6$	$5 - 15$
Time, s	∞	10^{-5}	10^{-23}
Size, m	10^4	10^4	10^{-14}

Table 1.2: Macroscopic characteristics of processes with QCD matter. ρ_0 denotes normal nuclear density [11].

Neutron stars

There are a lot of theoretical hypotheses about neutron stars (NS) composition and corresponding EoS, see Fig. 1.5. According to the Tolman-Oppenheimer-Volkoff equation [12] mass and radius of a NS strongly depend on its EoS. Thus NS observation, in particular their radius and mass evaluation, allows to advocate for some of predictions and reject others. E.g. observation of the neutron star with a mass equal to 2 solar masses rules out the EoS which do not intersect the red band J1614-2230 in Fig. 1.5. The Neutron Star Interior Composition Explorer (NICER) at the International Space Station (ISS) is designed to provide simultaneous measurements of mass and radius of neutron stars [13]. Results obtained with NICER will add more experimental points on the mass-radius diagram in Fig. 1.5, right, and thus (dis-)approve some of the EoS predictions.

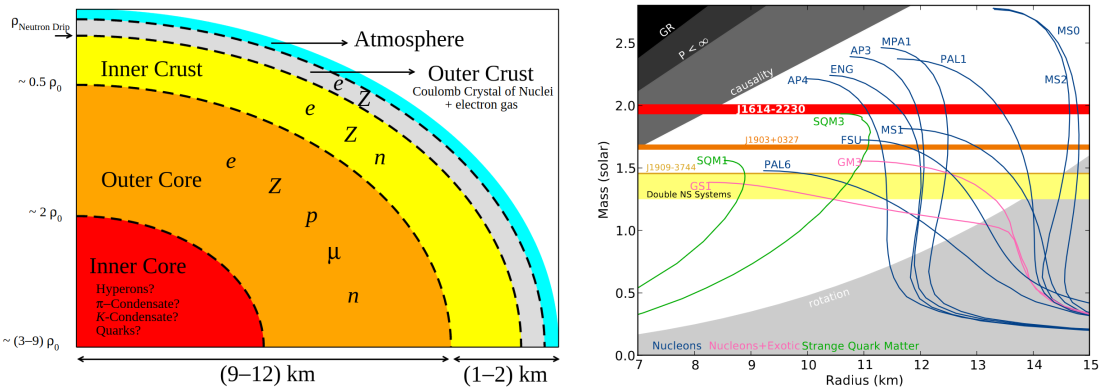

Figure 1.5: (**left**) Assumed structure and composition of a neutron star [14], (**right**) different EoSs predictions on NS mass-radius relation [15].

Neutron star mergers

First observation of gravitational waves generated by the merger of two black holes was done by LIGO and Virgo collaborations [16] in 2016; it opened a new era of multi-messenger astronomy. In 2017 the first gravitational waves caused by neutron stars merger were observed [17]. During a collision of two neutron stars a hot $(10 - 100\,\text{MeV})$ and dense $(2 - 6$ times normal nuclear density) medium is created. A simulation of the density and temperature of the medium created in a neutron star merger is shown in Fig. 1.6. The observation of the system evolution (prompt or delayed collapse to black hole or no collapse) with gravitational waves together with electromagnetic signals [18] allows to constrain the EoS of matter created in NS merger.

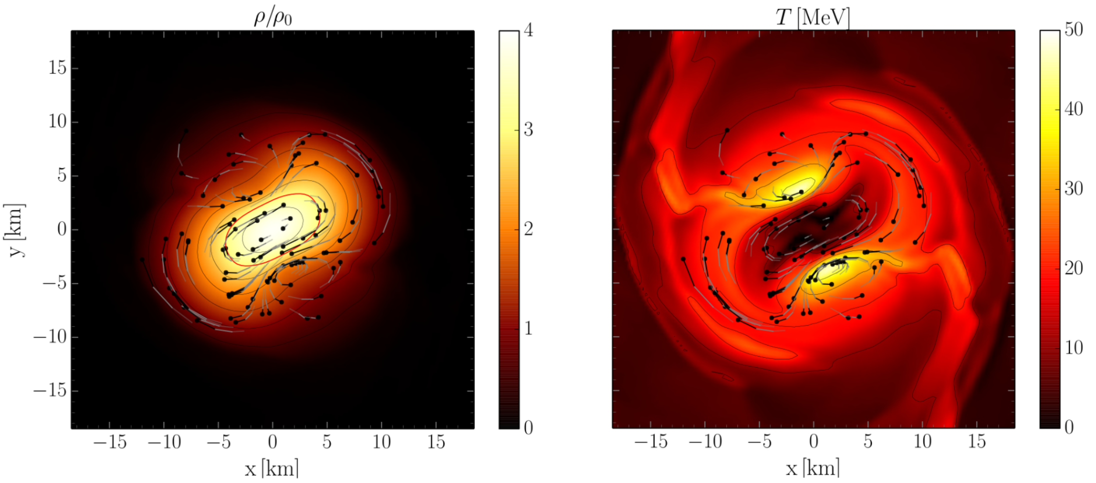

Figure 1.6: Numerical simulation of (**left**) density and (**right**) temperature distribution in the equatorial plane at a post-merger time of $t = 6.34\,\mathrm{ms}$ for the LS220-M132 binary [19].

Heavy-ion collisions

Another method of the QCD diagram study is heavy-ion collisions (HIC). HICs are often described as "little big bangs" because properties of the matter created in HICs and its following evolution resemble that of the matter created in Big Bang, but at smaller scale. Heavy-ion collisions as a method of QCD matter study (in particular in the energy range of the CBM experiment $\sqrt{s_{NN}} = 2.9-4.9\,\mathrm{GeV}$) is the most relevant for the current doctoral work and is described in detail in Sec. 1.4.

1.4 Heavy-ion collisions

The idea to investigate properties of strongly interacting matter at high temperatures belongs to Rolf Hagedorn [20]. He suggested that with increasing the energy, new degrees of freedom may become available. Heavy-ion collisions allow to achieve a state of hot and dense nuclear matter. They take place in the laboratory and thus parameters like the collision energy or the collision system (ions type) can be set by an experimentalist.

The first time heavy-ion collisions were performed in 1971 at Bevatron accelerator in Berkeley laboratory. Also HIC were studied at Alternating Gradient Synchrotron (AGS) experiments situated in BNL [21], in JINR (Nuclotron) [22], CERN (several "North Area" experiments) and GSI (FOPI [23] and KaoS [24]). Since that times the experimental technologies stepped forward significantly. Now energies and interaction rates higher by orders of magnitude can be achieved, but the original idea of colliding two nuclei and measuring produced particles remains in the head of QCD matter study.

There are two groups of heavy-ion collision experiments: colliders and experiments with fixed target. The first group has such advantages as higher available center-of-mass energies and symmetric backward-forward acceptance (which is not so energy dependent as at fixed target experiments). Fixed target experiments are characterized with higher luminosities and wider rapidity coverage in the forward direction (no beam pipe).

At the moment heavy-ion collisions program is implemented in following experiments worldwide:

- HADES - **H**igh **A**cceptance **D**i-**E**lectron **S**pectrometer at SIS-18 [25], GSI, Darmstadt, Germany;
- BM@N - **B**aryonic **M**atter at **N**uclotron [26, 27], JINR, Dubna, Russia;
- SHINE (NA61) - **S**PS **H**eavy **I**on and **N**eutrino **E**xperiment (**N**orth **A**rea 61) [28], CERN;
- STAR - **S**olenoidal **T**racker **at** **R**HIC [29], BNL, Brookhaven, USA;
- ALICE - **A** **L**arge **I**on **C**ollider **E**xperiment [30] at LHC, CERN;
- ATLAS - **A** **T**oroidal **L**HC **A**pparatu**S** at LHC, CERN;
- CMS - **C**ompact **M**uon **S**olenoid at LHC, CERN;

- LHCb - **L**arge **H**adron **C**ollider **b**eauty at LHC, CERN.

Few more experiments are under planning or development now:

- ALICE3 at LHC, CERN;
- MPD - **M**ulti-**P**urpose **D**etector [31] at NICA, JINR, Dubna, Russia;
- J-PARC - **J**apan **P**roton **A**ccelerator **R**esearch **C**omplex [32], JAEA, Tokai, Japan;
- CBM - **C**ompressed **B**aryonic **M**atter (see Sec. 2) at SIS-100, GSI, Darmstadt, Germany.

Heavy-ion collision stages are (see Fig. 1.7):

- **Initial phase:** two ions approach each other in the center-of-mass frame and due to relativistic velocities, their shapes are Lorentz-contracted along the beam direction. Matter distributions of two colliding nuclei overlap (in general case partially). Those nucleons which interact between each other inelastically are called *participants* while those which pass along each other without interaction or interact elastically only are *spectators*.
- **High-density phase and expansion:** participants interact in an inelastic way and produce new quarks. The medium created in the overlap zone is called *fireball*. Depending on the collision energy and system size, different densities and temperatures can be achieved. If the temperature exceeds the threshold of 156 MeV, the matter in the fireball is assumed to consist of quark-gluon plasma. Hot and dense fireball medium expands while cooling down until the temperature when production of new particles is not possible anymore. The composition of hadrons becomes fixed, as soon as inelastic collisions between the particles terminate. This is called *chemical freeze-out*. After that particles continue to interact but only in an elastic way.

- **Final phase:** medium becomes so transparent for particles that their momentum distribution becomes fixed, elastic processes do not happen anymore. This is called *kinetic freeze-out*. Particles continue freely propagate in space.

Only final phase of the collision can be accessed experimentally using plenty of detectors. Further physics analysis techniques together with the model calculations are used to process data obtained by detectors from the final state in order to make assumptions about the initial state.

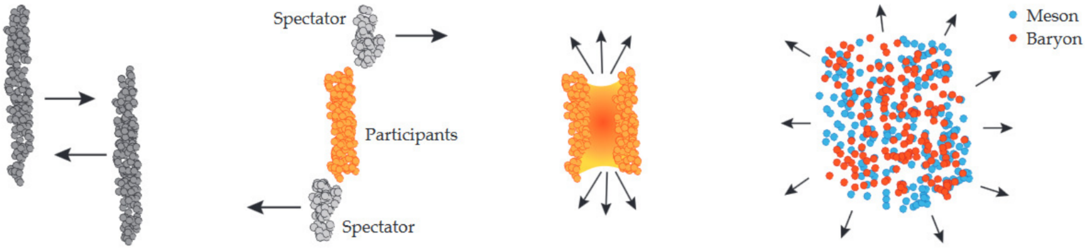

Figure 1.7: Stages of the heavy-ion collision: (**left**) initial phase, (**middle left**) high-density phase, (**middle right**) expansion, (**right**) final phase [33].

1.4.1 Strangeness production at high net baryon densities

Strange quarks do not exist as constituent quarks in usual matter but can be produced at high energies, in particular in heavy-ion collisions. Therefore particles containing strange quarks (see Fig. 1.8) are important probes of the excited medium created in HIC. The strange quark is significantly heavier than up and down quarks ($m_s = 93.4\,\mathrm{MeV}/c^2$ vs $m_u = 2.16\,\mathrm{MeV}/c^2$ and $m_d = 4.67\,\mathrm{MeV}/c^2$) [34]. However, strange-quark has mass still small compared to that of charm-, bottom- and top-quark and thus rather considered as a light quark than a heavy one. The strangeness (S) is conserved in strong interaction, implying associated $s\bar{s}$ production in such processes. Strangeness-changing weak interactions couple strange quarks or hadrons to other flavors.

Strangeness production in heavy-ion collisions was proposed as a messenger of

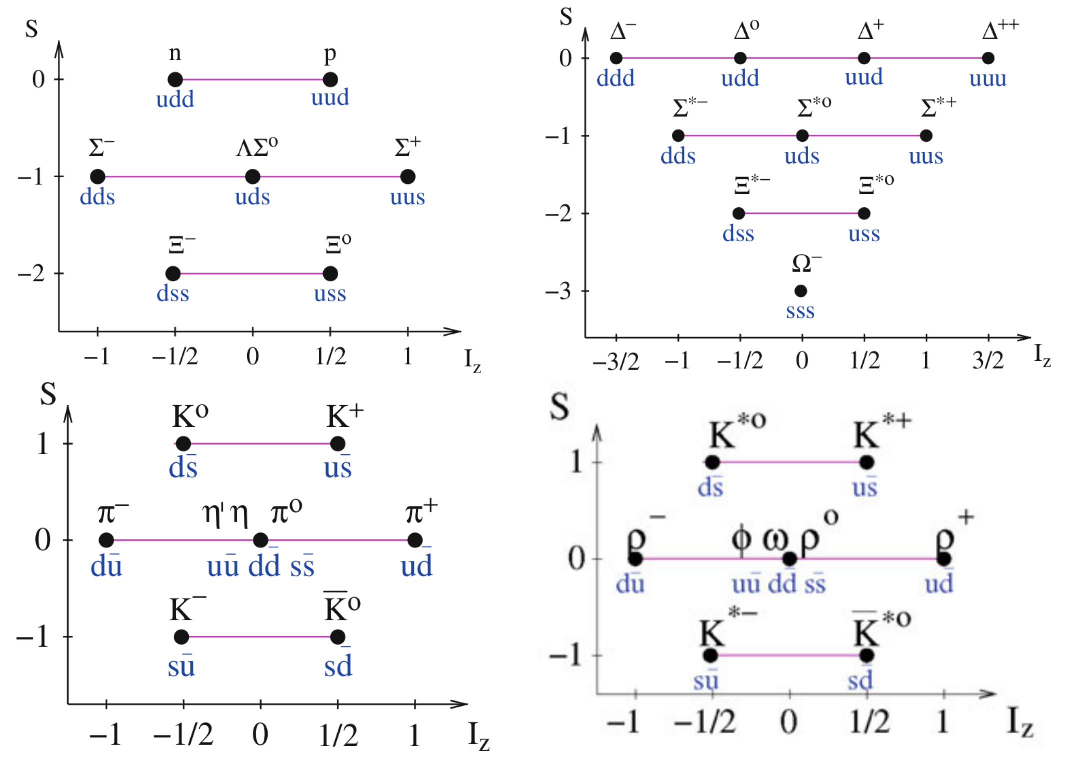

Figure 1.8: Strange-quark containing particles among the most important hadronic states. (**top**) Baryons: (**left**) octet and (**right**) decuplet. (**bottom**) Mesons: (**left**) pseudo-scalar nonet and (**right**) vector nonet.

the deconfined state since strangeness is more effectively produced in parton-parton interactions than in hadronic reactions [35]. Enhanced strangeness production in nuclear collisions comparing to nucleon-nucleon interactions arises naturally in the framework of statistical models as a consequence of the increased reaction volume, which relaxes the impact of exact strangeness conservation on the strange particle yields [36]. Experimental data at SPS energies ($\sqrt{s_{NN}} = 8.8 - 17.3\,\text{GeV}$) [37, 38] confirm strangeness enhancement in Pb+Pb collisions, the enhancement grows with the number of strange valence quarks and reaches up to 10 for Ξ^--baryons, see Fig. 1.9, left. Hadron abundances measured at midrapidity at SPS are well described as a hadron resonance gas in chemical equilibrium [39]. However, yield of Ξ^- hyperons measured at $\sqrt{s_{NN}} = 2.61\,\text{GeV}$ by the HADES collaboration exceeds the thermal model predictions by factor of about 15, see Fig. 1.9, right, indicating that Ξ^- is far from chemical equilibrium [40]. High-precision measurements of excitation functions of (multi-)strange hyperons in heavy-ion collisions with nuclei of various masses at SIS-100 energies will allow to study the degree of equilibration of the fireball, and, hence, open the possibility to find a signal for the onset of deconfinement in QCD matter at high net-baryon densities.

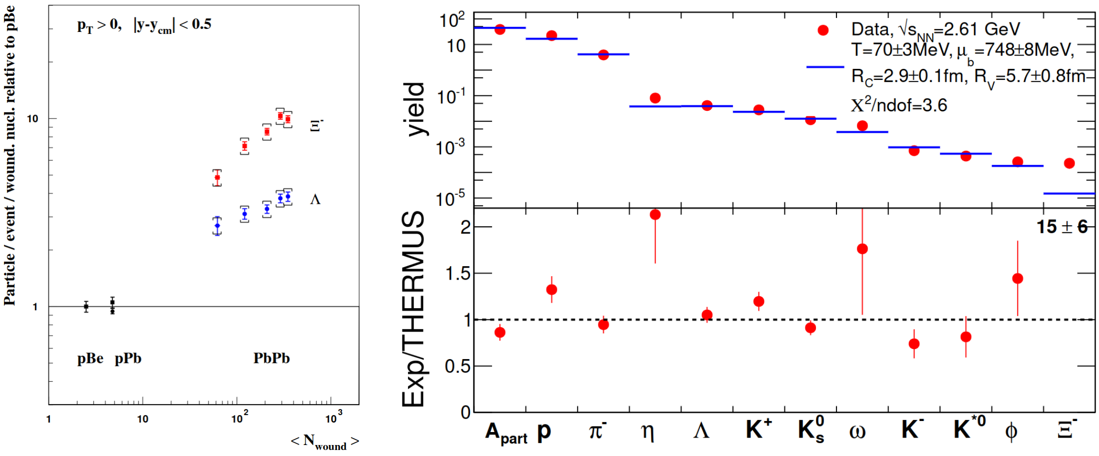

Figure 1.9: (**left**) Enhancement of Λ- and Ξ^- hyperons in Pb+Pb collisions at the SPS with respect to p+p collisions [38]; (**right**) Yield of hadrons measured in Ar+KCl collisions at $\sqrt{s_{NN}} = 2.61$ GeV by HADES collaboration (red symbols) vs thermo-statistical model prediction (blue bars) [40]. For the Ξ^- the ratio number is quoted instead of a point.

1.4.2 Collective phenomena: flow and polarization

The hadron production in nuclear-nuclear collision is different from that in nucleon-nucleon collisions due to collective expansion of the medium created in the overlap zone and strong pressure gradients, shock waves [41] and vorticity. The first evidences of collective effects were obtained in 1980s when the collective flow of protons was observed at the Bevalac in LBNL [42, 43]. Later collective flow was measured at SIS-18 in GSI, AGS and RHIC in BNL, and at CERN. Another important phenomenon - global polarization of strange hyperons - was first time measured in STAR@RHIC [44, 45, 46, 47], later study of this phenomenon was continued at LHC and SIS-18.

Geometry of a heavy-ion collision

When two nuclei approach each other it is very unlikely that they will collide head-on. More probable is that the nuclei overlap is only partial, see Fig. 1.10. The vector connecting centers of target and projectile nuclei is called *impact parameter vector*, and the plane defined with beam direction and impact parameter is called *reaction plane*. In a non-central collision initial matter and energy distribution in overlapping zone is not uniform. Another important consequence is a large angular momentum by order of magnitude equal to

$$\vec{L} = \vec{b} \times \vec{p}_{\mathrm{beam}} \tag{1.2}$$

Also the medium created in HIC is characterized with high vorticity - a measure of velocity field anisotropy:

$$\vec{\omega} = \frac{1}{2}\vec{\nabla} \times \vec{v}(\vec{r}) \tag{1.3}$$

Spatial and velocity anisotropies in the initial state lead to momentum anisotropies in the final state - collective flow and spin polarization of produced particles.

Anisotropic flow

Momentum distribution of produced particles and spectators in the transverse plane, perpendicular to the beam direction, is not uniform. It can be presented as a Fourier series:

$$\rho(\varphi - \Psi_{\mathrm{RP}}) = \frac{1}{2\pi}(1 + 2\sum_{n=1}^{\infty} v_n \cos(n(\varphi - \Psi_{\mathrm{RP}}))), \tag{1.4}$$

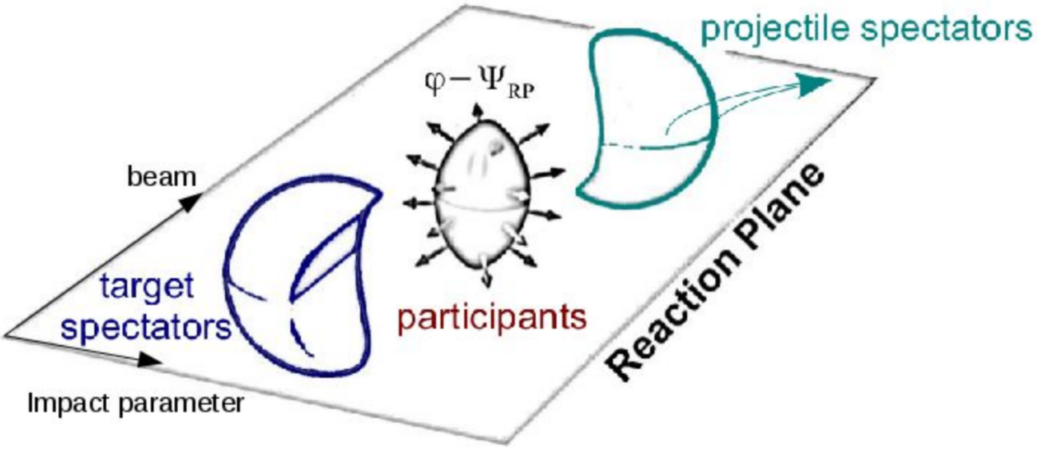

Figure 1.10: Geometry of heavy-ion collision

where ρ is probability density normalized to unity, φ is an azimuthal angle of the produced particle, Ψ_{RP} is a reaction plane angle, v_n is a flow coefficient of n-th harmonic. Due to symmetry considerations Eq. 1.4 does not contain sine terms. Each flow coefficient can be expressed in terms of φ and Ψ_{RP} by multiplying both sides of Eq. 1.4 by $\cos(n(\varphi - \Psi_{\mathrm{RP}}))$ and integrating from 0 to 2π:

$$v_n = \langle \cos[n(\varphi - \Psi_{\mathrm{RP}})] \rangle. \tag{1.5}$$

Thus n-th flow coefficient is an average cosine of n times azimuthal angle between particle's momentum and the reaction plane. By $\langle ... \rangle$ averaging both over particles and events is denoted. In Eq. 1.5 which is a definition of flow coefficients the Ψ_{RP} is not known. There are various experimental methods to obtain the flow coefficients, two of them are described in Sec. 4.2.

Each flow coefficient corresponds to a certain modulation of azimuthal distribution of particles, see Fig. 1.11:

- constant 1 in Eq. 1.4 is a uniform part of particles distribution;
- v_1 is a *directed flow*; it corresponds to particles emission in preferential direction. Positive v_1 means that particles mainly escape along $\vec{b}$ and vice

versa;

- v_2 is an *elliptic flow*; it describes the emission pattern with respect to the reaction plane. $v_2 > 0$, also called *in-plane flow*, means that more particles are emitted in the reaction plane, while $v_2 < 0$, *out-of-plane flow*, corresponds to the situation when particles mainly escape perpendicularly to the reaction plane;

- v_3 is a *triangular flow*, it describes a shamrock-like deformation of particles azimuthal distribution;

- higher order coefficients, i.e. $v_{4,5,6,...}$ also can be defined and calculated.

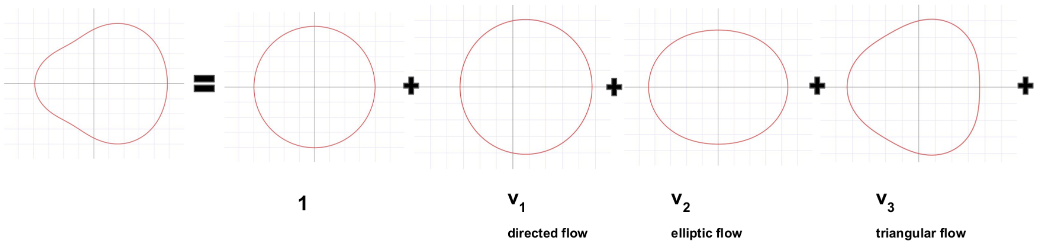

Figure 1.11: Illustration of flow coefficients.

Flow coefficients can be evaluated separately for particles with different kinematics (transverse momentum and rapidity) and events with different centrality. QCD matter equation of state and its parameters (compressibility, viscosity) define the dynamics of produced particles, in particular their momentum anisotropy. Therefore differential and integral measurements of flow coefficients as functions of kinematic variables, centrality and collision energy can provide information about the properties of QCD matter in the fireball and thus help to explore phase diagram. Let us illustrate it with an example of v_1 of protons predicted by various theoretical models, see Fig. 1.12. If one considers the slope of directed flow at midrapidity - dv_1/dy - as a function of collision energy, then at energies $\sqrt{s_{NN}} < 4\,\mathrm{GeV}$ most of the models predict high positive values of slope and at higher energies $\sqrt{s_{NN}} > 10\,\mathrm{GeV}$ the slope is significantly lower. However, the behaviour of slope between lower and higher energies is quite different for different theoretical predictions - some of them predict monotonic decreasing of slope, and another - non-monotonic with double sign change. Experimental measurements allow to judge which models describe the QCD matter better or worse which makes directed flow a very sensitive probe of the initial conditions and QCD matter equation of state.

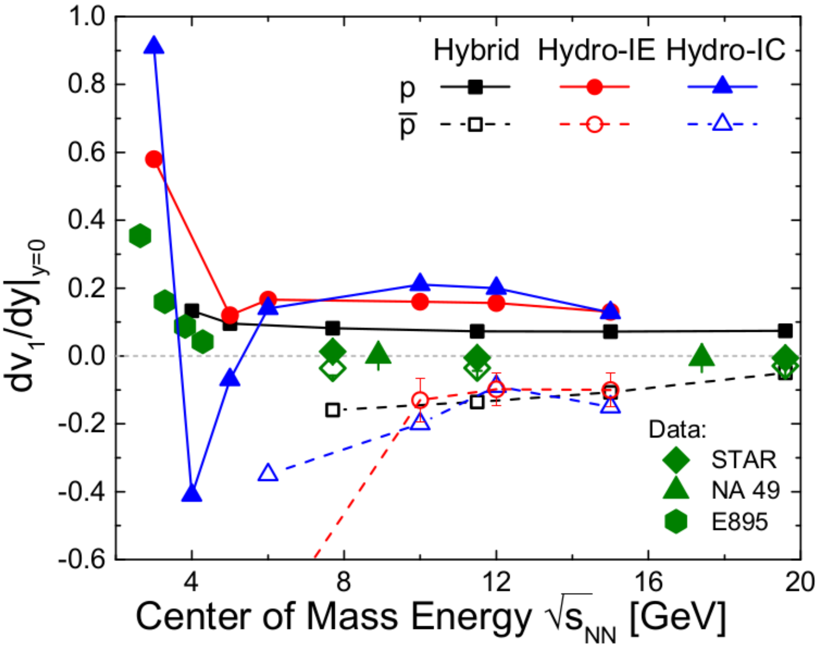

Figure 1.12: Comparison of $dv_1/dy|_{y=0}$ as a function of ($\sqrt{s_{NN}}$) of (anti-)protons for pure hydro and hybrid model calculations with a first order EoS. Experimental data are shown for comparison [48].

Global polarization

Theoretical ideas of a global polarization in HIC have their origin in two complementary effects which have been observed in the beginning of XX century. One of them is Barnett effect [49] - magnetization of an uncharged body when spun on its axis. Another phenomenon, Einstein-de Haas effect [50], is a rotation of a free ferromagnetic body in case of external magnetization of it. Both these effects prove a connection between angular and magnetic momenta of microscopic objects, in particular atoms.

A similar pattern is observed in the medium created in HIC. This medium has a big angular momentum (Eq. 1.2) and shear forces inside it develop a velocity gradient, vorticity (Eq. 1.3). This vortical structure generates magnetic field which makes particles with a non-zero spin to align with it (similarly to the the spin polarization in liquid mercury [51]). In this case we are talking about about *global polarization* of particles.

Polarization of a half-integer spin particle is defined as an expectation value of Pauli spin vector [52]:

$$\vec{P} = \langle \chi | \vec{\sigma} | \chi \rangle, \tag{1.6}$$

where $\vec{\sigma}$ is a vector consisting of Pauli matrices and χ is a wave function of a fermion. By global polarization coefficient we denote polarization vector projection on the axis along angular momentum of HIC divided by $\hbar/2$ (so fully polarized fermions correspond to global polarization coefficient 1). If one performs measurements of the projection of hyperon's spin on the axis along HIC angular momentum, then the relation between number of spin-up $N_\uparrow$ and spin-down $N_\downarrow$ particles and polarization coefficient is following:

$$P_H = \frac{N_\uparrow - N_\downarrow}{N_\uparrow + N_\downarrow} \tag{1.7}$$

This formula expresses hyperon's global polarization by definition but is not a working formula for obtaining it - since we cannot measure directly neither HIC's angular momentum nor spin projection on it. Experimental aspects of P_H calculation are described in Sec. 4.6.

Theoretical models attempt to calculate the amount of polarization of observable particles once the initial condition of the collision is known (energy and the impact parameter of the two nuclei). The final outcome depends on the model of the collision (quark-gluon plasma hydrodinamics properties relevant for vorticity formation) and on how the initial angular momentum may induce a global polarization of the particles (including statistical mechanics approach for polarization, spin relaxation processes and electromagnetic field impact on polarization) [53]. Of particular interest is the difference between global polarization of hyperons and their antiparticles. For example in the energy range $\sqrt{s_{NN}} = 11.5 - 39\,\text{GeV}$ the difference between global polarization of Λ and $\bar{\Lambda}$ is statistically insignificant, but that of $\bar{\Lambda}$ is systematically larger in average by factor of 1.5 [54]. A possible interpretation of a splitting is the presence of a large electromagnetic field and one could use the observed difference to extract the value of the magnetic field in the rest frame of the particles. More complicated explanation is a production of Λ and $\bar{\Lambda}$ in different regions of the fireball and thus their final polarizations reflect coordinate dependence of vorticity [55].

Overview of world data

During the last 40 years flow measurements in a wide energy range from few GeV (SIS-18 and AGS) to several TeV (LHC) were performed. However, world data concerning strange hadrons flow at relatively low energies, which are in the focus of this thesis, (several GeV) is not very rich. So, in Fig. 1.13 the collision energy dependence of the directed flow slope dv_1/dy is shown. Measurements performed at STAR for Λ-baryons and K^0_S-mesons are shown in top left and right plots respectively, while measurements done at HADES, STAR and E895 for Λ-baryons are shown in the bottom plot. One can see a positive slope $dv_1/dy\{\Lambda\}$ decreasing with $\sqrt{s_{NN}}$ to values around or even below zero. The slope $dv_1/dy\{K^0_S\}$ has negative values and non-monotonic behaviour along $\sqrt{s_{NN}}$. Of a particular interest for the current thesis are the flow measurements of strange hadrons at $\sqrt{s_{NN}} = 4.5\,\text{GeV}$ performed by STAR fix target program and at

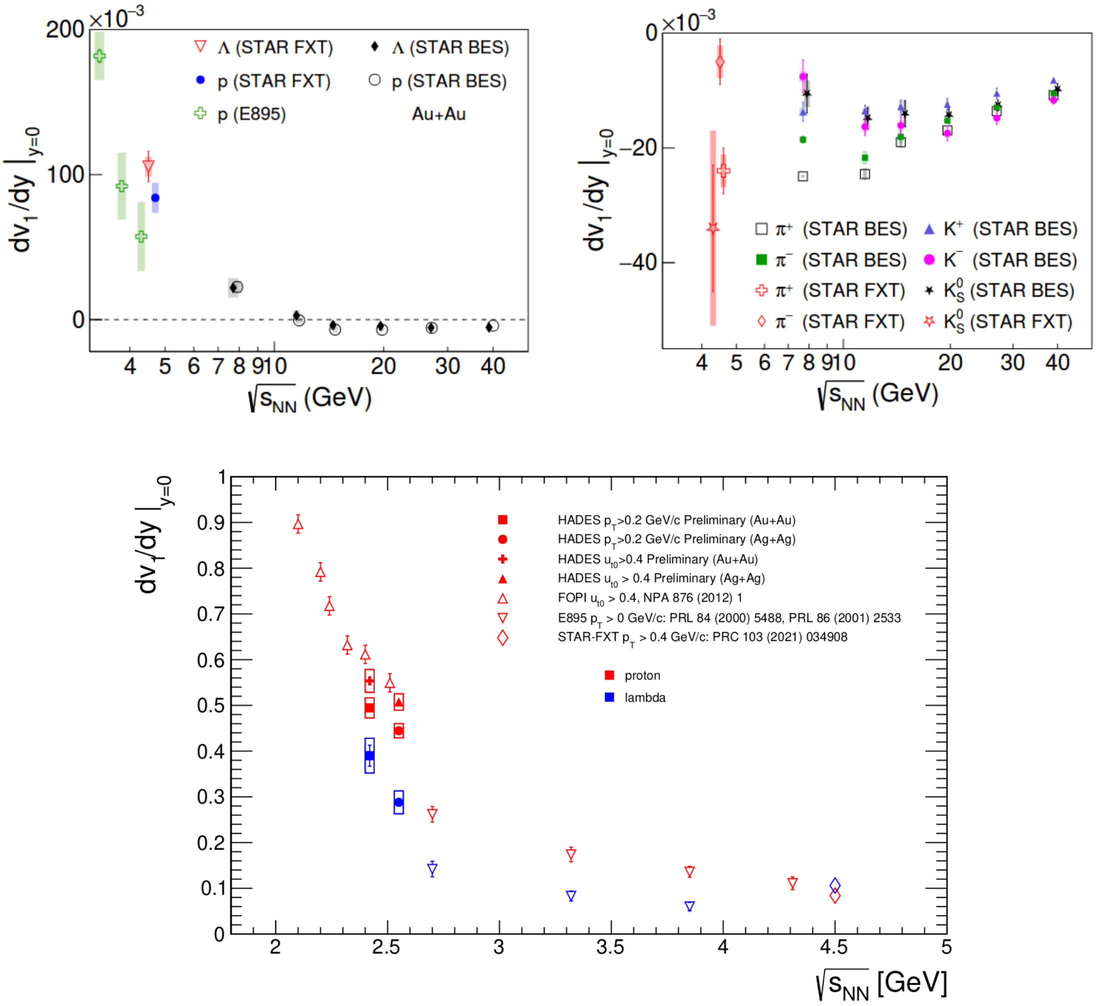

Figure 1.13: Beam energy dependence of the directed flow slope dv_1/dy at midrapidity of: (**top left**) protons and Λ-baryons, (**top right**) mesons incl. K^0_S, (**bottom**) protons and Λ-baryons. Pictures taken from [56, 57].

$\sqrt{s_{NN}} = 2.4 - 2.55$ GeV performed by HADES. Fig. 1.14 presents these measurements differentially, as a rapidity dependence of v_1 in mid-central events. One can see that the directed flow of Λ monotonically grows with rapidity while that of K^0_S has a wiggle structure and changes the sign three times. Small amount of data of strange hadrons flow in the energy range of few GeV (and complete absence of that for multi-strange hadrons) and large statistical and systematic uncertainties (as for K^0_S, see Fig. 1.13, top right) serve as a motivation for the CBM to cover these energies with high statistics measurements, keeping systematics under control.

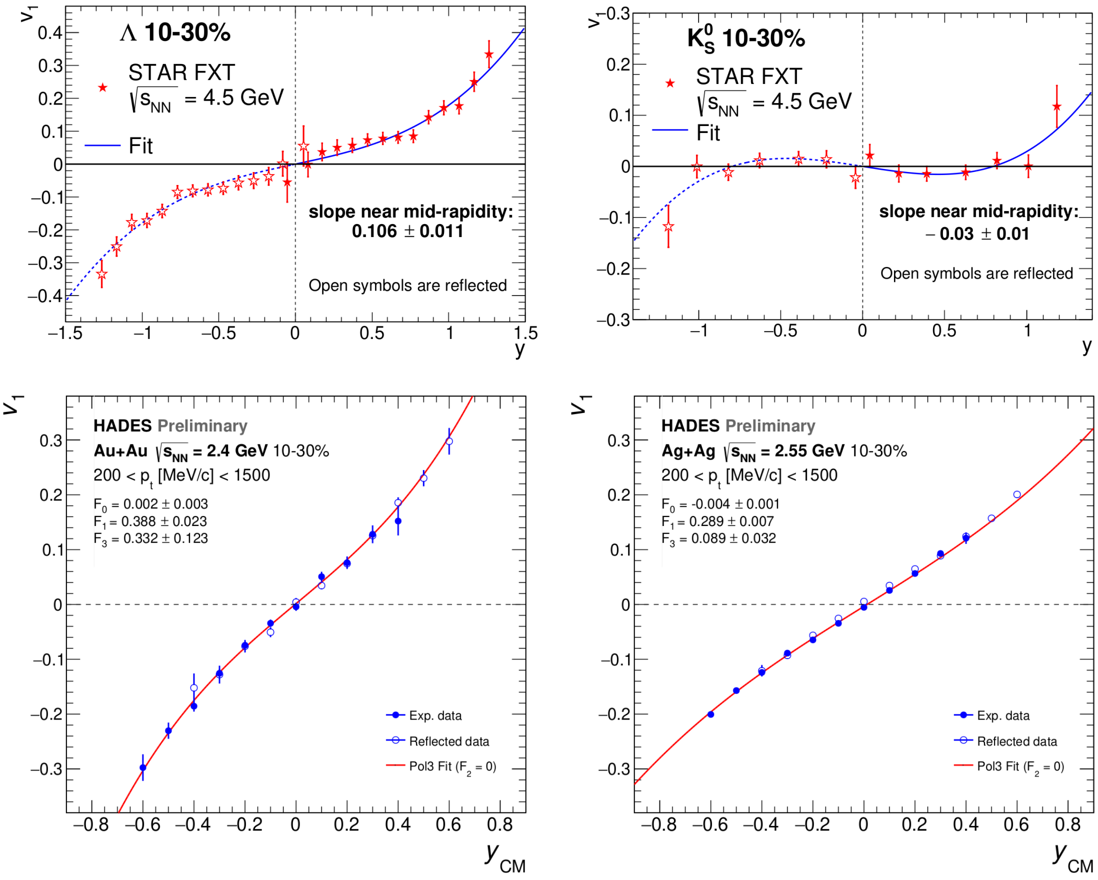

Figure 1.14: Rapidity dependence of the directed flow v_1 of (**top left**) Λ-baryons and (**top right**) K^0_S-mesons measured in Au+Au collisions at $\sqrt{s_{NN}} = 4.5\,\text{GeV}$ by the STAR collaboration [56], of Λ-baryons measured in (**left**) Au+Au collisions at $\sqrt{s_{NN}} = 2.4\,\text{GeV}$ and (**right**) Ag+Ag collisions at $\sqrt{s_{NN}} = 2.55\,\text{GeV}$ by the HADES collaboration [57]. Open symbols are the reflection of the solid symbols. A 3-d order polynomial fit is shown with a line.

Fig. 1.15 illustrates global polarization of Λ-hyperon as a function of collision energy shifted by two nucleon mass. Solid lines represent theoretical predictions of $P_\Lambda(\sqrt{s_{NN}} - 2m_N)$ provided by various models. A big gap in the energy range relevant for CBM studies (only single measurement by STAR is present) motivates CBM to do intensive studies there in order to discover physics scenarios which are realized in QCD matter created in HIC.

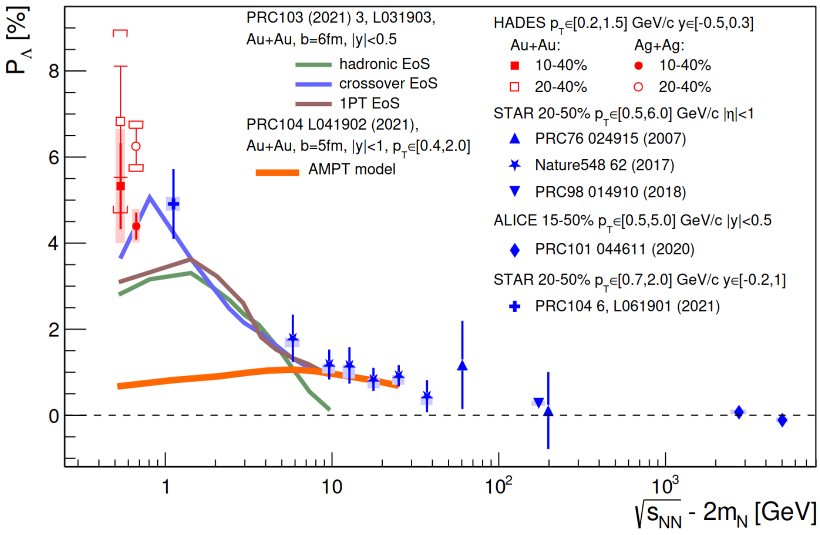

Figure 1.15: Global polarization of Λ-hyperons as a function of the center-of-mass energy above $2m_N$, where m_N is the nucleon mass [58].

1.4.3 Monte-Carlo modeling

General considerations

This subsection describes conceptual schemes and computational models that are used for the dynamical description of high-energy nuclear collisions. Heavy-ion collision modeling is complicated by various aspects. First of all, nuclear systems are relatively small, even on the scale of the strong interaction range; more than half of nucleons are situated on the surface of the nucleus. Surface energy together with the long-range Coulomb interaction reduces the binding nuclear energy relative to that of corresponding piece of bulk matter. Therefore the physical environments produced in nuclear collisions are far from those of idealised uniform matter and it is essential to take proper account of the significant variation of the local conditions throughout the system probed. Secondly, the time window during which net baryon and energy densities are significantly enhanced is often so short that local equilibrium may not be established. Consequently there is no straightforward connection between the statistical equilibrium quantities, such as temperature and chemical potentials, and collision final state observables. Thus, while thermodynamics describes bulk matter in statistical equilibrium, which may be characterised as being large and stationary, the available collision systems are rather small and transient. These problems are inherent to heavy-ion physics, it is necessary to rely extensively on dynamical transport treatments. But it is not possible to derive such treatments directly from the underlying QCD quantum field theory. Phenomenological modelling is therefore required.

Heavy-ion collisions can be described within the transport framework. While transport description should ideally be derived from the basic physics, in practice it is significantly relying on phenomenology. An important feature of many-particle reaction models is information reduction ("coarse graining"): following the detailed many-body evolution of the evolving system are neither practical nor desirable. In practice, the most important information is expressible in terms of the one-body phase-space densities for the various particle species. Transport descriptions generally rest on a separation of the space-time scales that characterise the microscopic interactions between individual hadrons from the scales characteristic for the macroscopic dynamics. In majority of transport approaches the hadrons motion in between the close encounters is described in classical deterministic way, while short-range encounters between hadrons are described in a probabilistic way because of smearing of the initial conditions with coarse-graining. However, at high hadron densities the separation between the various times scales becomes blurred, and the typical time between hadron-hadron encounters becomes comparable to the duration of the encounters themselves. Moreover, the macroscopic evolution grows relatively rapid and can no longer be clearly separated from the microscopic time scales. In this case identification of individual hadrons becomes problematic and a description in terms of constituent partons may be more appropriate. Degrees of freedom considered in the model (either nucleon or partonic) naturally define the energy range where the model is applicable.

Cascade models

Cascade models provide the simplest microscopic transport descriptions of high-energy nuclear collisions. They represent the nucleus as a collection of A spatially fixed individual nucleons distributed within the nuclear volume. The incoming hadron then interacts sequentially with those target nucleons that are encountered along its path through random momentum changes in accordance with the free elementary cross sections. Between the scattering events all particles move classically on straight lines.

In cascade models different scattering prescriptions are used [59]. The most common one is to decide on the scattering event by means of an impact parameter criterion related to the total cross section and to randomly change the particles' momenta. A competing approach is to use a deterministic classical prescription which relates the scattering angle to the impact parameter, e.g. such as a hard sphere (Billiard ball) dynamics. The first one has a trivial equation of state (EoS), namely that of a gas of non-interacting particles, the second approach implies a highly non-trivial EoS, namely that of a hard-sphere gas.

The early implementations of cascade models included nucleons and Δ resonances which can scatter both elastically ($NN \leftrightarrow NN$, $N\Delta \leftrightarrow N\Delta$, $\Delta\Delta \leftrightarrow \Delta\Delta$) and inelastically ($NN \leftrightarrow N\Delta$, $N\Delta \leftrightarrow \Delta\Delta$). Δ resonances decay only after all interactions had ceased. The pion (and other hadronic states) were explicitly included in later extensions. The Fermi momenta of the initial nucleons were usually included in the kinematics which was particularly important for production processes near or below threshold.

Hadronic cascade treatments have provided a useful framework for understanding the dynamics of relativistic nuclear collisions. However, their relevance is limited by few-GeV energy range. At higher energies, including CBM energy range which is in particular interest of current doctoral work, the partonic degrees of freedom become to play a role and therefore models taking them into account are required.

String models

The majority of the dynamical models being used in energy ranges where the partonic degrees of freedom can be excited do not explicitly treat the partonic degrees of freedom. Rather, they invoke concepts developed for the description of elementary collisions, such as pp, $p\bar{p}$, e^+e^-. The basic picture is that of a color exchange between the virtual partons associated with the fast-moving collision partners. So, as a result, colour charges become spatially separated and energy is being stored into the resulting chromo-electric field between the receding colour charges. It leads to the formation of the strings between quark and antiquark and quark and diquark [60]. The energy stored in the string may then subsequently create $q\bar{q}$-pairs that locally neutralise the field and thus fragment the string.

Thus, phenomenological strings present a tool for taking account of the fact that an increase of the collision energy leads to the activation of partonic degrees of freedom (quarks and gluons), without a need for explicitly treating the partonic phase.

Light nuclei and nuclear fragments production

Cascade and string models describe production of hadrons, in particular of nucleons. However, in the final state also nuclei are present - both light (deuterons, tritons, He-3, α-particles) and nuclei of intermediate masses and even heavy (up to the mass of colliding nuclei). The mechanism of nuclei production depends on their mass. For light nuclei it is mainly a coalescence [61] - formation of a deuteron from neutron and proton situated close to each other and with small relative momenta. By consequent joining of more nucleons heavier nuclei - tritons, helium etc - can be produced. Coalescence phenomenon can also involve Λ-baryons forming hypernuclei, e.g. ${}^{3}_{\Lambda}\mathrm{H}$, ${}^{4}_{\Lambda}\mathrm{H}$, ${}^{4}_{\Lambda}\mathrm{He}$ [62].

Another mechanism, which is more relevant for nuclei of medium and high masses, is nuclear fragmentation. It is well known that highly-excited ($5-10A$ MeV) residual nuclei are produced in inelastic nuclear reactions induced by intermediate- and high-energy particles and nuclei, and then they disintegrate. Such reactions can be divided into three stages:

1. The initial non-equilibrium stage leading to the production of an excited nuclear system;
2. The formation of fragments and break-up of the system into separate fragments;
3. Farther de-excitation of hot fragments via evaporation or fission.

The first step is described by cascade models. Residual nuclei disintegration at the second step can be described by a wide variety of models that have been proposed for nuclear multifragmentation, e.g. probabilistic, macroscopic, statistical models of different kinds, sequential evaporation, and many other models. Finally, the excited thermalized residual nucleus decays then according to fission and/or sequential evaporation model.

Statistical approaches have proved to be very successful for description of fragment production in nuclear reactions, therefore let us consider Statistical Multifragmentation Model (SMM) [63] in more detail. Depending on the value of residual nuclei excitation energy, it can either reach equilibrium or not. If excitation energy is lower than $\approx 3A\,\mathrm{MeV}$, then a so-called compound nucleus [64] is created, which is an equilibrated intermediate state of the nucleus, decaying mostly via evaporation of light particles and fission. At higher excitation energies the system does not reach equilibrium since the time intervals between subsequent fragment emissions become very short. For such systems a simultaneous break-up into many fragments happens. In SMM light nuclei ($A \leq 4$, $Z \leq 2$) are considered as elementary stable particles forming a gas while heavier nuclei are treated as heated nuclear liquid drops. This model performs a “competition” between all break-up channels - Fermi break-up, compound nucleus decay, fission etc, taking into account the conservation of baryon number, electric charge and energy.

Specific implementations of heavy-ion collision models

Monte-Carlo simulation of heavy-ions collisions is implemented in various models. Here are some of them, relevant for a few GeV collision energy range:

- **SMASH** - **S**imulating **M**any **A**ccelerated **S**trongly-interacting **H**adrons [65];
- **PHSD** - **P**arton-**H**adron-**S**tring **D**ynamics [66, 67];
- **PHQMD** - **P**arton-**H**adron-**Q**uantum-**M**olecular-**D**ynamics [68].

Let us consider in more details two heavy-ion collision models used in the current doctoral work:

DCM-QGSM-SMM [69, 70] stands for **D**ubna **C**ascade **M**odel - **Q**uark-**G**luon **S**tring **M**odel - **S**tatistical **M**ultifragmentation **M**odel. It consists of three modules, added to each other consequently. Originally, the Dubna Cascade Model [61] was developed, which is based on the Monte-Carlo solution of a set of the Boltzmann-Uehling-Uhlenbeck relativistic kinetic equations with the collision terms, including cascade-cascade interactions. To make the DCM code applicable at higher energies (up to hundreds AGeV), it was merged with the Quark-Gluon String Model. QGSM simulating elementary hadron collisions at energies higher than about 5 GeV describes binary collisions in the framework of independent quark-gluon strings quasiclassical approximation [71]. An approach of mean (self-consistent) field is used to describe particles' interaction between each other. Finally, the Statistical Multifragmentation Model was joined in order to simulate nuclear fragments production and their momenta distribution.

UrQMD [72, 73] stands for **U**ltra**r**elativistic **Q**uantum **M**olecular **D**ynamics model. It is also a cascade model, and includes strings for partonic degrees of freedom simulation at higher energies. Unlike DCM-QGSM-SMM model, the UrQMD uses many-body approach for description of particles interaction between each other - molecular dynamics. Significant limitation of the UrQMD is an absence of nuclei fragmentation - spectator nucleons are assumed to be separated from each other after the collision takes place.

Both DCM-QGSM-SMM and UrQMD models provide a realistic prediction concerning the directed flow of strange hadrons in the energy range relevant for the CBM ($\sqrt{s_{NN}}$ of several GeV). As shown in Fig. 1.16, left, the DCM-QGSM-SMM predicts behaviour and magnitude of $v_1(y)$ consistent with STAR measurements both for Λ and K^0_S. Fig. 1.16, right, shows that UrQMD also reproduces the measured values of protons and Λ-baryons directed flow well.

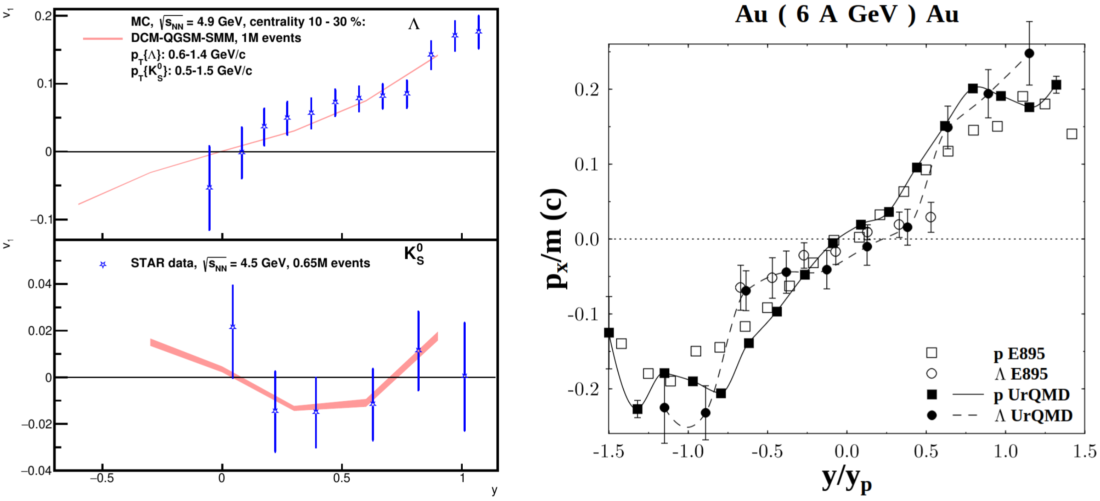

Figure 1.16: (**left**) Directed flow dependence on rapidity for (**top**) Λ and (**bottom**) K^0_S: STAR FXT data [56] (blue stars) and DCM-QGSM-SMM predictions (red line). A p_T-cut is set to mimic the STAR's acceptance. (**right**) Directed transverse flow p_x/m as a function of normalized rapidity y/y_p for protons (squares) and Λs (circles): E895 data [74] (open symbols) and UrQMD predictions (full symbols) [75].

Chapter 2

CBM experiment at FAIR

2.1 FAIR overview

Facility for Antiproton and Ion Research (FAIR) in Darmstadt, Germany, will be one of the largest and most complex accelerator facilities in the world. The existing accelerator facilities (Fig. 2.1, blue), located at GSI Helmholtz Centre for Heavy Ion Research, together with planned p-Linac will serve as the injector for the FAIR facility (Fig. 2.1, red) which is under construction since 2017. FAIR will have the unique ability to provide particle beams of ions, as well as antiprotons. The particles will be accelerated to almost the speed of light in the FAIR accelerator facility and made available for scientific experiments. The FAIR facility consists of a superconducting ring accelerator, storage rings and experiment sites with several kilometers of beam line in total.

The four scientific pillars of FAIR are:

- **A**tomic, **P**lasma **P**hysics and **A**pplications - APPA;
- **C**ompressed **B**aryonic **M**atter - CBM;
- **Nu**clear **St**ructure, **A**strophysics and **R**eactions - NUSTAR;
- Anti**p**roton **An**nihilation at **D**armstadt - PANDA.

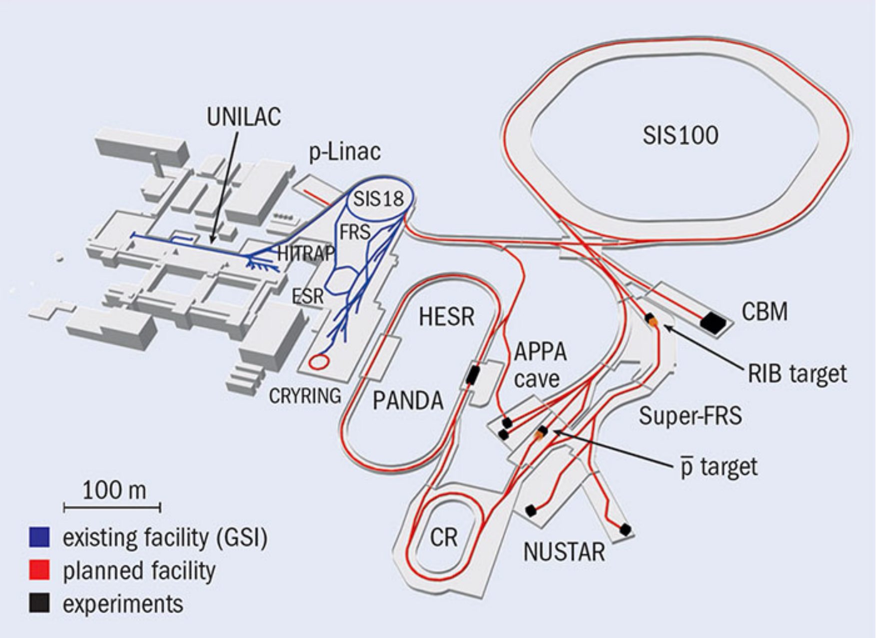

Figure 2.1: Accelerator facilities existing (GSI) and under construction (FAIR).

One of the most prominent parts of the future FAIR is the Heavy-Ion Synchrotron (in German *Schwer-Ionen-Synchrotron-100*), from here SIS-100. It is a 1083 m long accelerator of protons and ions consisting of superferric magnets with magnetic rigidity 100 Tm. The transverse beam width is of order of 0.1 cm at the target. The minimal available ion beam kinetic energy is about $2A$ GeV. The top kinetic energy available at the SIS-100 is up to 29 GeV for protons, $14A$ GeV for ions with $Z/A \approx 0.5$ (C, O, Ni) and $11A$ GeV for heavy ions with $Z/A \approx 0.4$ (Au, Pb). It will allow to perform high-statistics measurements and thus study rare processes.

2.2 Compressed baryonic matter (CBM) experiment at FAIR

2.2.1 Physics program

The region of the QCD phase diagram with the highest net-baryon densities can be reached in heavy-ion collisions at moderate collision energies which will be available at the Facility for Antiproton and Ion Research (FAIR). At high net-baryon densities reached in FAIR energy range, the phase transition between hadronic and partonic matter is expected to be first order, featuring a region of phase coexistence and a critical endpoint. The experimental discovery of these prominent landmarks of the QCD phase diagram would be a major breakthrough in our understanding of the properties of nuclear matter. Equally important is experimental information on the properties of hadrons in dense matter which may shed light on chiral symmetry restoration and the origin of hadron masses. In order to investigate physics phenomena mentioned above, the CBM will perform comprehensive measurements of excitation functions, system size dependencies and multi-differential phase-space distributions of identified particles, including flow, event-by-event fluctuations and other types of correlations. Physics program of CBM includes following main topics:

- Strangeness;
- Collective phenomena;
- Event-by-event fluctuations;
- Lepton pairs;
- Charm;
- Hypernuclei.

Strangeness

Particles containing strange quarks are important probes of the excited medium created in heavy-ion collisions. The CBM experiment will open a new precision era of multi-differential measurements of multi-strange (anti-)hyperons. High interaction rates will provide acceptable statistical significance of measurements of the production of rare strange and anti-strange baryons in dense nuclear matter (see Fig. 2.2). Excited hyperon states can be identified as well. It will be possible to study hyperon-nucleon and hyperon-hyperon correlations which allows exploring the role of hyperons in neutron stars. In more details the strangeness production is discussed in Sec. 1.4.1.

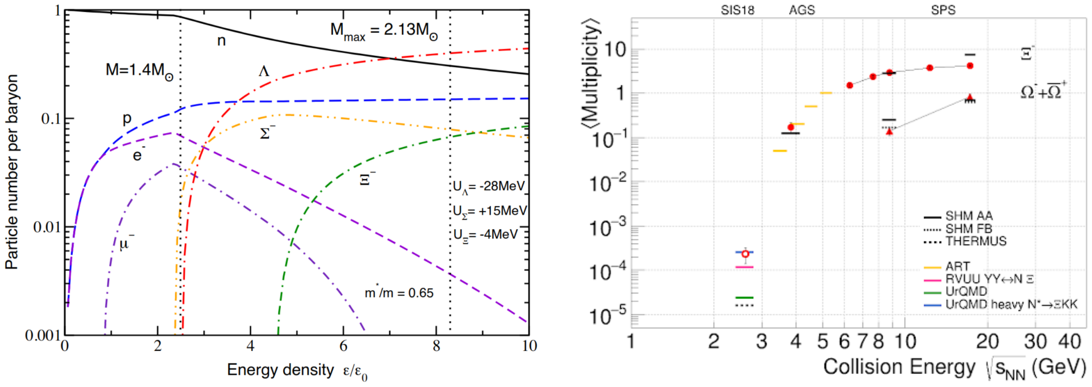

Figure 2.2: (**left**) Fraction of particles produced in the inner core of a neutron star as a function of the energy density, in units of energy density ε_0 at the nuclear saturation point [76]. (**right**) Multistrange hyperons yields vs collision energy: theoretical predictions and experimental data [77].

Collective phenomena

The collective flow of hadrons is driven by the pressure gradient created in the early fireball and provides information on the dense phase of the collision. These measurements will be important for understanding the QCD matter equation-of-state at neutron star core densities. At collision energy of the STAR FXT program $\sqrt{s_{NN}} = 4.5\,\text{GeV}$, which is covered by the SIS-100 energy range, anisotropic flow measurements were performed for pions, (anti-)protons, charged kaons, and Λ with K^0_S, but statistics is quite low [56, 78]. Angular anisotropy (flow) and polarization phenomena will be explored, that will provide information about the properties of matter in the fireball at early stages of collision and mechanisms responsible for transfer angular momentum into magnetic. High interaction rates at CBM will significantly improve precision and allow anisotropic flow measurements of identified particles, including multistrange hyperons and dileptons. More detailed anisotropic flow is discussed in Sec. 1.4.2.

Event-by-event fluctuations

The passage through a phase transition of the matter is associated with a rapid change (depending on temperature and chemical potential) of the thermodynamic susceptibilities, which reflect the corresponding fluctuations. Event-by-event fluctuations of conserved quantities (electric charge, baryonic number, strangeness) can provide information about the phase transition and properties of matter created in high-energy nuclear collisions. These are local fluctuations (e.g. in some rapidity range), not global, that are prohibited for conserved quantity. Another interesting observable is the fluctuation of particles multiplicity ratios (e.g. K to π) or ratio between baryon number and strangeness. Higher-order moments (cumulants) of these fluctuations are expected to be sensitive to the proximity of the critical point.

Measurements of event-by-event fluctuations have been performed by the NA49, PHENIX, STAR, ALICE and HADES collaborations in order to search for the QCD critical point. STAR measured $\kappa\sigma^2$ (kurtosis times squared standard deviation) of the net-proton multiplicity distribution as a function of the collision energy in Au+Au collisions [79]. The presence of a critical point is expected to lead to a non-monotonic behaviour of the $\kappa\sigma^2$ observable [80, 81]. For the most central collisions at $\sqrt{s_{NN}} = 7.7\,\mathrm{GeV}$ a deviation of $\kappa\sigma^2$ from unity (as expected according to Poisson law) is observed that can be an evidence of critical behaviour, see Fig. 2.3, however, statistical uncertainties are too large in order to make an unambiguous conclusion. These results motivate further research of higher-order fluctuations with rich statistics at lower beam energies in order to search for the peak in $\kappa\sigma^2$. The CBM experiment will perform a high-precision study of higher-order fluctuations at various beam energies in order to search for the elusive QCD critical point at $\sqrt{s_{NN}} = 2.9-4.9\,\mathrm{GeV}$ and $\mu_B = 500-800\,\mathrm{MeV}$.

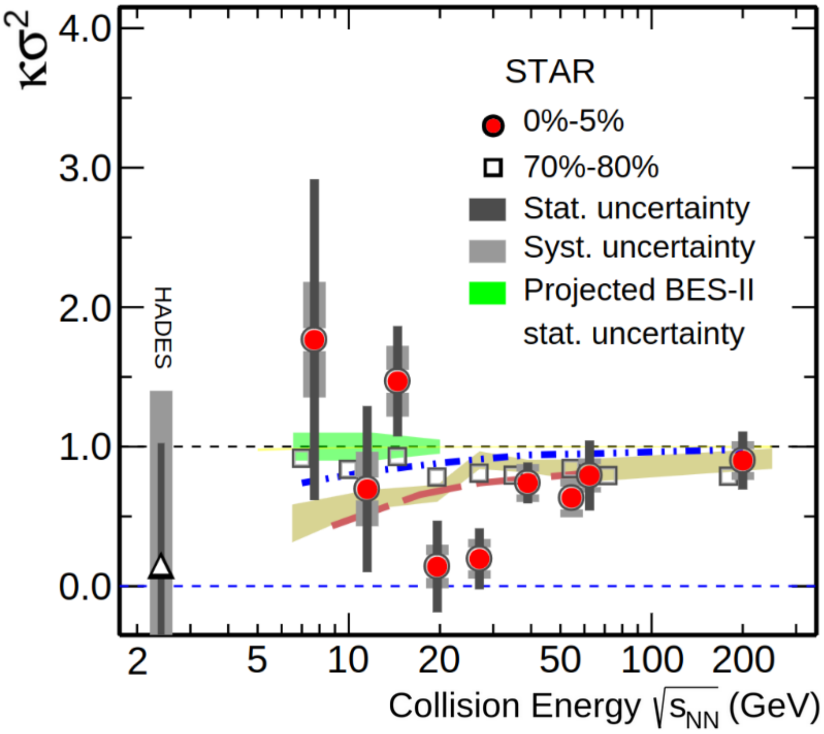

Figure 2.3: Energy dependence of the $\kappa\sigma^2$ of the net-proton multiplicity distribution for top 0-5% central Au+Au collisions (red circles) [82].

Lepton pairs

Electromagnetic (EM) radiation is a unique probe of strongly interacting matter in HIC. Once the (real or virtual) photon is produced, it escapes the medium essentially undistorted, since its mean free path is much larger than the typical system size. Once produced, photons decouple from the collision zone and materialize as muon or electron-positron pairs (also named *dileptons*). Leptonic decay channels offer the possibility to look into the fireball and to probe the hadronic currents of strongly interacting systems in a state of high temperature and density. Dileptons inherit from their parent particle the invariant mass, which makes them the prime observable to search for in-medium modifications of hadrons. This is restricted to vector mesons, which are directly coupled to the EM current, in particular light vector mesons ρ, ω and ϕ.

The excess yield of lepton pairs with invariant masses up to $1\,\mathrm{GeV}/c^2$ is sensitive to both the temperature of the created matter and its lifetime. It measures the fireball lifetime and is sensitive to chiral symmetry restoration [83]. The slope of the dilepton invariant mass distribution between 1 and 2.5 GeV/c^2 reflects the average temperature of the fireball [84] and provides indications about onset of deconfinement and the location of the critical endpoint.

No dilepton data exist for heavy-ion collisions at beam energies between $2A$ and $40A\,\mathrm{GeV}$. The CBM experiment will perform pioneering multidifferential measurements of lepton pairs over the whole range of invariant masses emitted from a hot and dense fireball. According to model calculations, various processes will contribute to the measured yield: thermal radiation (including a broadened in-medium ρ meson), radiation from the QGP and multi-pion annihilation. The precise measurement of the energy dependence of the spectral slope opens the unique possibility to measure the caloric curve, which would be the first direct experimental signature for phase coexistence in high-density nuclear matter.

Experimental measurements of dileptons require leptons identification and separation them from pions. Dalitz decays of light neutral mesons (e.g. π^0 and η) and lepton pairs produced by photon conversion in the target and detector material represent a physics background in dileptons analysis. Uncorrelated combinations of electrons and muons pairs, forming combinatorial background, have also to be subtracted. Measurements of both electron and muon pairs complement each other allowing to control systematic errors.

Charm

Particles containing charm and/or anticharm quarks in heavy-ion collisions probe the early phase of the fireball due to the large mass of the charm quarks which can be produced in hard processes only. The charm and anti-charm quarks hadronize into D-mesons, charmed baryons or charmonium (J/ψ). The suppression of charmonium due to colour screening of the heavy quark potential in the deconfined phase has been predicted as a signature for quark-gluon plasma formation [85]. Charmonium suppression was observed by NA50 collaboration in central Pb+Pb collisions at 158A GeV [86] and then also found by PHENIX [87] and ALICE [88]. At low beam energies the charm production mechanisms and yields are sensitive to the conditions inside the fireball, because the absolute production threshold for a $c\bar{c}$ pair in a partonic environment is lower than the minimum energy needed to create a pair of charmed hadrons. Therefore study of both total and relative yields of hadrons containing charm quarks in HIC at threshold energies can provide information about the degrees of freedom in the early fireball.

No data on charm production in heavy-ion collisions are available at beam energies below 158A GeV. At FAIR energies the charm sector becomes accessible with proton-nuclei collisions, and measurements of open and hidden charm will be performed for the first time in heavy-ion collisions close to (nucleon-nucleon) threshold energies.

Hypernuclei and strange objects

Thermal model [89] calculations of single and double hypernuclei production in heavy-ion collisions are shown as a function of collision energy in Fig. 2.4. The yield maximum is within SIS-100 energy range. This is due to the superposition of the increase of light nuclei production with decreasing beam energy, and the increase of hyperon production with increasing beam energy.

The CBM experiment will reconstruct hydrogen and helium hypernuclei in huge

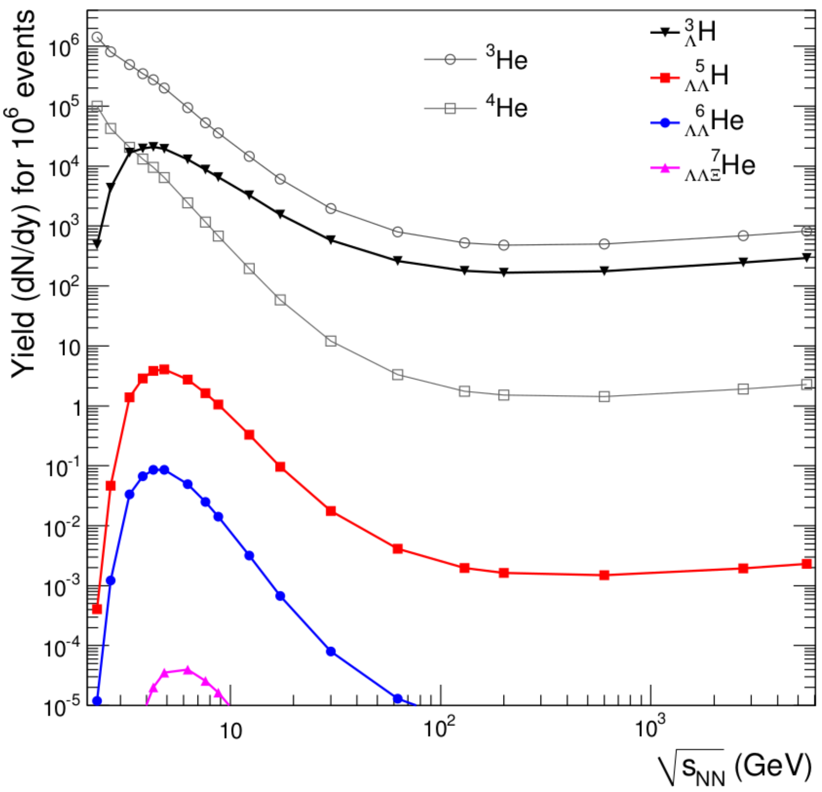

Figure 2.4: Energy dependence of hypernuclei yields at midrapidity for 10^6 central collisions as calculated with a thermal model [89]. ^{4}He and ^{3}He are shown for comparison.

amounts ($dN/dy \approx 5 \times 10^{-3}$ of $^3_\Lambda$H at midrapidity). Double-strange hypernuclei measurements will be possible as well. Up to now only a few double-Λ hypernuclei events have been found [90]. The discovery of (double-)Λ hypernuclei and the determination of their lifetimes will provide information on the hyperon-nucleon and hyperon-hyperon interactions, what is important for understanding the nuclear matter equation-of-state at high densities and the structure of neutron stars [91]. Also theoretical models [92, 93] predict existence of such exotic objects as metastable exotic multi-hypernuclear objects (MEMOs) and purely hyperonic systems consisting of Λs and Ξ^-s. CBM offers an exciting perspective to explore the formation of composite objects with multiple strangeness in heavy-ion collisions at SIS-100.

2.2.2 Experiment design

The CBM experiment will be able to identify both hadrons and leptons, and rare probes at reaction rates of up to 10 MHz with charged particle multiplicities of up to 1000 per event (Fig. 2.5 shows interaction rates of world experiments and CBM among them). The experiment will also allow lepton identification (both electrons and muons), high-resolution secondary vertex reconstruction and a high speed triggering and data acquisition.

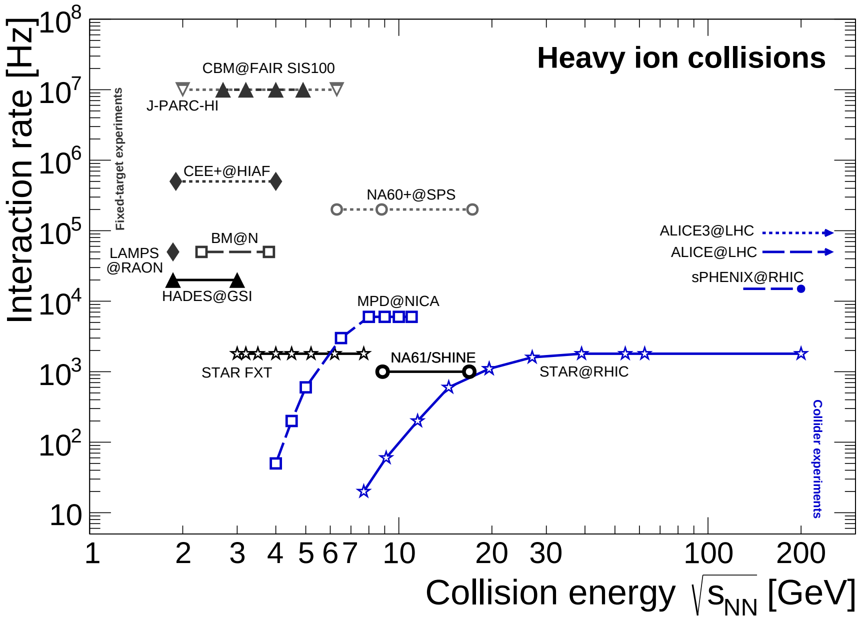

Figure 2.5: Interaction rates vs collision energy: CBM@FAIR among other world experiments [94].

The CBM contains following subsystems, shown in Fig. 2.6:

- Silicon Tracking System (STS), main tracking detector, based on double-sided silicon micro-strip sensors arranged in eight stations;

- Micro Vertex Detector (MVD) for displaced decay vertices reconstruction, with four layers of silicon monolithic active pixel sensors;

- superconducting dipole magnet which encapsulates inside STS and MVD and allows momentum measurement of charged particles;
- Ring Imaging Cherenkov (RICH) detector for electron and pion identification comprising a CO_2 radiator and an UV photon detector realized with multi-anode photomultipliers;
- Muon Chamber (MuCh) system for muon identification consisting of a set of gaseous micropattern chambers sandwiched between hadron absorber plates made of graphite and iron;
- Transition Radiation Detector (TRD) for pion suppression, particle tracking and identification using specific energy loss;
- Time-of-Flight wall (TOF) for charged hadrons identification based on Multi-Gap Resistive Plate Chambers with low-resistivity glass;
- Projectile Spectator Detector (PSD) for centrality and event plane determination.

Silicon Tracking System

The STS [95] is the heart of the experimental setup installed in a large acceptance dipole magnet. It consists of 8 low-mass silicon micro-strip detectors providing unambiguous space point measurements. The sensitive component of the silicon detector is a reverse biased diode with the depleted zone acting as a solid-state ionization chamber. When charged particle passes through an active volume of the detector, a lot of electron-hole pairs are produced along the path of the particle. Under the application of reverse-bias voltage, electrons drift towards the n-side and holes to the p-side. This charge migration induces a current pulse on the read-out electrodes. High mobility of electrons and holes provides very fast collection of the signal. The STS allows track reconstruction in a wide momentum

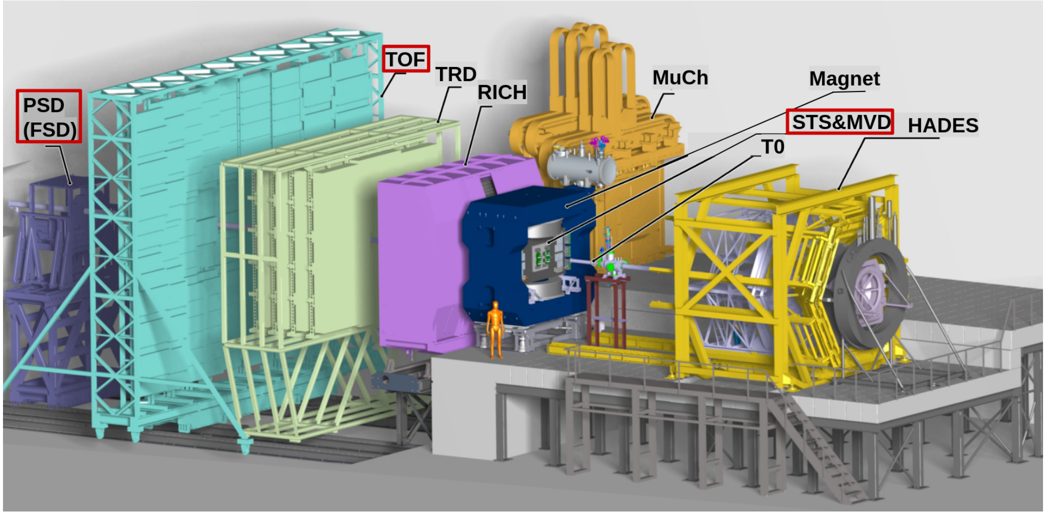

Figure 2.6: CBM experiment design; the most relevant subdetectors for study of (multi-)strange hyperons flow are highlighted with red frames. T0 denotes time-zero detector and beam diagnostics. The HADES setup will be placed in front of the CBM.

range from about 100 MeV up to more than 10 GeV with a momentum resolution of about 1.5%. The typical hit resolution is of order of 25 μm. This performance can only be achieved with an ultra low material budget of the stations, imposing particular restrictions on the location of power-dissipating front-end electronics in the fiducial volume. STS stations are located at distances between 30 and 100 cm from the target, and its acceptance covers the polar angle between 2.5° and 25°. Schematic view of the STS is shown in Fig. 2.7, left.

Micro Vertex Detector

The MVD [96] is needed to determine secondary vertices with high precision, in particular for D-mesons reconstruction. It consists of 4 layers of ultra-thin and highly-granulated Monolithic Active silicon Pixel Sensors (MAPS) which are located in vacuum in front of the STS (5–20 cm from the target). Physical principle of signal registration in the MVD is similar to that of the STS. The MVD acceptance is the same as of the STS. Expected resolution of secondary vertex position along beam axis is up to 250 μm. Schematic view of the MVD is shown in Fig. 2.7, middle and right.

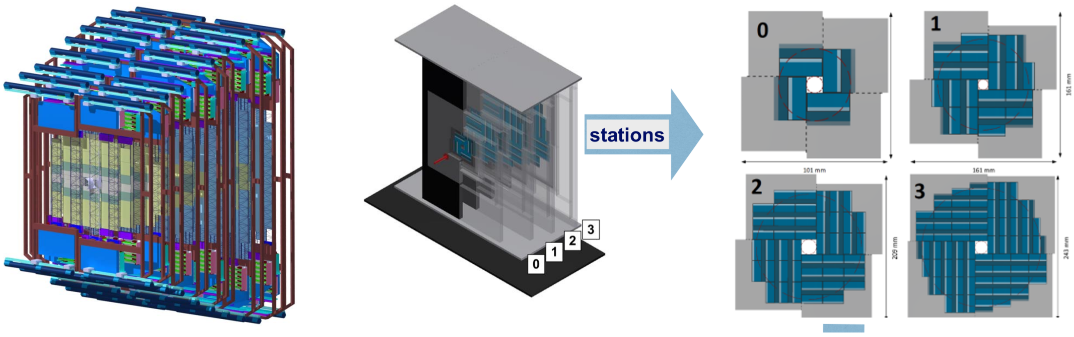

Figure 2.7: Schematic view of (**left**) Silicon Tracking System; Micro Vertex Detector: (**middle**) full setup and (**right**) MVD stations separately.

Dipole magnet

The superconducting dipole magnet [97] serves to bend charged particle trajectories in order to determine their momenta. It has an aperture of ±25° in polar angle and provides a magnetic field integral up to 1 Tm in order to provide momentum resolution of order of $\Delta p/p = 1.5\%$. The magnet gap has a height of 144 cm and a width of 300 cm to accommodate STS and MVD inside. Magnetic field is not homogeneous, it is mainly directed along vertical axis and the maximum value of its magnitude is around 1 T. Dipole magnet scheme is shown in Fig. 2.8.

Ring Imaging Cherenkov detector

The main task of the RICH detector [99] is to identify electrons and positrons with momenta up to 10 GeV, in particular to distinguish them from pions. The identification technique is based on the measurement of Cherenkov radiation emitted by charged particles passing a radiator with velocity higher than speed of light in the medium. Cherenkov photons form a cone-shaped front which spreads at an angle θ to the momentum of the particle, such as $\cos\theta = c/nv$ where c is

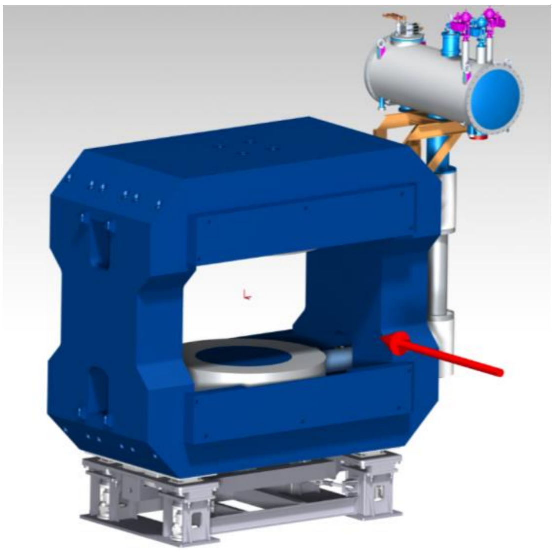

Figure 2.8: Dipole magnet geometry scheme [98].

the speed of light in vacuum, n is a refraction index of the radiator and v is particle's velocity (see Fig. 2.9, left). Emitted Cherenkov photons fall on spherical mirrors (shown in blue in Fig. 2.9, right) where due to geometrical optics reasons they form a ring image with radius proportional to θ. Finally, reflected Cherenkov photons are captured by position-sensitive photon detectors (yellow planes in Fig. 2.9, right), what allows to reconstruct radius of the produced ring and therefore - angle θ and particle's velocity. Relation between particle's velocity and momentum allows to make a hypothesis about its mass and type. In the CBM setup RICH uses CO_2 as a radiator and is situated after the STS in 1.6 m from the target.

The Muon Chamber system

The experimental challenge for muon measurements in heavy-ion collisions at FAIR energies is to identify low-momentum muons in an environment of high particle densities. The CBM concept is to track the particles through a hadron absorber system, and to perform a momentum-dependent muon identification. This concept is realized in MuCh system [100] consisting of hadron absorber

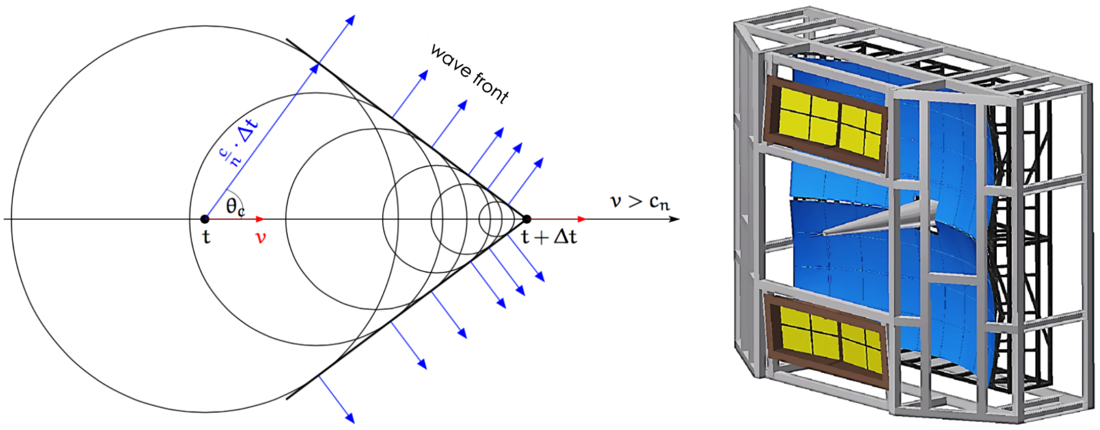

Figure 2.9: (**left**) Geometrical scheme of Cherenkov radiation wave front spread; (**right**) schematic view of the Ring Imaging Cherenkov detector.

segmented in several layers (red cylinders in Fig. 2.10, left) and triplets of tracking detector planes placed in the gaps between the absorber layers (yellow planes in Fig. 2.10, left). Hadron absorbers consist of carbon (the first one) and iron (all the rest) while tracking planes are based on Gas Electron Multiplier (GEM) and Multigap Resistive Plate Chambers (MRPC) technologies. In order to reduce meson decays into muons the absorber and detector system have to be as compact as possible. The MuCh system is placed downstream the STS and replaces the RICH detector in case of using of the CBM muon setup.

Transition Radiation Detector

The TRD [101] task is to improve identification of electrons and positrons with respect to pions for the momenta larger than 1.5 GeV/c. The detection is based on the effect of emission of transition radiation by charged particle crossing the boundary between two media with different refraction indices. The total energy loss of a charged particle during the transition depends on its Lorenz factor $\gamma = E/mc^2$. A single detector module consists of a radiator and a drift chamber as a photon detector. Detector modules are united into TRD stations located at distances approximately $5 - 9.5$ m downstream the target. In order to keep the occupancy below 5% for central heavy-ion collisions, the minimum area of a single cell should be about 1 cm^2. The pion suppression factor obtained with TRD is estimated to be well above 100 at an electron efficiency of 90%. Additionally, the TRD can serve as a tracking detector, bridging the gap between the STS and the TOF detectors. Fig. 2.10, right, illustrates the layout of the Transition Radiation Detector.

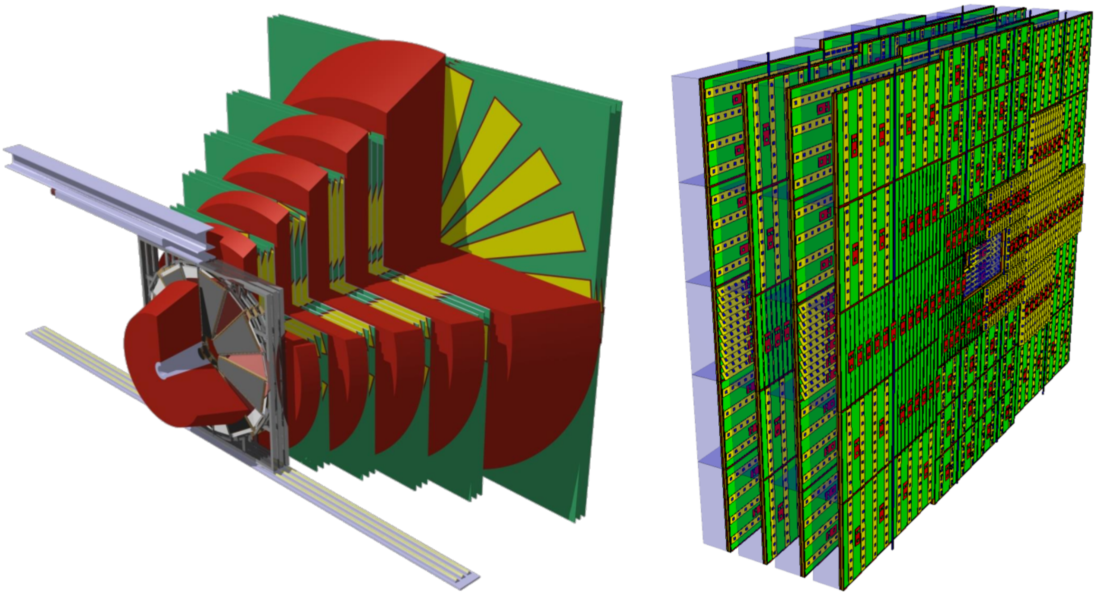

Figure 2.10: Layout of (**left**) the Muon Chamber system; (**right**) the Transition Radiation Detector.

Time Of Flight detector

TOF detector [102] is used for the identification of charged particles, mostly hadrons. Determination of the particle mass is based on the measurement of the time of flight, the particle momentum and the particle track length (for details see Sec. 2.3.3). TOF consists of Multigap Resistive Plate Chambers (MRPC). Charge particle ionizes gas inside MRPC gap, and high voltage applied to the sides of the gap amplifies this ionization by an electron avalanche. Resistive plates stop the avalanche and collect the signal produced by the particle. To obtain sufficient separation between different particle species, a time resolution better than 80 ps is required. For an acceptance coverage close to the one of the STS total size of the TOF wall placed at a distance of 7 m downstream the target has to be $12 \times 9\,\mathrm{m}^2$. Schematic view of the TOF wall is shown in Fig. 2.11.

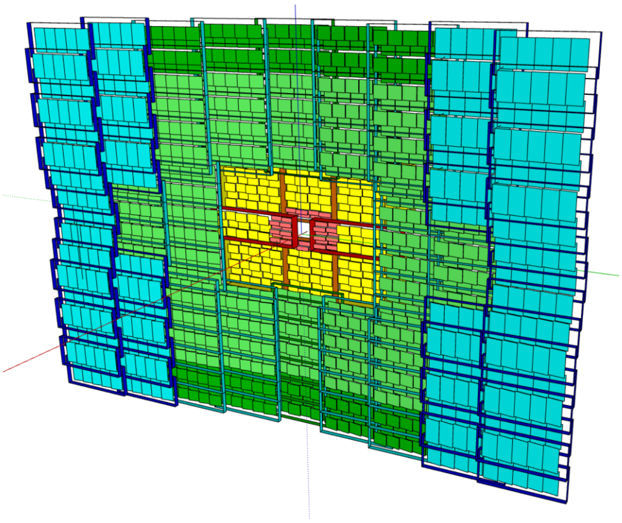

Figure 2.11: Layout of the Time-of-Flight detector.

Projectile Spectator Detector

The main purpose of the PSD [103] is to provide experimental information about event characteristics such as collision centrality and orientation of the reaction plane. The detector is a hadronic calorimeter which is designed to measure the energy distribution of the projectile nucleus fragments (spectators), and the forward going particles produced close to beam rapidity. The general layout of the PSD is shown in Fig. 2.12, left. The Projectile Spectator Detector is located in 8 m from the target and its acceptance covers polar angles $0.21° < \theta < 5.7°$. It has 44 modules with size $20 \times 20\,\mathrm{cm}^2$ consisting of lead and scintillator layers. Modules can be divided into groups sensitive to particles with different pseudorapidities; this division is illustrated by different colors in Fig. 2.12, right. The PSD has a diamond hole of size $20 \times 20\,\mathrm{cm}^2$ in the center which is needed to avoid radiation damage at high beam intensities.

Disclaimer: *At the time of writing this thesis the CBM Collaboration decided to replace the PSD hadronic calorimeter with another detector - Forward Spectator Detector (FSD), which is the scintillator array. Results presented in the current doctoral work with the PSD provide a baseline performance for the ongoing research and development work and preparation of the FSD.*

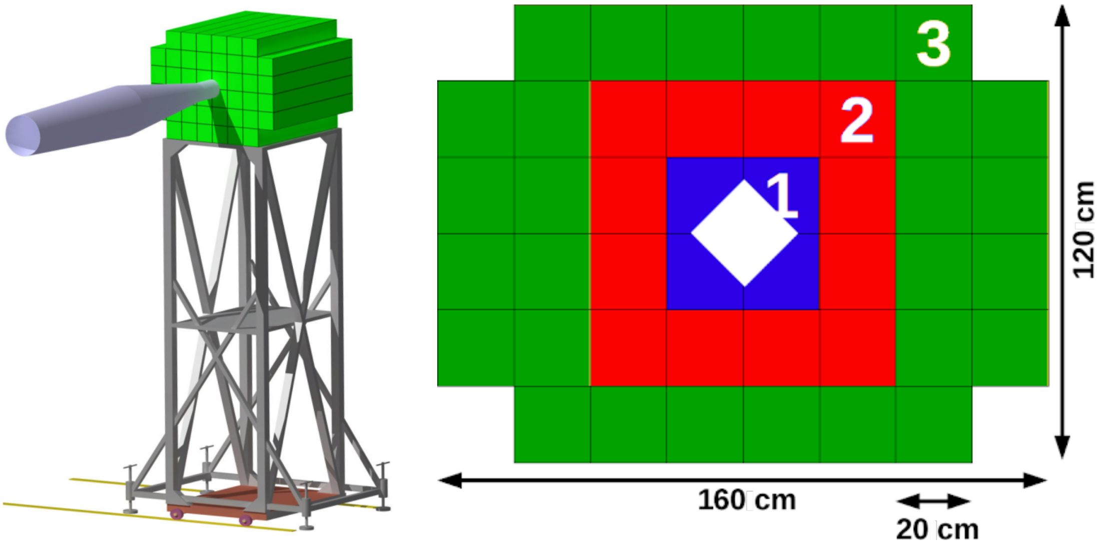

Figure 2.12: (**left**) Projectiles spectator detector layout; (**right**) PSD view along beam pipe. PSD modules used for building different subevents (see Sec. 4.2) are shown with different colors.

Tab. 2.1 briefly summarizes the content of this chapter showing which subsystems of the CBM detector are relevant for study of different particles species.

2.3 Reconstruction algorithms

The event selection is based on an on-line reconstruction running on a computing farm equipped with many-core CPUs and graphics cards. Track reconstruction, which is the most CPU-time consuming stage of the reconstruction, is based on parallel track finding and fitting algorithms, implementing the Cellular Automa-

	MVD	STS	RICH	MuCh	TRD	TOF	PSD
$\pi^{\pm}$, $K^{\pm}$, $p^{\pm}$		+	(+)		(+)	+	+
Hyperons		+			(+)	(+)	+
Open charm	+	+	(+)		(+)	(+)	+
$e^{\pm}$	+	+	+		+	+	+
$\mu^{\pm}$		+		+		(+)	+
γ							+
γ **via** $e^{\pm}$	+	+	+		+	+	+

Table 2.1: Observables and CBM detector subsystems required for their measurements marked with "+" sign. Detectors marked with "(+)" can be used to suppress background.

ton and Kalman Filter methods.

Neutral and short-lived particles are reconstructed via their decay topology using KFParticle - Kalman filter based tools. Charged hadrons are identified by time of flight - using Bayesian approach. Events are classified into centrality classes using measured multiplicity or an energy deposit in a forward detector.

2.3.1 Cellular-automaton track finder

The concept of cellular automaton (CA) is based on the Game of Life [104] introduced by John Conway. The cellular automaton method models a discrete dynamical system, whose evolution is completely determined by local mutual relations of constituent elements of the system named *cells*. A general scheme of the CA-based track finder is shown in Fig. 2.13, left. In this example the cell is a potential track segment, consisting of two detector measurements - hits (0). At the first stage the algorithm builds all possible track segments (1). Then the evolution of the cellular automaton takes place: the method searches for neighboring segments, which share a hit in common and have the same direction within some error, and, thus, potentially belong to the same track (2). During this search the track finder also estimates a possible position of the segment in the track. Starting with a segment of the largest position counter, the track finder follows a chain of neighbours collecting segments into a track candidate (3). As a result one gets a tree structure of track candidates. In the last stage the competition between the track candidates takes place: only the longest tracks with the best χ^2 sharing no hits in common survive (4).

2.3.2 Kalman-filter track fit

Usually track fitting algorithm exploits the so-called track model, which is a theoretical assumption on the equation of motion for charged particles in the volume of a tracking detector. One of the most common algorithms used for track fitting in high energies physics is the Kalman filter method [105] schematically illustrated in Fig. 2.13, right.

Let us consider a dynamic system, whose evolution in time is described with a state vector $\vec{r}_t$, consisting of several system parameters, and covariance matrix C describing uncertainties of the state vector. The Kalman filter method obtains an optimal estimate $\vec{r}$ of the state vector $\vec{r}_t$ based on the measurements of this state vector which may be contaminated with noise (e.g. scattering). Fitting procedure can be divided into three main stages: initialization, prediction (propagation) and filtration (update). The method starts with an initial approximation $\vec{r} = \vec{r}_0$ if one is available, or alternatively with arbitrary values. In this case the covariance matrix reflects low confidence level of the initial estimate and therefore is equal to numerical infinity. Then the current estimate of the state vector and the covariance matrix at the measurement are propagated to the point of the next measurement, while taking into account possible noise. Finally the $\vec{r}$ estimate is improved (updated) taking into account each measurement, providing as a result the optimal estimate after adding the last measurement. Propagation and update stages are repeated several times according to the number of measurements. The result of the fitting procedure is the state vector after the last measurement which describes the kinematics of the track.

It is worth noting that in principle the track parameters also can be derived from the hit measurements by applying the least squares fit. But Kalman filter method is preferable since its recursive nature allows for a computationally simpler and numerically optimized implementation. Also it allows to take noise into account. Track finding and reconstruction algorithms are described more detailed in [106].

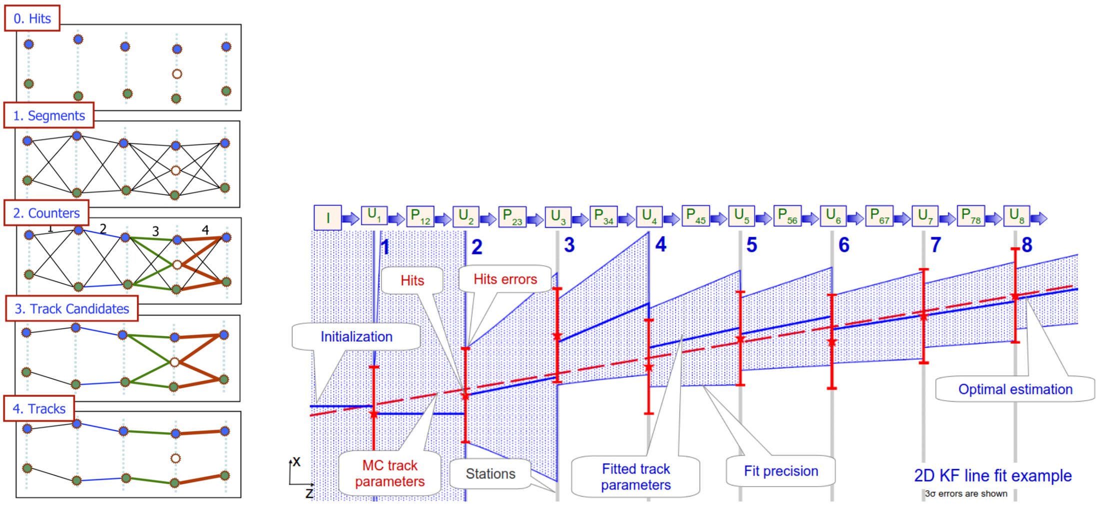

Figure 2.13: (**left**) Illustration of the cellular automaton based track finding algorithm: tracking stations are shown by vertical dashed lines, hits of two different particles are shown by blue and green circles, the noise hit is shown by empty circle; (**right**) illustration of Kalman Filter based track fit: I stands for initialization, U_k for update at k-th measurement, $P_{k\ k+1}$ for propagation between k-th and k+1-th measurement [106].

2.3.3 Charged track identification

For performing physics analysis one needs to apply a realistic particle type hypothesis on reconstructed charged tracks. Since particles species differ from each other with their kinematics, they can be identified by analysing their momenta and velocity. It is called *Time-of-Flight* method of particles identification. In CBM it is done in the following way: each track reconstructed in STS (and

MVD) is extrapolated to the TOF wall, the nearest hit in the TOF is associated to it. Then the relation between kinematical parameters of the track can be expressed with formula:

$$\frac{m^2}{q^2} = \frac{1}{c^2}\frac{p^2}{q^2}\left(\frac{c^2t^2}{L^2} - 1\right), \tag{2.1}$$

where p is particle's momentum, q - particle's charge, L - length of its trajectory, t - time passed from collision to appearance of associated hit in TOF, m - particle's mass hypothesis. Particle's mass obtained from Eq. 2.1 can be used as a discriminator between particles' species. A significant shortcoming of the Time-of-Flight method is that it cannot distinguish tracks with the same m/q ratio, e.g. deuterons and alpha-particles. But since in the current thesis we are interested in hadrons with $|q| = 1$, in further formulae q will be omitted for simplicity, and p will be a signed momentum which is positive for positively charged tracks and vice versa. Fig. 2.14 (left) shows the distribution of tracks extrapolated to TOF in $m^2 - p$ space. One can see spots in places characteristic to certain particles. They are localized at places corresponding to real particles' masses, but due to finite detector resolution in momentum and time measurement, spots are smeared and width of smearing is increasing with momentum of particle. There are also entries in places which are not characteristic for any particles species. They are assumed as background and appear mostly due to mismatch between reconstructed track and TOF hit.

In order to operate with particles identification in terms of probabilities, a Bayesian approach is used [107]. 2-dimensional $m^2 - p$ histogram is sliced vertically into ranges in p; in each vertical slice the population of particles is considered as a function of m^2 (blue ticks in Fig. 2.14, right). Entries in certain momentum range are assumed to include contributions from different particles species (pions, kaons, protons, nuclei etc.) and background appearing due to mismatch between track and TOF hit. Population dependence on m^2 is fitted with following set of

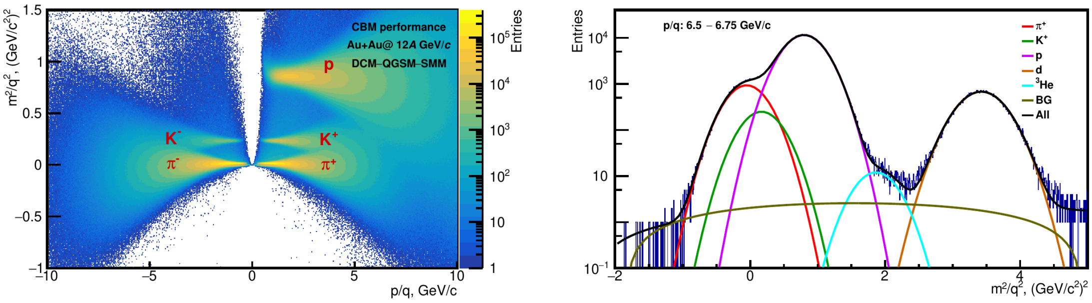

Figure 2.14: (**left**) $m^2 - p$ dependence for registered charged tracks; (**right**) Gaussian fit of particles population vs m^2 for certain momentum range.

functions and fit parameters:

- Gaussian function for particles' yields with mean value, standard deviation and full integral as fit parameters;
- 2-nd order polynomial for background with polynomial coefficients as fit parameters.

Colored lines in Fig. 2.14 (right) show particles, background and total fit of positively charged tracks in certain momentum range. This procedure is repeated in each vertical slice. Then fit parameters obtained at previous step are assumed as functions of p, and are fitted with polynomial functions.

After determination of fit parameters one can obtain the probability that a particle with certain m^2 and p belongs to $j-$th species using following formula (particle's purity):

$$P_j(m^2, p) = \frac{G_j(m^2, p)}{\sum_i G_i(m^2, p) + BG(m^2, p)}, \tag{2.2}$$

where i is an iterator of particles species ($i = \pi^{\pm}, K^{\pm}, p, ...$), $G_i(m^2, p)$ is an $i-th$ particles species fit function value at point (m^2, p), $BG(m^2, p)$ is a background fit function value. Then to each track which has matched hit in TOF a particle type hypothesis can be applied basing on purities obtained with Eq. 2.2. For hypothesis one can choose e.g. the particle with highest purity or particle with purity higher than some pre-defined threshold etc.

Bayesian fitting procedure described in this subsection is implemented in ROOT based C++ framework Pid [108]. Validation and maintenance of the Pid package together with its interface co-development is a part of current doctoral work.

2.3.4 Decay reconstruction

Neutral particles (such as Λ-hyperons or K_S^0-mesons) do not leave hits in the tracking system, so they cannot be reconstructed directly. A similar issue applies to charged particles with short lifetime (such as Ξ^-- and Ω^--baryons) - although they are charged, but they mainly decay before they leave enough hits in STS (+MVD) to be reconstructed as tracks. However, it is possible to reconstruct them by their weak decay products. This topic occupies a significant part of the current doctoral thesis and is comprehensively described in Sec. 3.

2.3.5 Centrality determination

The volume and evolution of the matter produced in heavy-ion collision depend on the collision geometry. Centrality of the collision C_b is defined via impact parameter b:

$$C_b = \frac{1}{\sigma_{AA}} \int\limits_0^b \frac{d\sigma(b')}{db'} db', \tag{2.3}$$

where σ_{AA} is a total cross section of nucleus-nucleus inelastic interaction, and $d\sigma(b')/db'$ is a differential cross section as a function of impact parameter.

Impact parameter cannot be measured directly and experimentally the collision is characterized with multiplicity of charged particles detected with tracking system (STS and MVD) or with the energy registered in the PSD, which are (anti-)correlated with the impact parameter, as shown in Fig. 2.15. The dependence between E_{PSD} and b is non-monotonic. E_{PSD} increases with impact parameter but beginning with $b \approx 8\,\mathrm{fm}$ E_{PSD} decreases again. It happens because heavy fragments produced in peripheral collisions have direction very close to the beam and pass through the hole in PSD (see Fig. 2.12, right) without being registered. Therefore in further work multiplicity of reconstructed tracks is used as centrality estimator. Events are distributed into centrality classes in the following way [109]:

$$C_M = \frac{1}{\sigma_{AA}} \int\limits_{M}^{\infty} \frac{d\sigma(M')}{dM'} dM'; \tag{2.4}$$

where M is multiplicity of reconstructed charged tracks. Using percentiles defined by Eqs. 2.3 and 2.4 event classes selected using multiplicity ($M \pm \Delta M$) can be mapped to a certain range of impact parameter ($b \pm \Delta b$) as shown in Figs. 2.15 (right) and 2.16.

Centrality procedure described in this subsection is implemented in ROOT-based C++ Centrality framework [110]. Validation and maintenance of the Centrality package together with its interface co-development is a part of current doctoral work.

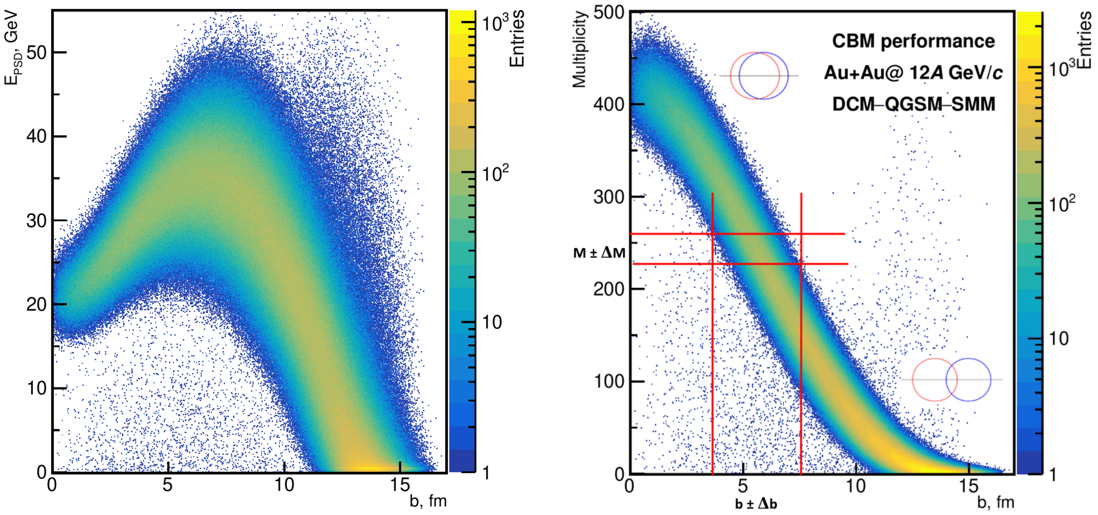

Figure 2.15: Correlation between impact parameter and (**left**) energy deposit in PSD, (**right**) multiplicity of registered charged tracks.

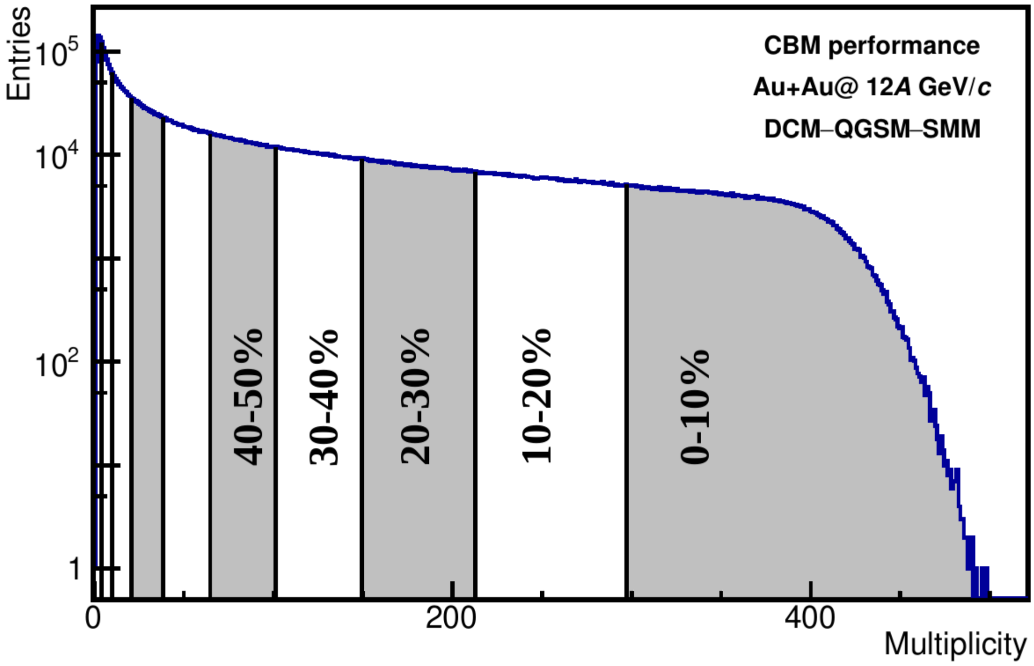

Figure 2.16: Charged tracks multiplicity distribution, divided into centrality classes.

2.4 CBM simulation setup

Simulations were performed for gold-gold collisions at the lowest and the highest SIS-100 beam momenta of $3.3A\,\mathrm{GeV}/c$ and $12A\,\mathrm{GeV}/c$ respectively. Two event generators were used for heavy-ion collision simulations in current doctoral work: DCM-QGSM-SMM and UrQMD. More details can be found in Sec. 1.4.3.

CBM geometry includes following elements: magnet, MVD, STS, RICH, TRD, TOF and PSD. PSD is located in 870 cm from the target. It consists of 44 modules with 20 cm hole in its center. The target is 25 μm thick golden foil.

The following software was used for simulations:

FairSoft [111] - external software required by FairRoot. Version jun19p1 was used.

FairRoot [112] - C++ based simulation, reconstruction and analysis framework for particle physics experiments at FAIR. Version 18.2.1 was used.

CbmRoot [113] - C++ based simulation, reconstruction and analysis framework designed specifically for CBM. Release APR20 was used.

Geant4 [114, 115, 116] (installed within FairSoft routines) - engine for the simulation of the transport of particles through detector material.

Tab. 2.2 summarizes simulation setups and software used for anisotropic flow study in this doctoral work.

System	Au+Au		
Setup shortcut	u-12	d-12	d-3
Model	UrQMD	DCM-QGSM-SMM	
p_{beam}, AGeV/c	12		3.3
Statistics	2M	5M	5.2M
CBM geometry	sis_100_electron		
Target	25 μm thick		
Magnet	v18a		
MVD	v17a_tr		
STS	v19a		
RICH	v17a_1e		
TRD	v17n_1e		
TOF	v16d_1e		
PSD	v18e		
Transport code	Geant4		
FairSoft	jun19p1		
FairRoot	18.2.1		
CbmRoot	APR20		

Table 2.2: Description of simulation setups and software used in current doctoral work.

Tab. 2.3, 2.4 show selection of input for TOF-based particles identification and centrality determination respectively.

Quantity	**Notation**	**Selection**
Quality of primary vertex reconstruction	χ^2_{vtx}	< 3
Distance from TOF hit to reconstructed track	$\Delta r_{\text{track}-\text{hit}}$	$< 1.5\,\text{cm}$
Track approach to the primary vertex	$\chi^2_{\text{track}-\text{vtx}}$	< 18

Table 2.3: Selection applied on events, tracks and hits for TOF-based PID.

Quantity	**Notation**	**Selection**
Track approach to the primary vertex	$\chi^2_{\text{track}-\text{vtx}}$	< 3
Number of hits	N_{hits}	≥ 4
Quality of track reconstruction	$\chi^2_{\text{track}}/ndf$	< 3
Pseudorapidity	η	$[0.2 - 6]$

Table 2.4: Selection applied on tracks for centrality estimation with charged tracks multiplicity.

Chapter 3

PFSimple package for decay reconstruction

Measurements of (multi-)strange particles and rare probes in CBM require tools for their reconstruction. Stable particles (electrons, positrons, (anti)protons, stable nuclei) and particles which pass through CBM tracking system before decay (muons, charged pions and kaons) are reconstructed with the tracking system as described in Sec. 2.3.1-2.3.2. Short-lived particles (Λ, Ξ^- and Ω^- baryons, K^0_S-mesons, D-mesons, resonances) are reconstructed from the products of their decay. CBM tools for decays reconstruction are online-oriented package Kalman Filter Particle Finder (KFParticleFinder) and physics analysis oriented package Particle Finder Simple (PFSimple). Development of the PFSimple package is a part of the current doctoral work.

This chapter describes online and offline decay reconstruction challenges in CBM (Sec. 3.1), the PFSimple package, its algorithm and data flow (Sec. 3.2) and application of the PFSimple package implemented for different physics analysis in CBM (Sec. 3.3).

3.1 Decay reconstruction challenges: online and offline

Decays reconstruction in CBM is challenging due to high interaction rate up to 10 MHz, large multiplicities of charged particles in the CBM acceptance (up to 1000 in central events at the top SIS-100 collision energy) and complex topology of decays, characterised by a large set of geometrical quantities (from here *topological variables*). These challenges are illustrated by the CBM event display in Fig. 3.1. Kalman filter based algorithms [117], which are required for decays reconstruction, are implemented in the KFParticle package [118]. Two complementary packages, based on the KFParticle package, for constructing decay candidates are developed in CBM: Kalman Filter Particle Finder (KFParticleFinder), designed to be used online during the data taking and the second one, Particle Finder Simple (PFSimple), which provides a convenient interface for optimization of the decays selection used in offline physics analysis.

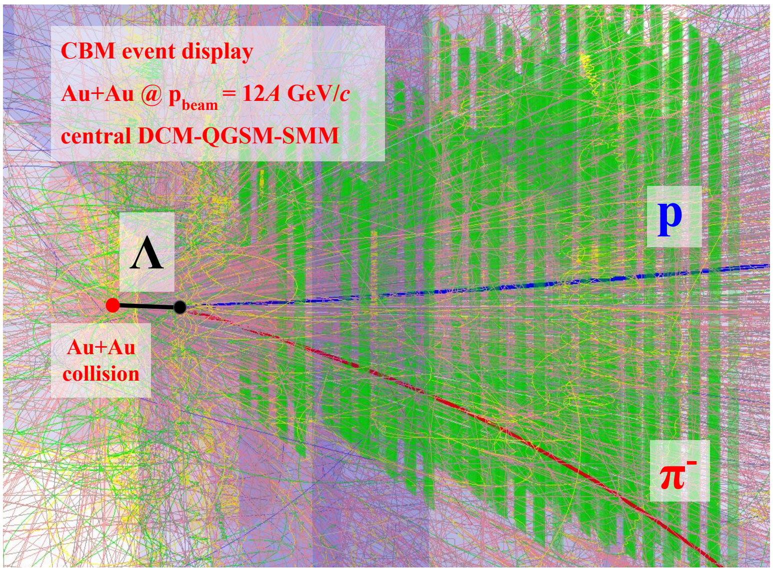

Figure 3.1: The CBM event display illustrating the multi-particle environment which complicates the hyperon decay reconstruction.

Digesting online events at the interaction rate up to 10 MHz and identification rare signals to make a decision to save the event require fast reconstruction algorithms executed online during data taking. KFParticleFinder reaches the speed by vectorization of calculations with "Single instruction, multiple data" approach [119] implemented in the VC library [120]. KFParticleFinder can simultaneously construct decay candidates for more than 150 channels including (multi)strange hadrons, low mass vector mesons, charmed particles, resonances, hypernuclei etc. KFParticleFinder is described in [121] and implemented as a part of the KFParticle package.

Offline analysis does not require very fast speed of numerical calculations, but requires best performance of reconstruction in terms of signal-to-background ratio or significance, which requires a flexible configuration depending on the decay channel, kinematic and event centrality. A package PFSimple [122] aims to fulfill these offline analysis requirements.

3.2 Algorithm, data flow and output format

3.2.1 KFParticle functionality

In the KFParticle a particle reconstructed by tracking system or by decay products is described with the state vector

$$\vec{r} = \{X, Y, Z, P_x, P_y, P_z, E\}, \tag{3.1}$$

where X, Y, Z are Cartesian coordinates of the particle, P_x, P_y, P_z - its momentum and E - energy. The uncertainties of state vector are represented with its covariance matrix $\hat{C}_{\vec{r}}$. KFParticle provides tools for operating with particles' state vectors and covariance matrices, among them the most relevant operations for PFSimple are:

- transportation the particle: calculation of state vector and covariance matrix of the particle along its trajectory in a non-homogeneous magnetic field;
- construction decay candidate: building a state vector and covariance matrix from two or more particles;
- invariant mass constraint: recalculation 4-momentum $\{P_x, P_y, P_z, E\}$ to place it on the mass shell;
- evaluation of square distance between two particles (or particle and a point) in terms of its error (dimensionless representation):

  $$\chi^2 = \Delta\vec{r}^T \hat{C}^{-1} \Delta\vec{r} = \sum_{i,j=x,y,z} C^{-1}_{ij} \Delta r_i \Delta r_j, \tag{3.2}$$

  where $\Delta\vec{r}$ is a vector connecting two particles (or particle and a point), $\hat{C}^{-1}$ - an inverted covariance matrix of the union of two particles (or a single particle).

3.2.2 PFSimple algorithm

Two-body decay

PFSimple reconstructs decays in each event using the primary vertex coordinates and tracks parameters:

- momentum and coordinates of the point where it is defined;
- covariance matrix for momentum and coordinates;
- charge of the track;
- parameters of the parabolic approximation of magnetic field components along track's trajectory;

- (optionally) particle type hypothesis of the track.

As example let us consider a two-body decay of Λ-baryon into proton and negatively charged pion. All possible pairs of positively and negatively charged tracks are considered. Positive (negative) tracks are assumed to be a proton (π^--meson). This assumption is implemented by calculating the state vector (Eq. 3.1) component as $E = \sqrt{\vec{p}^2 + m^2}$ with mass m of proton (pion) taken from the PDG [34]. Covariance matrix elements related to E are also calculated. Then both tracks are transported to points where they are closest to each other and combined into Λ-*candidate*, for which a state vector is calculated, from where momentum, invariant mass and spatial position of the candidate can be obtained. Candidates originating from real Λ decay are called *signal* and the rest - a *combinatorial background*, shortly just *background*. A combinatorial background for all available track pairs is huge. It can be reduced by iterating only over tracks identified as protons and π^--mesons (see Sec. 2.3.3). Another way of background suppression is a rejection of candidates with topological variables more often associated with background than with signal. Fig. 3.2 illustrates topological variables which characterize the two-body decay:

- DCA – a distance of the closest approach between two daughter tracks (in cm);
- $\cos\alpha_{\mathrm{md}}$ – a cosine of the angle between the mother candidate's and daughter's momenta;
- $L/\Delta L$ - a distance (L) between the primary and secondary vertices divided by its error (ΔL);
- $\chi^2_{\mathrm{prim,d}}$ – a dimensionless squared distance between daughter track and primary vertex, see Eq. 3.2;
- χ^2_{geo} – a dimensionless squared distance between two daughter tracks;

- χ^2_{topo} – a dimensionless squared distance between the Λ candidate trajectory and primary vertex.

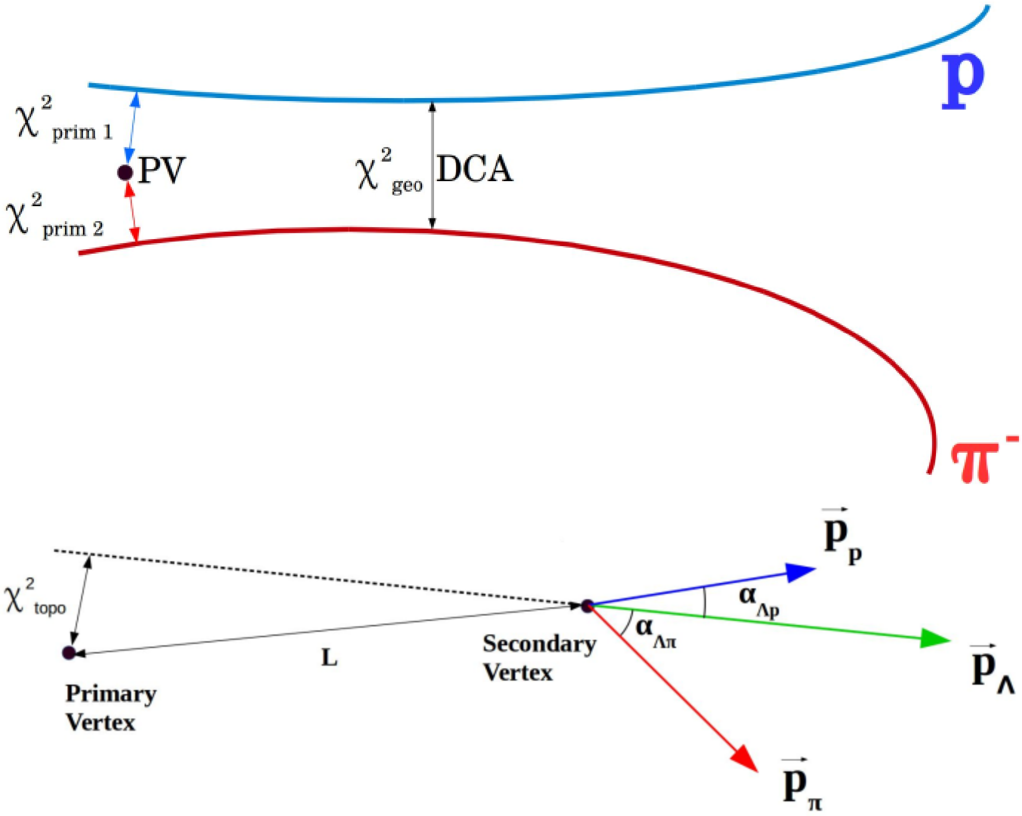

Figure 3.2: Schematic view of the $\Lambda \to p\pi^-$ decay which indicates topological variables used for the Λ candidate selection. See text for details.

PFSimple allows to select Λ-candidates with a desired topology. Fig. 3.3 illustrates the distribution of 5 topological variables - both for signal and background (background distribution is normalized to the same integral as signal). Rejection as much background as possible and in the same time preservation as much signal as possible are competing tasks. To find a compromise between background rejection and selection efficiency, a selection on topological variables has to be optimized. Selection optimization used in the current doctoral work is described in App. A. Selection optimization using machine learning techniques is discussed in Sec. 3.3.1.

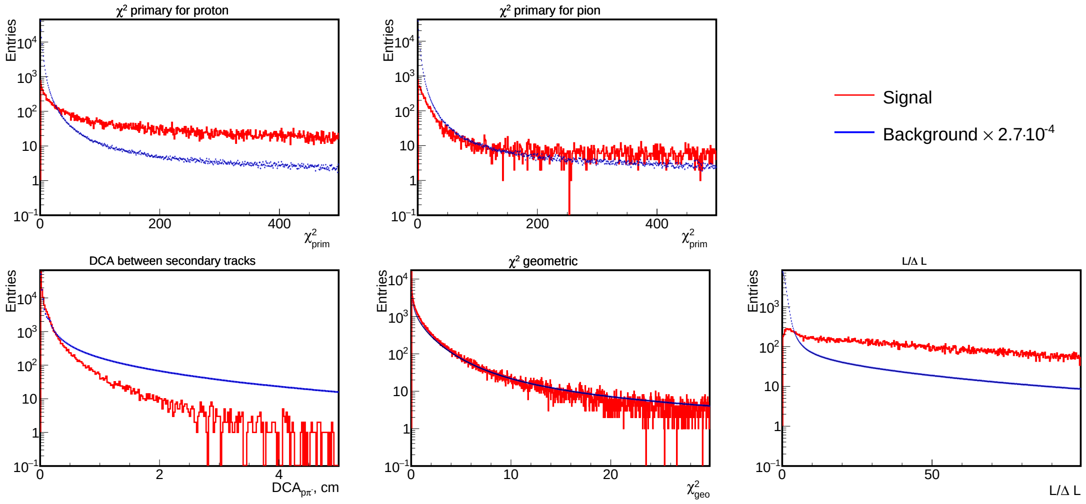

Figure 3.3: Distributions of the topological variables for $\Lambda \to p\pi^-$ candidates. No event or Λ candidate kinematical selection. Background (blue) is normalized to the same integral with signal (red).

Cascade decay

Reconstruction of Ξ^--baryon is done in two steps: first a $\Lambda \to p\pi^-$ decay (a daughter Λ), and then - a $\Xi^- \to \Lambda\pi^-$ decay are reconstructed. Topological variables describing cascade decay are similar to those of two-body decay, see Fig. 3.4. Cascade reconstruction has several additional features:

- the same daughter track is not participating in building both cascade and daughter Λ;
- only daughter Λs with invariant mass close to its PDG mass are used to construct cascade candidates;
- 4-momentum of the daughter Λ is set to its value on the mass shell.

3.2.3 Data flow and output format

PFSimple is agnostic to the input and output format. In current work both of them are represented by the *AnalysisTree* data format [123], based on ROOT

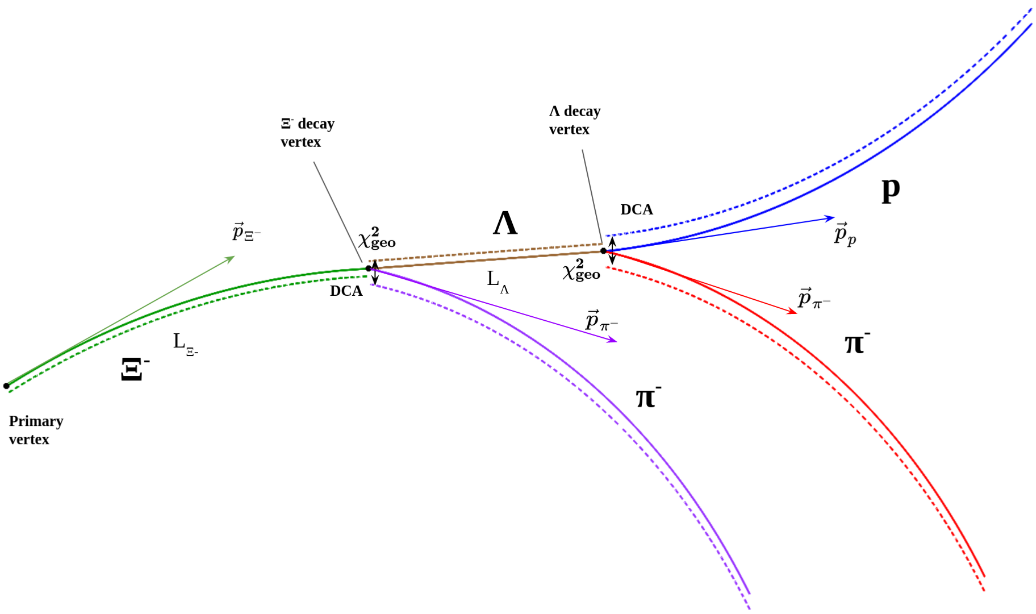

Figure 3.4: Schematic view of the $\Xi^- \to \Lambda\pi^-$; $\Lambda \to p\pi^-$ decay which indicates parameters used for the Ξ^- candidate selection. Solid and dashed lines denote real and reconstructed particles trajectories respectively. See text for details.

framework [124, 125]. Co-development of the AnalysisTree infrastructure and improving its flexibility in data storage are a part of the current doctoral work. The core of PFSimple algorithm described in Sec. 3.2.2 depends on the KFParticle package and input/output containers in internal PFSimple format. There is an AnalysisTree interface to PFSimple which consists of converters from AnalysisTree to PFSimple (input) and from PFSimple to AnalysisTree (output). PFSimple together with AnalysisTree interface are managed with PFSimple Manager in the following way:

1. Input converter transmits information for decays reconstruction (listed in Sec. 3.2.2) from input file to PFSimple.

2. PFSimple reconstructs decay candidates.

3. Output converter writes into the produced file information about reconstructed candidates: momentum, energy and topological variables.

4. For Monte-Carlo simulation a matching between reconstructed signal candidates and corresponding simulated particles is found and saved.

5. (Optionally) complementary to PFSimple data (e.g. event variables) is copied to the output file.

These steps are repeated for each event. Fig. 3.5 illustrates how PFSimple together with other packages operate with input data and produce the output. Dependencies are shown with red arrows and flow of data - with black arrows.

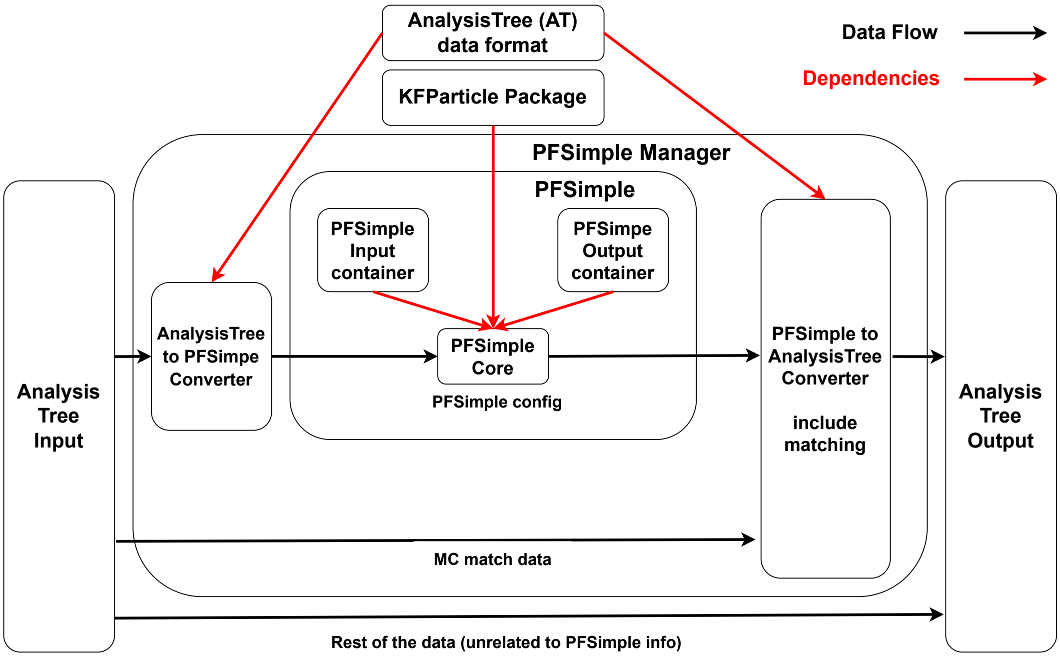

Figure 3.5: PFSimple and surrounding packages structure. Black and red lines show data flow and package dependencies respectively.

The output AnalysisTree file can be digested either with browser (Fig. 3.6, left) or using command line (Fig. 3.6, right). Data in this file can be histogrammed using AnalysisTree QA package [126]. Produced file can be used as an input for the consecutive physics analysis such as optimization of candidates selection (Sec. 3.3.1) or flow study (Sec. 3.3.3).

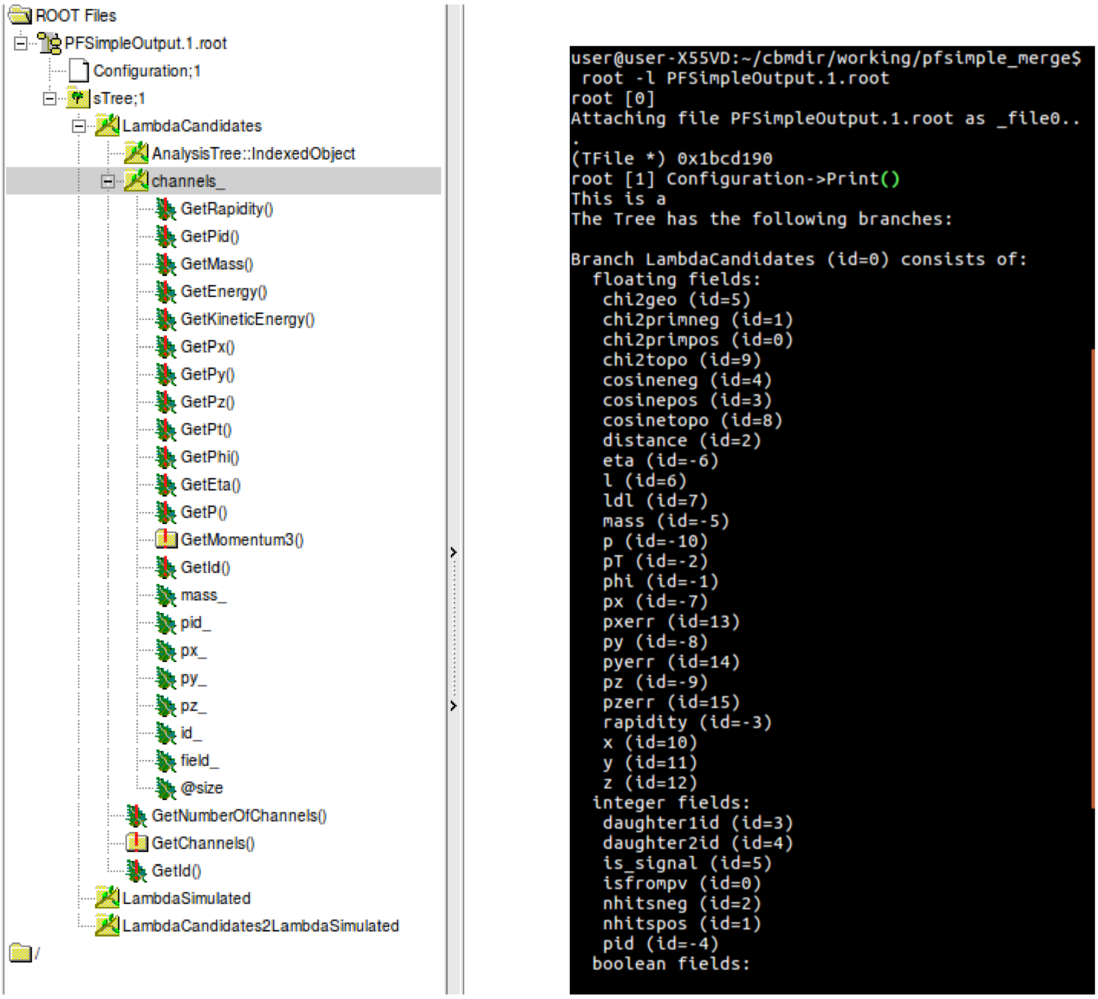

```
user@user-X55VD:~/cbmdir/working/pfsimple_merge$
 root -l PFSimpleOutput.1.root
root [0]
Attaching file PFSimpleOutput.1.root as _file0..
.
(TFile *) 0x1bcd190
root [1] Configuration->Print()
This is a
The Tree has the following branches:

Branch LambdaCandidates (id=0) consists of:
  floating fields:
   chi2geo (id=5)
   chi2primneg (id=1)
   chi2primpos (id=0)
   chi2topo (id=9)
   cosineneg (id=4)
   cosinepos (id=3)
   cosinetopo (id=8)
   distance (id=2)
   eta (id=-6)
   l (id=6)
   ldl (id=7)
   mass (id=-5)
   p (id=-10)
   pT (id=-2)
   phi (id=-1)
   px (id=-7)
   pxerr (id=13)
   py (id=-8)
   pyerr (id=14)
   pz (id=-9)
   pzerr (id=15)
   rapidity (id=-3)
   x (id=10)
   y (id=11)
   z (id=12)
  integer fields:
   daughter1id (id=3)
   daughter2id (id=4)
   is_signal (id=5)
   isfrompv (id=0)
   nhitsneg (id=2)
   nhitspos (id=1)
   pid (id=-4)
  boolean fields:
```

Figure 3.6: Output of the PFSimple package: (**left**) ROOT::TBrowser view, (**right**) terminal view.

3.3 Application for physics analysis at CBM

In this section examples of application of PFSimple package for physics analysis at CBM are discussed. Implementations described in Sec. 3.3.1 and 3.3.2 were developed by members of the CBM collaboration with assistance of the author of current doctoral work. Application described in Sec. 3.3.3 was developed as a part of current doctoral work.

3.3.1 Λ, K_S^0 and Ξ^- decays selection with machine learning

Distribution of topological variables constitutes a multi-dimensional phase space, where variables are correlated between each other. A linear selection (so-called box cuts) is not optimal for signal to background ratio or significance. This is illustrated in Fig. 3.7 where signal and background are distributed in 2-dimensional phase space $A-B$. If one applies a selection on variable A (right from vertical line in Fig. 3.7, left), then a similar amount of background and signal is rejected. If a selection is applied on variable B (up from horizontal line in Fig. 3.7, middle), then better separation between signal and background is achieved, but still one loses some signal and some background remains. If one performs transformation of coordinates and applies selection on a combination of A and B (up from diagonal line in Fig. 3.7, right) then the best result is achieved. Topological variables form a multi-dimensional space (up to 7 for two-body decay and 14 for cascades), and they are not necessarily correlated linearly as shown in Fig. 3.7. It is difficult to optimize a separation between signal and background manually, but it is a common task for machine learning techniques.

PFSimple performs reconstruction of all decays without selection. Set of candidates is used as an input for the decision tree implemented in XGBoost package [127, 128]. Topological variables are input parameters of the decision tree. As a target variable a Monte-Carlo flag signal/background is used. After training

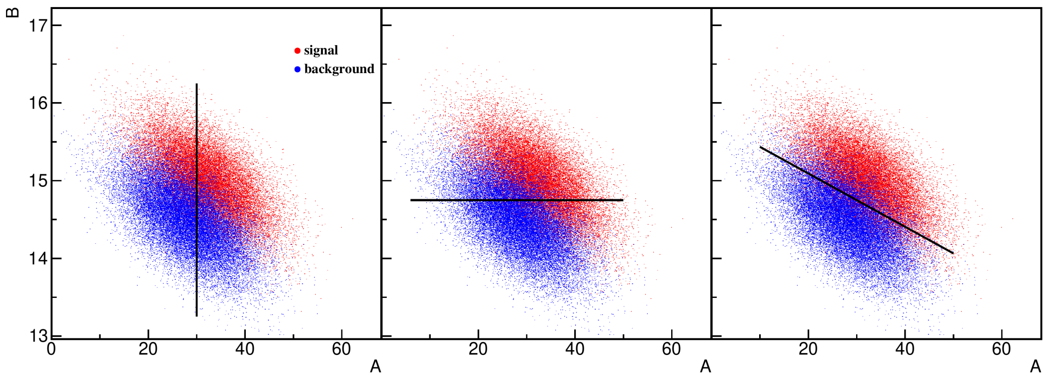

Figure 3.7: Distribution for a toy Monte-Carlo simulation of signal (red) and background (blue) in arbitrary 2-dimensional phase space $A - B$ with selection (**left**) on A, (**middle**) on B, (**right**) both on A and B.

and testing the decision tree, the model maps a single number (so-called XGBoost score) between 0 and 1 to the vector of input parameters. The closer score is to 1 the higher probability that candidate is signal, see Fig. 3.8, left. The model is a non-linear transformation of multi-dimensional phase space of input parameters into 1-dimensional unity segment with signal and background concentrated at opposite sides. A selection of candidates is done by scanning the threshold of XGBoost score in order to find an optimum between background rejection and signal efficiency. Fig. 3.8, right, illustrates comparison of Λ-candidates reconstruction with one-dimensional selection on topological variables and multi-dimensional XGBoost-based selection. As one can see XGBoost gives better performance both in background rejection and signal efficiency.

Decays reconstruction with machine learning techniques is described more detailed in [130].

3.3.2 Hypernuclei reconstruction

At top SIS-100 energies a high amount of hypernuclei will be produced [89]. Reconstruction of hypernuclei via three-body decay was added into PFSimple by CBM collaboration members [131]. The reconstruction of a three-body decay

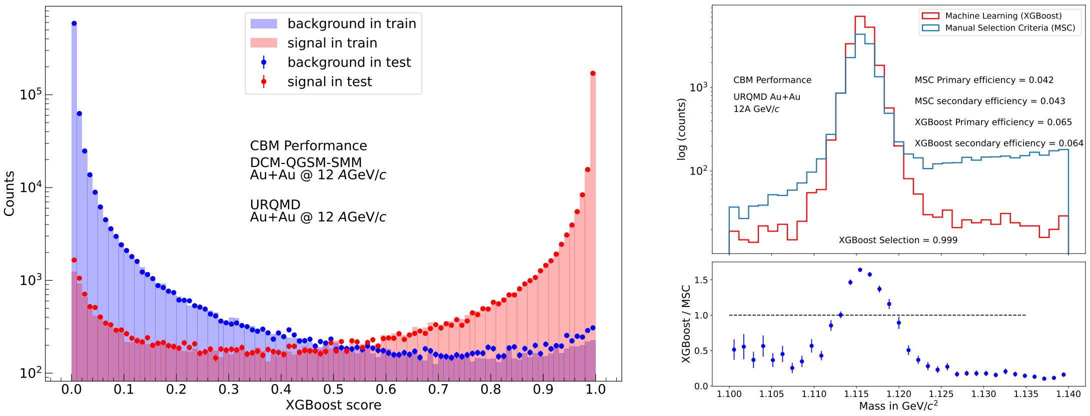

Figure 3.8: (**left**) Distribution of XGBoost score for signal and background, (**right**) Λ-baryon invariant mass distribution: comparison of XGBoost (red) and box cuts (blue) selection performance [129].

in PFSimple is implemented in two steps. First, a *temporary* mother of two daughters is reconstructed at their point of closest approach. Second, the third daughter is added to the secondary vertex of temporary mother. Topological variables are calculated for each pair of three daughter tracks and selection on them can be applied.

Performance of PFSimple for hypertritons reconstruction at CBM was tested using the PHQMD model [68] which includes formation of nuclei and hypernuclei. Fig. 3.9, left, shows invariant mass distribution of ${}^{3}_{\Lambda}\mathrm{H} \to d + p + \pi^{-}$ decay. An efficiency of 26% and signal-to-background ratio of 0.24 are achieved for central events at $\sqrt{s_{NN}} = 4.9\,\mathrm{GeV}$. Fig. 3.9, right, shows reconstruction efficiency as a function of transverse momentum and rapidity, which has a maximum at midrapidity.

3.3.3 Λ, K^0_S and Ξ^- candidates construction for flow study

PFSimple is used for (multi-)strange hadrons flow study, which is the main topic of the current thesis. In Tab. 3.1-3.2 the selection criteria of two-body and cascade candidates used for flow analysis are presented. For two-body the selection

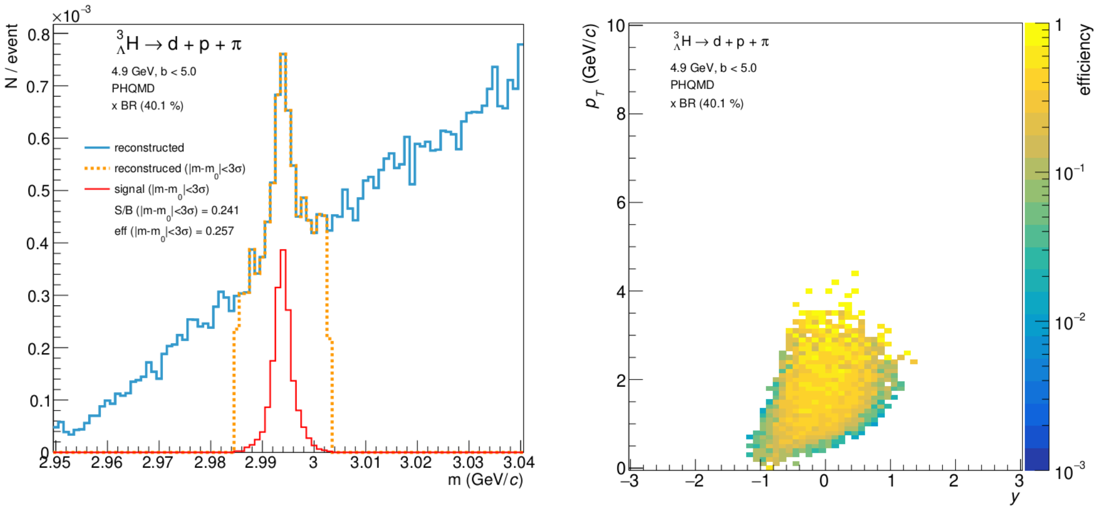

Figure 3.9: PFSimple performance for ${}^{3}_{\Lambda}\mathrm{H} \to d + p + \pi^-$ reconstruction: (**left**) invariant mass distribution, (**right**) reconstruction efficiency as a function of $p_T - y$ [132].

criteria differ with beam momentum and particles species; in the column "Default" the selection criteria optimized within [121] and present in [113] are shown. For cascade Ξ^- decays selection criteria are common for both beam momenta and coincide with those which were optimized within [121] and present in [113].

Fig. 3.10 illustrates the output of PFSimple decays reconstruction for the DCM-QGSM-SMM @ $12A\,\mathrm{GeV}/c$ simulation with selection criteria specified in Tab. 3.1 (column "Default") and Tab. 3.2. Λ-baryons, K^0_S-mesons and Ξ^--baryons are shown in left, middle and right columns respectively. Top row shows the invariant mass distribution of decay candidates. A signal peak on a top of smoothly distributed background can be clearly seen. Signal peak broadening is due to a finite momenta resolution. A shape of combinatorial background is a convolution of daughters momenta and angle between them. It does not have structures because it is formed by random pairs of independent particles. Middle and bottom rows of Fig. 3.10 illustrate reconstruction efficiency of (multi)strange particles as a function of $p_T - y$ and $p_T - \varphi$ respectively. Reconstruction efficiency is defined

Value	**12*A* GeV/*c***	**3.3*A* GeV/*c***		**Default**
	Λ, K^0_S	Λ	K^0_S	
$\chi^2_{\text{prim,pos}}$	> 3	> 24	> 65	> 18.4
$\chi^2_{\text{prim,neg}}$			> 50	
χ^2_{geo}	< 10	< 7	< 8	< 3
DCA	$< 1.5\,\text{cm}$	$< 0.15\,\text{cm}$		$< 1\,\text{cm}$
$L/\Delta L$	> 3	> 3.8	> 4.2	> 5
$\cos\alpha_{\text{pos}}$	-	> 0.995	-	-
χ^2_{topo}	-	< 18	< 35	-

Table 3.1: Neutral particles (Λ-baryons and K^0_S-mesons) selected for anisotropic flow study: numerical values of conditions for topological variables. "Default" column denotes numerical values of conditions for topological variables optimized within [121] and present in [113].

Value	**Intermediate V0**	**Cascade itself**
$\chi^2_{\text{prim,pos(V0)}}$	> 18.4	> 15
$\chi^2_{\text{prim,neg}}$	> 18.4	
χ^2_{geo}	< 3	< 6
DCA	$< 1\,\text{cm}$	
$L/\Delta L$	> 10	> 5
χ^2_{topo}	-	< 5
$\lvert m_{\text{inv}} - m_{\text{PDG}}\rvert$	$< 3\sigma_{m_{\text{inv}}}$	-

Table 3.2: Cascade particles (Ξ^--baryons) selected for anisotropic flow study: numerical values of conditions for topological variables. $\sigma_{m_{\text{inv}}} = 1.5\cdot 10^{-3}\text{GeV}/c^2$. V0 denotes a neutral daughter of the cascade.

as a ratio between number of reconstructed particles and number of particles simulated by event generator. These distributions are not uniform due to detector asymmetries, and this has to be taken into account for the anisotropic flow evaluation as discussed in Sec. 4.1.

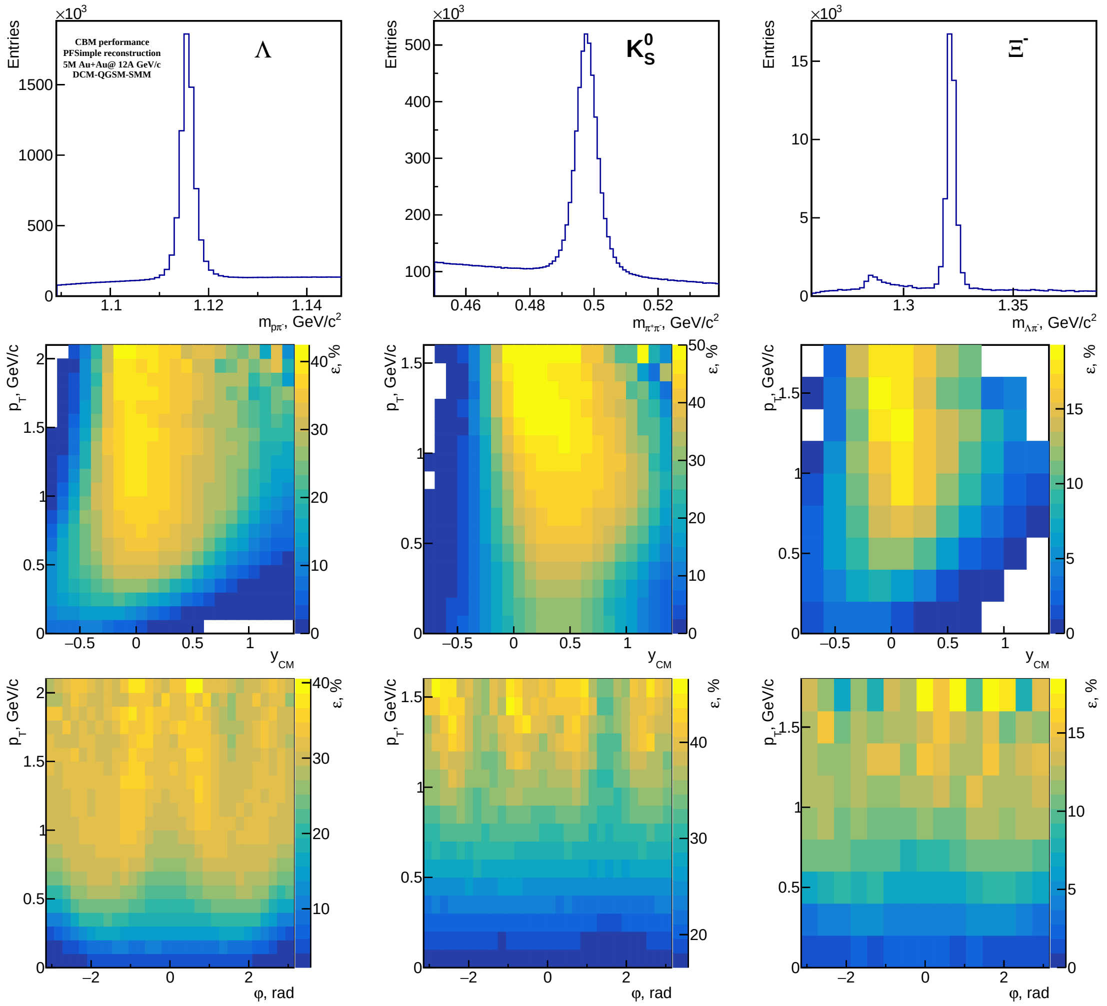

Figure 3.10: PFSimple reconstruction output for (**left**) Λ-baryons, (**middle column**) K^0_S-mesons, (**right**) Ξ^--baryons: (**top**) invariant mass distribution; reconstruction efficiency as a function of transverse momentum and (**middle row**) rapidity, (**bottom**) azimuthal angle. The input is generated with DCM-QGSM-SMM model at $12A\,\text{GeV}/c$.

Chapter 4

Flow measurement technique

4.1 Flow vector formalism and corrections for detector non-uniformity

Anisotropic flow coefficients defined by Eq. 1.5 are evaluated from correlation between azimuthal angles of particles in the final state of HIC. For this a flow vector $\mathbf{Q}_n$ given by a weighted sum of unit vectors $\mathbf{u}_n$ of particles is used:

$$\mathbf{u}_n = \{\cos n\varphi,\ \sin n\varphi\}, \quad \mathbf{Q}_n = \sum_{i=1}^{N} w_i \mathbf{u}_{n,i}. \tag{4.1}$$

Here φ is an azimuthal angle of i-th particle, n is a harmonic number, w_i is a weight of i-th particle. Flow vector $\mathbf{Q}_n$ can be normalized by its magnitude, sum of weights, square root of sum of weights.

A distribution of $\mathbf{Q}_n$ vectors azimuthal angle for a large set of events should be uniform from symmetry considerations. Because of detector's material non-uniformities and magnetic field this distribution is not uniform. Fig. 3.10, bottom, illustrates non-uniformity of (multi-)strange hyperons reconstruction efficiency as a function of azimuthal angle. Effect of this non-uniformity of $\mathbf{Q}_n$-vector can be corrected in three steps according to the procedure described in [133]:

- recenter distribution of $\mathbf{Q}_n$-vectors to their average;
- twist of $\mathbf{Q}_n$-vectors to align the distribution along axes of coordinate system;
- rescale of $\mathbf{Q}_n$-vector components to have the same average magnitude in x and y directions.

Schematically this procedure is illustrated in Fig. 4.1.

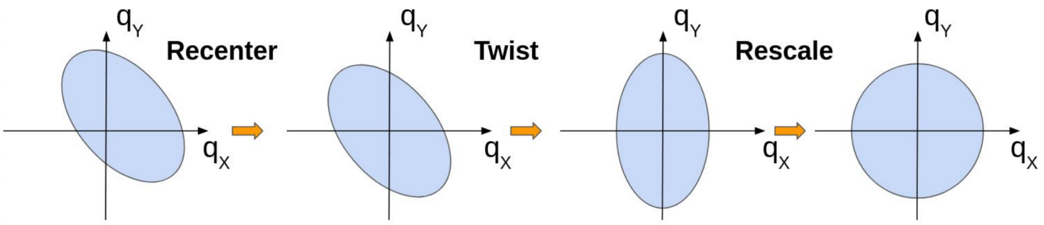

Figure 4.1: Schematic illustration of recenter, twist and rescale correction steps.

There are non-uniformities in $p_T - y$ directions which also can bias the $\mathbf{Q}_n$ vectors distribution. Fig. 3.10, middle row, illustrate non-uniformity of (multi-)strange hyperons reconstruction efficiency in $p_T - y$ directions. To correct this effect, unit vector of i-th particle is added with a weight w_i equal to inverse reconstruction efficiency $\varepsilon_i(p_T, y)$. Efficiency is calculated using Geant4 Monte-Carlo simulations. $\mathbf{Q}_n$-vectors distributions and numerical values of corrections are shown in App. B.

4.2 Event plane and scalar product methods

Evaluation of flow coefficients with Eq. 1.5 requires to know the reaction plane angle Ψ_{RP} and azimuthal angle φ of particles, flow of which is an object to study. From here we will name them *observed* particles. Angle Ψ_{RP} can be estimated experimentally from a set of particles kinematically separated from observed particles. Particles used for estimation of the reaction plane are called *reference* particles. Reaction plane angle can be estimated by the event plane angle, Ψ^n_{EP}:

$$\Psi^n_{\mathrm{EP}} = \frac{1}{n}\mathrm{atan2}(Q^n_y, Q^n_x), \tag{4.2}$$

where $\mathbf{Q}_n$ is a flow vector of reference particles. Since the set of reference particles is finite, the estimation of the reaction plane by Eq. 4.2 is never perfect but has some resolution which is needed to be obtained. Resolution correction factor is defined as

$$R_n = \langle \cos n(\Psi^n_{\mathrm{EP}} - \Psi_{\mathrm{RP}}) \rangle \tag{4.3}$$

Nucleons and fragments which do not participate in the collision (spectators) are deflected outwards from the beam line [134, 135] and can serve for the reaction plane estimation. In case of hadronic calorimeter (PSD) the azimuthal angle in Eq. 4.1 is defined by the center of PSD module with its signal used as a weight. The resolution correction factor can be evaluated using 3-subevent method using subsets of reference particles, marked A, B, C, which are correlated between each other via common reaction plane. This assumes a factorization of averaged product of $\mathbf{Q}_n$-vectors of subevents:

$$\langle \mathbf{Q}^A_n \mathbf{Q}^B_n \rangle = \langle \mathbf{Q}^A_n \mathbf{\Psi}^{\mathrm{RP}}_n \rangle \langle \mathbf{Q}^B_n \mathbf{\Psi}^{\mathrm{RP}}_n \rangle, \tag{4.4}$$

where $\mathbf{Q}^{A(B)}_n$ is a $\mathbf{Q}_n$-vector of subevent A(B) and $\mathbf{\Psi}^{\mathrm{RP}}_n$ is a unit vector along the reaction plane. 3 subevents are calculated for 3 different subsets of PSD modules (inner, middle and outer) as shown in Fig. 2.12. Using Eq. 4.4 one obtains an expression for resolution corrector factor R^A

$$R^A_{n,\alpha} = \sqrt{\frac{\langle Q^A_{n,\alpha} Q^B_{n,\alpha} \rangle \langle Q^A_{n,\alpha} Q^C_{n,\alpha} \rangle}{\langle Q^B_{n,\alpha} Q^C_{n,\alpha} \rangle}}, \tag{4.5}$$

where α stands for x, y component of $\mathbf{Q}_n$-vectors.

The main assumption expressed in Eq. 4.4 may not be fulfilled because of correlation between neighbouring subevents. To suppress those correlations an additional subset of particles can be used as 4-th subevent (marked as D): e.g. particles produced in the collision far enough from projectile spectators in kinematic space. The formulae for resolution correction factor are modified to:

$$R^B_{n,\alpha} = \frac{\langle Q^B_{n,\alpha} Q^D_{n,\alpha} \rangle}{R^D_{n,\alpha}}, \quad R^D_{n,\alpha} = \sqrt{\frac{\langle Q^A_{n,\alpha} Q^D_{n,\alpha} \rangle \langle Q^C_{n,\alpha} Q^D_{n,\alpha} \rangle}{\langle Q^A_{n,\alpha} Q^C_{n,\alpha} \rangle}}, \tag{4.6}$$

where B is corresponding to the middle PSD subevent.

With resolution correction factor the flow coefficient v_n is given by the following formula:

$$v_{n,\alpha} = \frac{2\langle q_{n,\alpha} Q_{n,\alpha} \rangle}{R_{n,\alpha}}, \tag{4.7}$$

where $\mathbf{q}_n$ is a flow vector of observed particles, normalized by sum of weights (in case of unity weights - by multiplicity), and $\mathbf{Q}_n$ is a flow vector of reference particles.

The equations for v_n when $\mathbf{Q}_n$ of reference particles is normalized by its magnitude, represent the *event plane* method. The flow coefficient v_n fluctuates from event to event [136]. In case of flow fluctuations, according to [137], the flow coefficient obtained by Eq. 4.7 is equal to $\langle v_n \rangle$ in case of high resolution ($R \approx 1$) and to $\sqrt{\langle v_n^2 \rangle}$ in case of low resolution ($R << 1$). This makes the flow measurement with the event plane method difficult to compare to the theoretical predictions. The *scalar product* method can be used to avoid this. It differs from the event plane method by normalization of $\mathbf{Q}_n$-vector by its sum of weights. As shown in [137] in this case $v_n = \sqrt{\langle v_n^2 \rangle}$ independently on the resolution. In this work the flow coefficients are calculated using scalar product method.

4.3 Uncertainty calculation

Statistical uncertainties

Eq. 4.7 for the flow coefficient contains $\mathbf{Q}_n$-vectors of observed and reference particles in different subevents. Statistical uncertainty can be calculated using *error propagation* or *bootstrap*. Statistical uncertainty of $f(x, y, z, ...)$ calculated using error propagation is defined as:

$$\sigma_f = \sqrt{\left(\frac{\partial f}{\partial x}\right)^2 \sigma_x^2 + \left(\frac{\partial f}{\partial y}\right)^2 \sigma_y^2 + \left(\frac{\partial f}{\partial z}\right)^2 \sigma_z^2 + ...} \tag{4.8}$$

In this approach it is difficult to take into account the partial correlation between variables. To take into account correlation of variables a bootstrap technique of statistical uncertainty evaluation is applied [138].

Systematic uncertainties

Eq. 4.7 for flow measurement gives two independent estimations from $\mathbf{Q}_n$-vectors x- and y-components. There are three estimators of the reaction plane based on different subevents. Thus one has a set of 6 independent estimators of the flow coefficients. For the results presented in this thesis, the v_n is calculated as an average over all estimators, and systematic uncertainty is estimated as a standard deviation of results for different estimators.

Corrections of $\mathbf{Q}_n$-vectors (Sec. 4.1), event plane and scalar product methods (Sec. 4.2) and statistical uncertainties estimation via bootstrap (Sec. 4.3) are implemented in ROOT-based C++ framework QnTools [139], which is connected to AnalysisTree-based input with QnAnalysis [140] interface. Within current doctoral work the QnAnalysis package was validated, its automatic installation and bootstrap sampling were improved.

4.4 Signal extraction with invariant mass fit

Candidates of strange hyperons contain combinatorial background with its own flow, different from signal. A procedure to extract signal's flow is based on invariant mass-based separation between signal and background. We consider flow coefficient as a function of invariant mass of strange hyperon decay given by the equation:

$$v_{n,\mathrm{ALL}}(m_{\mathrm{inv}}) = \frac{v_{n,\mathrm{S}} N_{\mathrm{S}}(m_{\mathrm{inv}}) + v_{n,\mathrm{BG}}(m_{\mathrm{inv}}) N_{\mathrm{BG}}(m_{\mathrm{inv}})}{N_{\mathrm{S}}(m_{\mathrm{inv}}) + N_{\mathrm{BG}}(m_{\mathrm{inv}})}, \tag{4.9}$$

where $v_{n,\mathrm{ALL}}(m_{\mathrm{inv}})$ is a measured flow coefficient of all candidates, $v_{n,\mathrm{S}}$ is a flow coefficient of hyperons independent on invariant mass, $v_{n,\mathrm{BG}}$ is an invariant mass dependent flow coefficient of background candidates; $N_{\mathrm{S(BG)}}$ - yield of signal (background) candidates as a function of invariant mass. $v_{n,\mathrm{BG}}(m_{\mathrm{inv}})$ depends on invariant mass smoothly, in current work a linear dependence is considered. Yields of signal and background are determined by fitting the invariant mass distribution of selected candidates. A double-sided Crystal Ball function [141] is used for signal:

$$u(x) = \frac{x-\mu}{\sigma}, \quad f(u) = A \times \begin{cases} e^{-\frac{a_1^2}{2}} \cdot (1 - \frac{a_1(u+a_1)}{n_1})^{-n_1}, \ u < -a_1 \\ e^{-\frac{u^2}{2}}, \ -a_1 < u < a_2 \\ e^{-\frac{a_2^2}{2}} \cdot (1 + \frac{a_2(u-a_2)}{n_2})^{-n_2}, \ u > a_2, \end{cases} \tag{4.10}$$

which is a stitch of Gaussian peak and power law tails. Free parameters of this function are:

- A - common factor;
- μ - mean value of Gaussian function;
- σ - standard deviation of Gaussian function;

- $a_{1(2)}$ - distance in terms of σ between the point where Gaussian peak transits to left (right) tail and Gaussian mean value;
- $n_{1(2)}$ - power index of power law left (right) tail.

Background is assumed to have no structures and is fitted with a third order polynomial. Fig. 4.2 (top) illustrates fitting of invariant mass of $\Lambda \to p\pi^-$ (left) and $K^0_S \to \pi^+\pi^-$ (right).

Then v_n as a function of invariant mass fitting is performed with free parameters $v_{n,\mathrm{S}}$ and coefficients of $v_{n,\mathrm{BG}}$ linear dependence on m_{inv}. Fig. 4.2 (bottom) illustrates fitting of $v_1(m_{\mathrm{inv}})$ of Λ (left) and K^0_S (right).

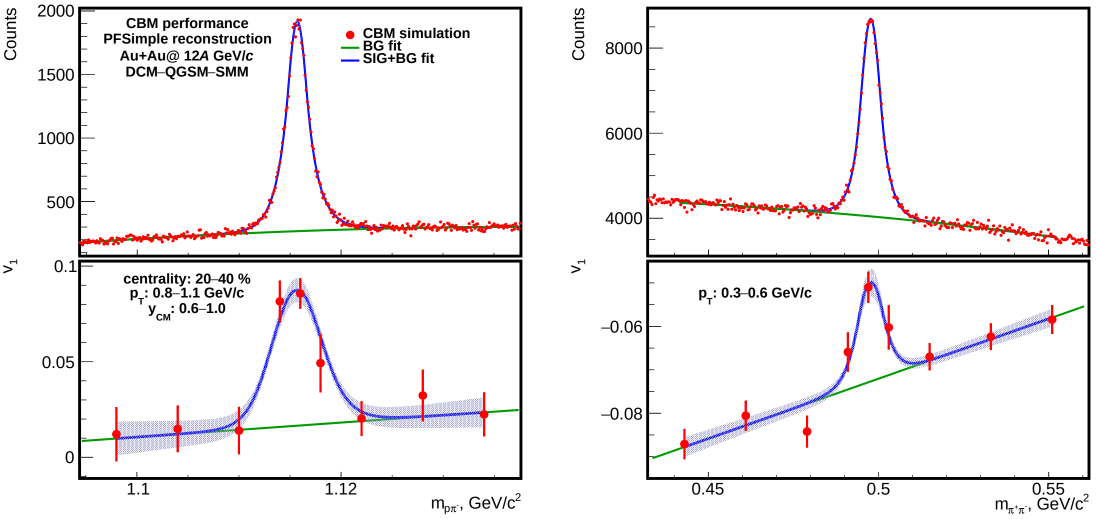

Figure 4.2: (**top**) Invariant mass distribution of (**left**) $\Lambda \to p\pi^-$ and (**right**) $K^0_S \to \pi^+\pi^-$, fitted with a combination of the double-sided Crystal Ball function (SIG) and 3-d order polynomial (BG). (**bottom**) Directed flow of (**left**) Λ and (**right**) K^0_S vs. invariant mass, fitted using Eq. 4.9.

4.5 dv_1/dy slope extraction

Directed flow of Λ and Ξ^- baryons and K^0_S-mesons is evaluated according to the procedure described in Sec. 4 as a function of rapidity and transverse momentum and collision centrality. The dependence of v_1 on rapidity is condensed by linear fit $v_1(y) = ky + b$ where $k = dv_1/dy$ is a slope of $v_1(y)$ and $b = v_1|_{y=0}$ is its value at midrapidity (see Fig.4.3, left). When $v_1(y)$ dependence is not linear, higher order terms are also introduced to the fitting function (see Fig.4.3, right).

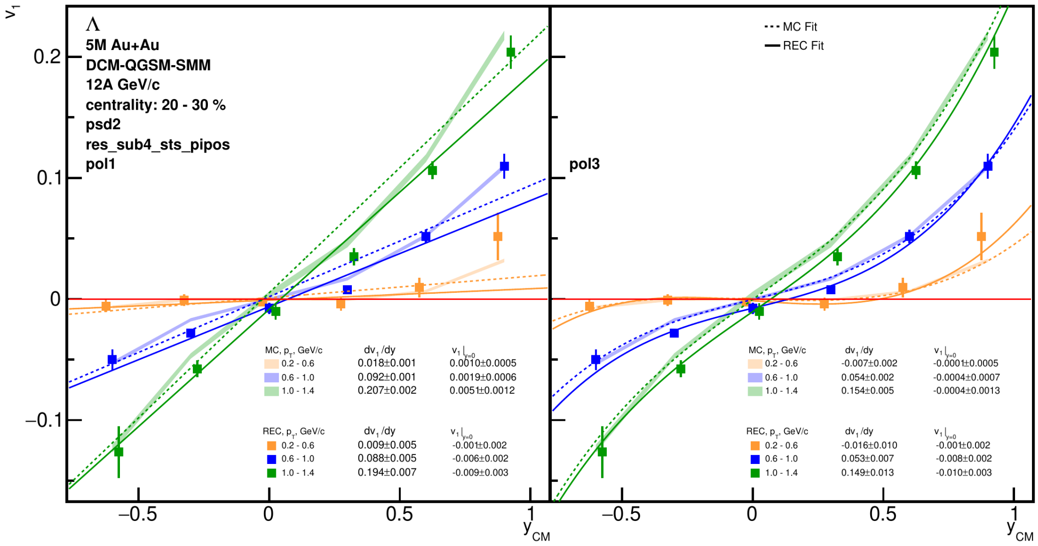

Figure 4.3: $v_1(y)$ of Λ-baryons calculated relative to spectators registered in PSD2 with resolution determined via 4-subevents method. The input is generated with DCM-QGSM-SMM @12A GeV/c. MC-true input (filled areas) and reconstructed values (markers) are fitted with (**left**) linear fit, (**right**) 3-d order polynomial function with quadratic term fixed to zero.

Within the current doctoral work an invariant mass fit method (Sec. 4.4) and dv_1/dy slope extraction (Sec. 4.5) are implemented in QnTools extension - QnDiscriminator [142].

4.6 Global polarization calculation

Hyperon's spin projection can be accessed via its weak decay. Let us illustrate it with an example of $\Lambda \to p\pi^-$ decay, but this approach can be applied for other (multi)-strange baryons.

In case of fully polarized Λ-hyperons the angular distribution of emitted proton is given by equation [143]:

$$\frac{dW}{d\Omega} = \frac{1}{4\pi}(1 + \alpha_\Lambda \cos\theta), \tag{4.11}$$

where $dW/d\Omega$ is a probability density, Ω is a solid angle, $\alpha_\Lambda = 0.732 \pm 0.014$ [34] is the asymmetry parameter of decay and θ is an angle between Λ polarization vector and direction of proton's momentum in the rest frame of Λ. In case of partially polarized Λ-baryons, taking into account Eq. 1.7, the Eq. 4.11 transforms into

$$\frac{dW}{d\Omega} = \frac{1}{4\pi}(1 + \alpha_\Lambda P_\Lambda \cos\theta^*), \tag{4.12}$$

where P_Λ is global polarization coefficient and θ^* is an angle between proton's momentum direction and angular momentum of the system measured in the rest frame of Λ. $\cos\theta^*$ can be expressed as

$$\cos\theta^* = \sin\theta_p^* \sin(\phi_p^* - \Psi_{\mathrm{RP}}), \tag{4.13}$$

where angles notations are presented in Fig. 4.4. Replacing $\cos\theta^*$ in Eq. 4.12 with r.h.s. of Eq. 4.13 and integrating over θ_p^* one obtains

$$\frac{dW}{d\phi_p^*} = \frac{1}{2\pi}(1 + \frac{\pi\alpha_\Lambda P_\Lambda}{4} \sin(\phi_p^* - \Psi_{\mathrm{RP}})). \tag{4.14}$$

Averaging $\sin(\phi_p^* - \Psi_{\mathrm{RP}})$ using Eq. 4.14 gives

$$P_\Lambda = \frac{8}{\pi\alpha_\Lambda}\langle\sin(\phi_p^* - \Psi_{\mathrm{RP}})\rangle. \tag{4.15}$$

Since polarization of Λ-hyperon can be measured via distribution of daughter proton, this decay is called *self-analyzing*.

Eq. 4.15 is similar to Eq. 1.5, therefore techniques used for flow analysis (Sec. 4.2, 4.4) can be applied for polarization measurement.

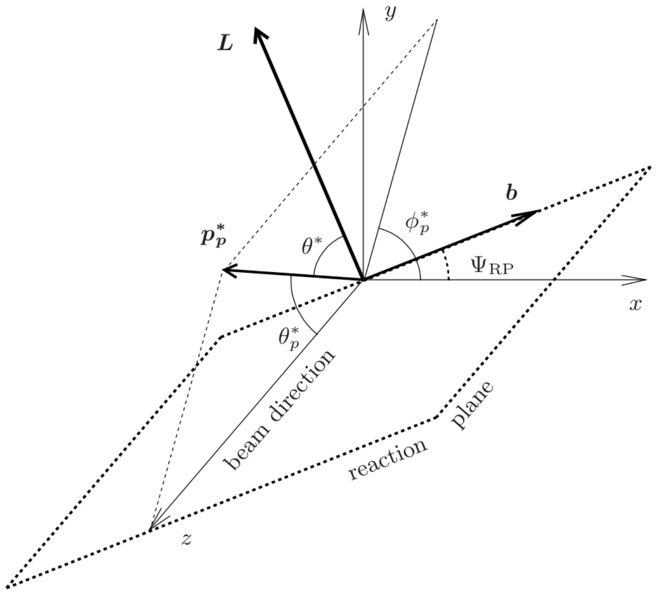

Figure 4.4: Scheme showing notations used in global polarization determination. z-axis is lying along beam axis, xy is a plane transverse to the beam direction. $\vec{b}$ is impact parameter vector, $\vec{L}$ is angular momentum vector perpendicular both to z-axis and $\vec{b}$, $\vec{p}_p$ is momentum of proton in hyperon rest frame. θ^* is an angle between $\vec{p}_p$ and $\vec{L}$, θ_p^* - between $\vec{p}_p$ and z-axis, ϕ_p^* - between $\vec{p}_p$ and x-axis (azimuthal angle of proton), Ψ_{RP} - between $\vec{b}$ and x-axis (reaction plane angle) [47].

Chapter 5

Results

In this chapter a performance of the CBM experiment for directed flow and global polarization measurements of (multi-)strange hadrons is presented. Firstly, two-body and cascade decays reconstruction with PFSimple is studied in terms of signal-to-background ratio and reconstruction efficiency as a function of transverse momentum and rapidity. Invariant mass spectra of $\Lambda \to p\pi^-$, $K^0_S \to \pi^+\pi^-$, $\Xi^- \to \Lambda\pi^-$, $\Omega^- \to \Lambda K^-$ decays are obtained together with signal-to-background ratios. Efficiency and background rejection are compared with and without TOF particles identification. Performance with and without MVD detector is compared for Λ-baryons and K^0_S-mesons. $p_T - y$ reconstruction efficiency maps are built for Λ, K^0_S and Ξ^-, which illustrate the CBM acceptance, characteristic maximal values of the reconstruction efficiency and position of its maximum depending on the collision energy. Secondly, the performance for resolution correction factor evaluation, directed flow coefficient calculation and extraction of directed flow slope is presented with an example of Λ-baryons and K^0_S-mesons as the most abundant strange particles at FAIR energies. Sources of systematic uncertainties together with their quantitative impact are studied. Finally, projections of statistical uncertainties of directed flow and global polarization for (multi-)strange hadrons are calculated for expected high-statistics measurements.

5.1 Performance for two-body and cascade decay reconstruction

Results with and without TOF particle identification

Fig. 5.1 illustrates the PFSimple performance for two-body and cascade decays reconstruction without PID (pure topological reconstruction), TOF PID and MC-true PID as a reference (when a particle's type of reconstructed track is determined from matching it with a particle, simulated by event generator or transport). Background suppression with TOF is significant ($\approx 35\%$) and loss of signal is small (efficiency $\approx 95\%$) for two-body decays of Λ and K^0_S. Background suppression of about $\approx 40\%$ with efficiency $\approx 90\%$ is achieved for Ξ^- with TOF PID. Signal-to-background ratio without PID is too small to observe Ω^- signal. TOF PID allows to reject $\approx 99.9\%$ of background because Ω^- baryon decay contains kaon, which is rare relative to protons and pions; identification of K^- reduces combinatorial background dramatically. An efficiency of Ω^--baryon reconstruction with TOF PID is $\approx 25\%$[1]. An optimization of PID selection is important for optimal background rejection and reconstruction efficiency. Tab. 5.1 summarizes the PFSimple reconstruction performance for two-body and cascade decays in different PID modes.

Performance with and without MVD

Fig. 5.2 illustrates PFSimple performance for two-body decays reconstruction with (in red) and without (in blue) MVD detector in CBM setup. Invariant mass spectrum collected with MVD was normalized on the same number of events as without MVD. The MVD allows to reconstruct $\approx 40\%$ more signal for two-body

---

[1] Tracks unmatched to TOF-hits (and thus unidentified) are usually considered as daughter tracks in decays reconstruction. However, it is not the case for K^- tracks in Ω^- decay reconstruction since consideration of all unmatched tracks as kaons increases combinatorial background by factor of 300.

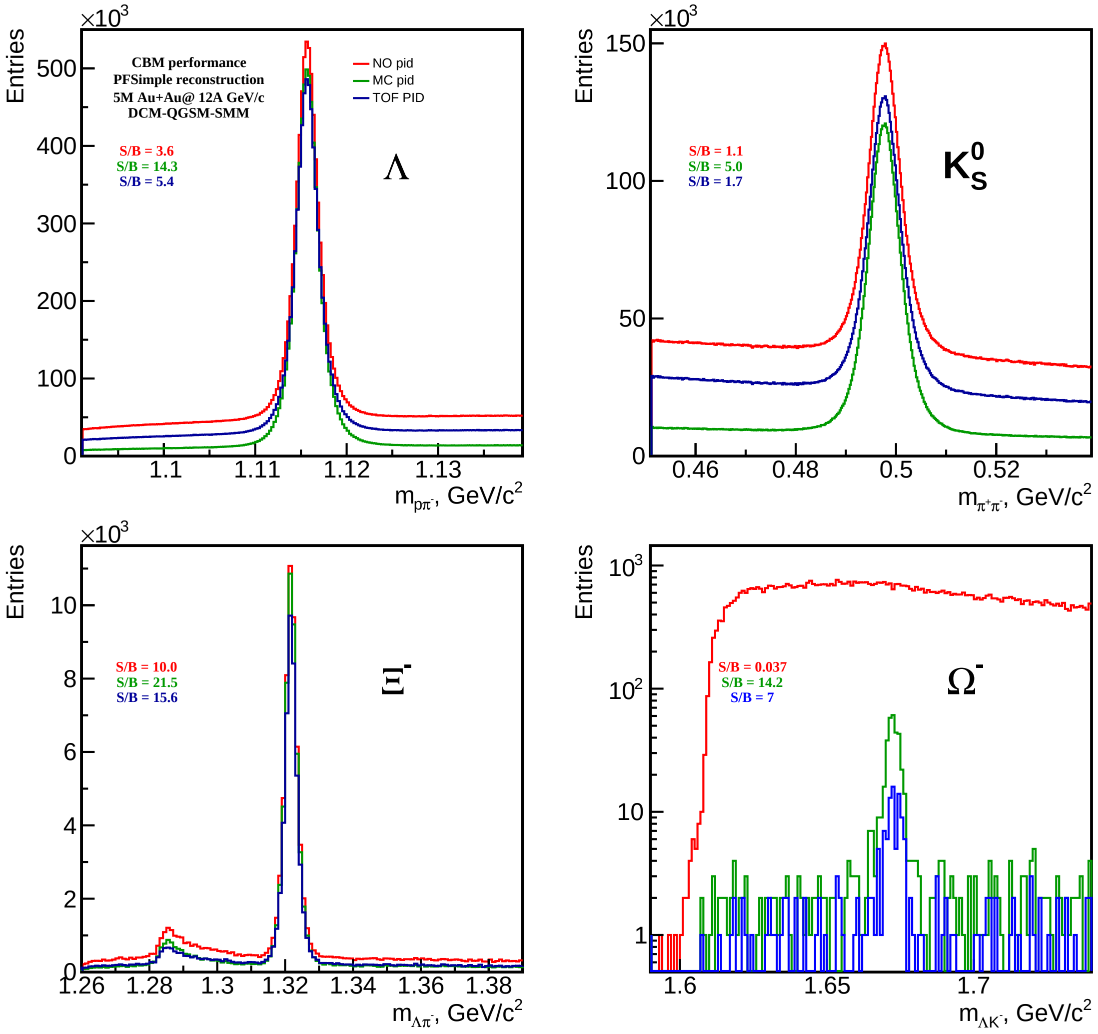

Figure 5.1: PFSimple performance for two-body and cascade decays reconstruction if different PID modes: invariant mass spectra of (**top left**) $\Lambda \rightarrow p\pi^-$, (**top right**) $K^0_S \rightarrow \pi^+\pi^-$, (**bottom left**) $\Xi^- \rightarrow \Lambda\pi^-$, (**bottom right**) $\Omega^- \rightarrow \Lambda K^-$. The input is generated with DCM-QGSM-SMM at $12A\,\mathrm{GeV}/c$.

decays while combinatorial background grows by $\approx 30\%$, so signal-to-background ratio changes only by few percents. In case of usage of MVD the width of the peak is $\approx 11\%$ and $\approx 15\%$ narrower for Λ and K^0_S respectively. The MVD is not critically important for two-body strange particles decays reconstruction performance in contrast to particles with decay length of hundreds of micrometers (e.g. D-mesons).

Decay	ε, %	BR, %	B(TOF/MC)
$\boldsymbol{\Lambda \to p\pi^-}$	94	37	2.5
$\boldsymbol{K^0_S \to \pi^+\pi^-}$	95	36	2.9
$\boldsymbol{\Xi^- \to \Lambda\pi^-}$	88	43	1.2
$\boldsymbol{\Omega^- \to \Lambda K^-}$	24	99.9	0.5

Table 5.1: PFSimple performance for two-body and cascade decays reconstruction with TOF-based PID: efficiency $\varepsilon = S_{TOF}/S_{NO}$ as a fraction of preserved signal of available in absence of PID, background rejection $BR = 1 - B_{TOF}/B_{NO}$ as a fraction of rejected background due to usage of TOF-based PID, ratio $B(TOF/MC)$ between background in case of TOF PID and MC (ideal) PID.

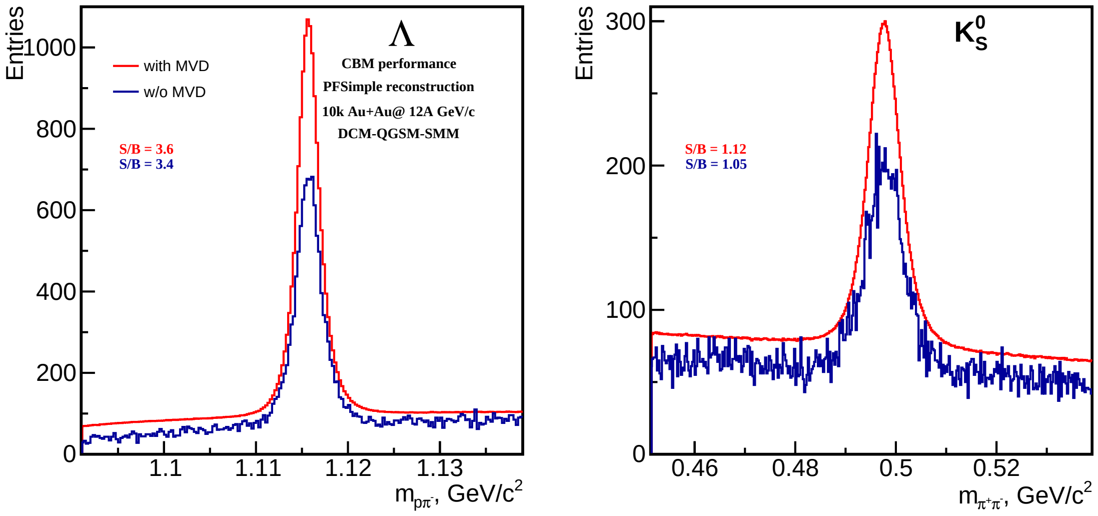

Figure 5.2: PFSimple performance for two-body decays reconstruction with and without Micro-Vertex Detector: invariant mass spectra of (**left**) $\Lambda \to p\pi^-$, (**right**) $K^0_S \to \pi^+\pi^-$. The input is generated with DCM-QGSM-SMM at $12A\,\mathrm{GeV}/c$. No PID hypothesis on decay products applied.

$p_T - y$ dependence of reconstruction efficiency

PFSimple reconstruction efficiency as a function of $p_T - y$ is shown in Fig. 5.3 for Λ, K^0_S and Ξ^- for the highest ($12A\,\mathrm{GeV}/c$) and the lowest ($3.3A\,\mathrm{GeV}/c$) SIS-100 beam momenta. Only bins populated enough to extract reconstruction efficiency are shown (relative statistical error less than 35% for Ξ^- at $3.3A\,\mathrm{GeV}/c$ and 10%

for the rest).

Reconstruction efficiency at the highest and the lowest beam momenta reaches values up to 50% for Λ and K^0_S, and up to 20% for Ξ^-. In case of the highest beam momentum the maximum of reconstruction efficiency is located near midrapidity, while at the lowest beam momentum the maximum is shifted to forward rapidities ($y = 0.7 - 1$). Also for the lowest beam momentum the reconstruction efficiency at midrapidity and backward rapidity is quite low, especially for $p_T > 0.5\,\mathrm{GeV}/c$.

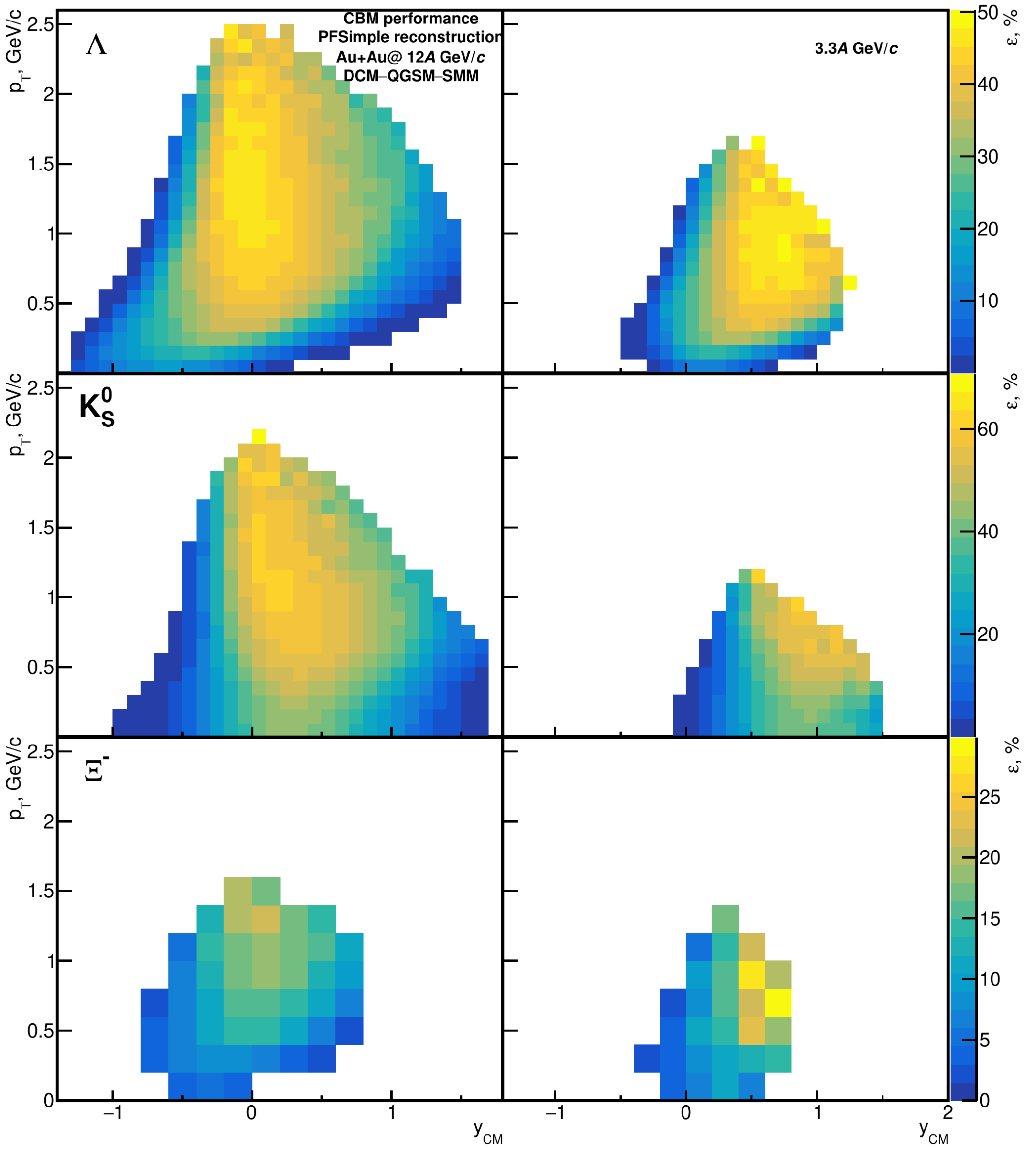

Figure 5.3: $p_T - y$ dependence of reconstruction efficiency of (**top**) Λ, (**middle**) K_S^0, (**bottom**) Ξ^- at beam momentum (**left**) 12A GeV/c, (**right**) 3.3A GeV/c. Only bins where reconstruction efficiency is defined with relative statistical error less than 10% (for Ξ^- at 3.3A GeV/c - 35%) are shown.

5.2 Sources of azimuthal correlations and systematic uncertainties

5.2.1 Non-flow, momentum conservation, and flow fluctuations

Calculations of flow coefficients (Sec. 4.2) assume azimuthal correlations of particles only due to their correlation with the reaction plane. However, there are other sources of azimuthal correlations, which include short-range femtoscopy and resonance decays, momentum conservation, flow fluctuations imposed by the fluctuating nucleon positions [144, 145, 146].

Short-range correlations and resonance decays

There are femtoscopic correlations between particles with close momenta: quantum statistics of identical particles, Coulomb and strong interactions. Many hadrons produced in HIC originate from resonance decays such as $\rho \to \pi^+\pi^-$ or Δ-resonance decaying into nucleon and pion. Momenta of short-range correlated particles are not independent but defined by their interaction. In the same time decay products of resonances are correlated due to decay kinematic considerations. Short-range correlations contribute to correlation between $\mathbf{Q}_n$-vectors in calculation of flow coefficients and resolution correction factor (Eqs. 4.5-4.7)). These correlations are called *non-flow*.

Since non-flow mainly involves few particles, its contribution scales inversely proportional to the multiplicity of produced particles. Therefore non-flow has stronger impact in peripheral collisions (where multiplicity is small) and in central collisions (where flow itself is small due to geometry of the collision). A dependence on multiplicity (centrality) can be used to subtract non-flow from measured flow coefficient. Since non-flow correlations have significant impact only for particles with close momenta, non-flow can be also suppressed by increasing rapidity gap between correlated particles. Another way to suppress short-range correlations is a multi-particle method [147].

Momentum conservation

Momentum conservation imposes a constrain on the the azimuthal distribution of produced particles and spectators which results in an additional correlation between particles. As shown in [145, 148] azimuthal angles of two particles which do not have any correlation between each other except of due to momentum conservation fulfill following condition:

$$\langle \cos(\varphi_1 - \varphi_2) \rangle = -\frac{p_{T1} p_{T2}}{N \langle p_T^2 \rangle}, \tag{5.1}$$

where $\varphi_{1,2}$ are azimuthal angles of two selected particles, $p_{T1,2}$ are their transverse momenta, N is a total multiplicity, $\langle p_T^2 \rangle$ is an average square transverse momentum of all particles. Momentum conservation contribution, Δv_1, to the directed flow coefficient is proportional to:

$$\Delta v_1 \sim -\frac{p_T}{N \langle p_T^2 \rangle} f, \tag{5.2}$$

where f is a coefficient proportional to square root of fraction of reference particles among total multiplicity of produced particles and spectators. From Eqs. 5.1, 5.2 one can see that momentum conservation shifts down measured directed flow coefficient, therefore directed flow at midrapidity $v_1|_{y=0}$ is non-zero as it should be for symmetry considerations, see Fig. 5.4 (left). This shift is stronger for particles with higher p_T and in peripheral events with lower multiplicity N, see Fig. 5.4 (middle). Momentum conservation cannot be eliminated by rapidity gap between observed and reference particles. For experiments with symmetric acceptance in rapidity, shifts of v_1 (Eq. 5.2) measured relative forward- and backward-rapidity

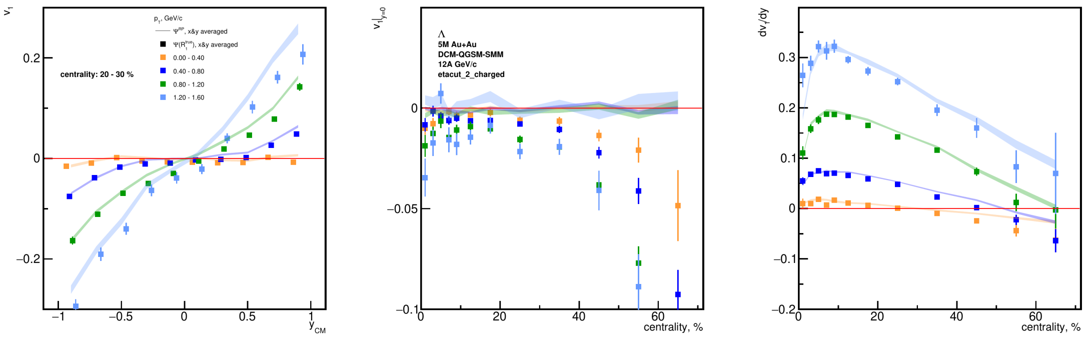

Figure 5.4: Directed flow of simulated Λ-baryons with reaction plane estimated using charged fragments in the acceptance of middle PSD submodule (PSD2): (**left**) directed flow v_1 as a function of rapidity, (**middle**) directed flow offset $v_1|_{y=0}$ as a function of centrality, (**right**) directed flow slope dv_1/dy as a function of centrality. Solid lines represent MC-true input. The input is generated with DCM-QGSM-SMM @ $12A\,\mathrm{GeV}/c$.

reference particles compensate each other. Momentum conservation does not affect a slope of v_1 as shown in Fig. 5.4 (right). A model-dependent approach to correct for momentum conservation in flow measurements is to subtract term defined in Eq. 5.2 [148].

Flow fluctuations

Traditionally, the anisotropic flow introduced in Sec. 1.4.2 is considered in a purely geometrical picture (Fig. 1.10): solid spherical nuclei and a reaction plane defined by beam axis and impact parameter connecting nuclei centers. However, the picture of heavy-ion collision is more complicated. Nucleons are distributed by Woods-Saxon [149] and their positions fluctuate from event to event, see Fig. 5.5 (left, middle). The shape of the overlap region is distorted, and the main axis of the participant zone does not coincide with that of the reaction plane, see Fig. 5.5 (right). Fluctuations in nucleon positions lead to anisotropic flow fluctuations from event to event even for the same impact parameter. One of the observables,

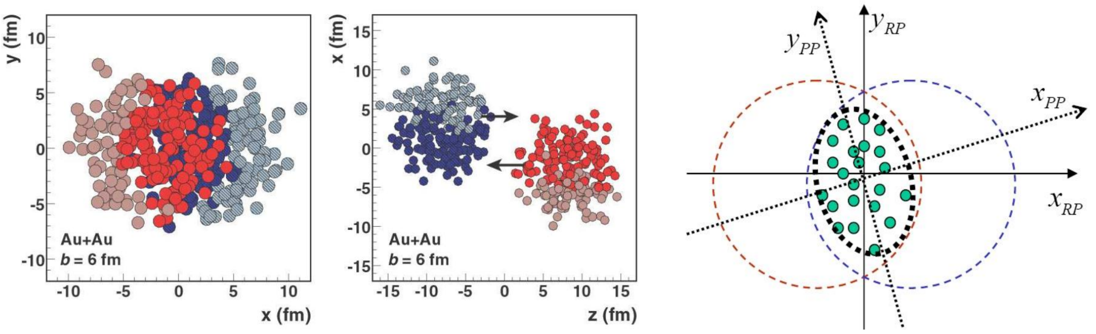

Figure 5.5: MC-Glauber generated event (Au+Au, $\sqrt{s_{NN}} = 200\,\text{GeV}$, $b = 6\,\text{fm}$) in (**left**) transverse plane and (**middle**) along beam axis. Participant nucleons are shown with dark colors [149]; (**right**) illustration of the reaction plane and participants plane [144].

which characterizes flow fluctuations, is:

$$\sigma^2_{v_n} = \langle v_n^2 \rangle - \langle v_n \rangle^2, \tag{5.3}$$

where $\langle ... \rangle$ is an average over events. The event plane method gives the following estimate of anisotropic flow: $v_n\{EP\} = \langle v_n^\alpha \rangle^{1/\alpha}$, with α varying from 1 in case of high resolution to 2 in case of low resolution, while the scalar product method gives $v_n\{SP\} = \langle v_n^2 \rangle^{1/2}$ independently on resolution [137].

5.2.2 Overlapping acceptance of STS and PSD and transverse spread of hadronic showers in PSD

Auto-correlations

When acceptances of detector subsystems which register observed and reference particles are overlapping, then the same particle can contribute to both $\mathbf{q}_n$ and $\mathbf{Q}_n$ vectors in Eq. 4.7. In this case the observed particle is correlated with itself (so called *auto-correlation*). A similar situation happens when a decay product of observed particle is present in the acceptance of reference particles detector.

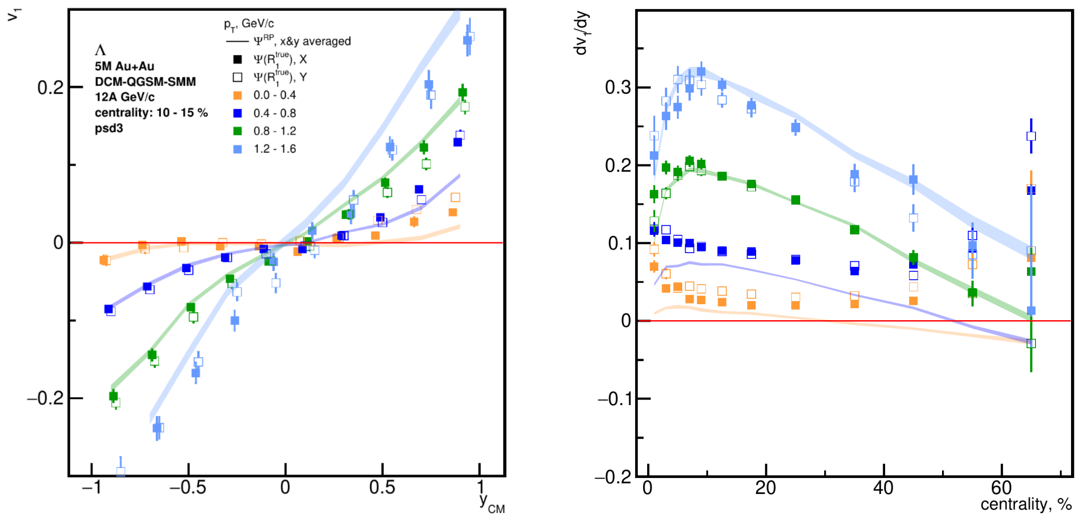

Figure 5.6: (**left**) Directed flow v_1 as a function of rapidity, (**right**) directed flow slope dv_1/dy as a function of collision centrality calculated for simulated Λ-hyperons with reaction plane estimated using 3-d submodule of the PSD.

Fig. 5.6 (left) illustrates an effect of auto-correlation on the directed flow of Λ-hyperons with $p_T < 0.8\,\mathrm{GeV}/c$. In the forward rapidity region $y \approx 1$ there is a significant difference between reconstructed and MC-true values of v_1, which is interpreted as a correlation of Λs with protons from their decay registered in the PSD. No effect is observed in the backward rapidity region $y \approx -1$. This effect is stronger for central and peripheral events and weaker in mid-central collisions. This is because a lower amount of spectators registered in the PSD in central (due to geometry reasons) and peripheral (where they are lost in the PSD hole) collisions makes the relative contribution of the proton from Λ decay higher. This bias can be reduced by avoiding kinematic phase space where acceptances of STS and PSD overlap (e.g. exclude low p_T forward rapidity hyperons when estimating reaction plane with an outer PSD subevent).

Transverse spread of the hadronic shower

When a nucleon or a charged fragment hits in the PSD module, it produces a hadronic shower which spreads both in longitudinal and in transverse direction. Shower spread across multiple modules leads to the correlation between $\mathbf{Q}_n$-vectors which is not due to common reaction plane and breaks the factorization assumption (Eq. 4.4) of $\mathbf{Q}_n$-vectors in resolution correction factor determination. As one can see in Fig. 5.7 (left) the factorization is not fulfilled for subevents built from neighbour (1 and 2, 2 and 3) PSD submodules, but is present for 1 - 3 pair. This leads to a discrepancy in the resolution correction factor calculated with 3-subevent method (Sec. 4.2), as shown in Fig. 5.7 (middle). One can notice that discrepancy is stronger for the resolution of the middle submodule (PSD2) when neighbouring subevents are both in numerator in Eq. 4.5, and weaker for inner (PSD1) and outer (PSD3) submodules when neighbouring subevents in numerator and denominator partially compensate each other. In order to avoid this systematic uncertainty, an additional subevent from different kinematic region can be used (e.g. produced protons or pions registered with STS). The 4-subevent method is applied for resolution determination, using correlations of subevents between which neighbouring are not present. Fig. 5.7 (right) illustrates

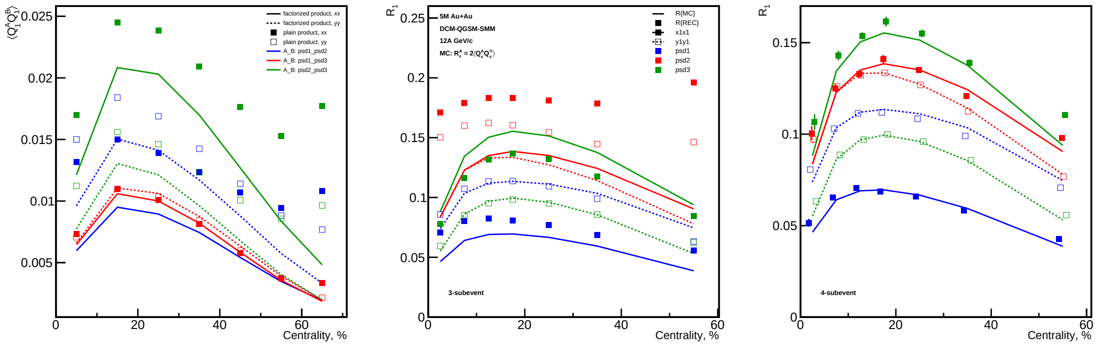

Figure 5.7: (**left**) $\langle Q_A Q_B \rangle$ factorization into $\langle Q_A \Psi_{\mathrm{RP}} \rangle \langle Q_B \Psi_{\mathrm{RP}} \rangle$; Comparison of resolution calculated using (**middle**) 3-subevent (**right**) 4-subevent method and MC-true resolution for reaction plane estimation.

an effect of using an additional subevent constructed from positively charged pions with $p_T \in [0;\ 1.4]$ GeV/c; $y \in [0.8; 1.2]$ which allows to suppress bias in the resolution correction factor evaluation compared to results with 3 subevents.

5.2.3 Non-uniformity of decay reconstruction efficiency

As illustrated in Sec. 3.3.3, decays reconstruction efficiency is not uniform and depends on rapidity, transverse momentum and azimuthal angle of the particle. Procedures introduced in Sec. 4.1 mostly correct these inefficiencies. Residual effects are due to the following reasons:

- In the current implementation, the statistical uncertainties of reconstruction efficiency and azimuthal corrections are not propagated. At near-zero p_T, where reconstruction efficiency changes rapidly, the granularity of the reconstruction efficiency map is not fine enough and requires MC simulations with higher statistics;

- In case of acceptance non-uniformities and presence of strong flow of observed particles of higher harmonics (e.g. elliptic flow v_2) the procedure described in [133] does not correct these inefficiencies. However, this effect is minor for flow calculations at CBM because of low values of both higher order harmonics of anisotropic flow at SIS-100 energies and higher order detector anisotropies.

Fig. 5.8 illustrates discrepancies between directed flow slope as a function of centrality calculated for reconstructed Λ-hyperons and MC-generated input. The differences are more significant for low transverse momentum. To improve the situation one needs to perform high-statistics Monte-Carlo simulations which would allow for multi-differential study of the distribution and correlation of $\mathbf{q}_n$-vectors.

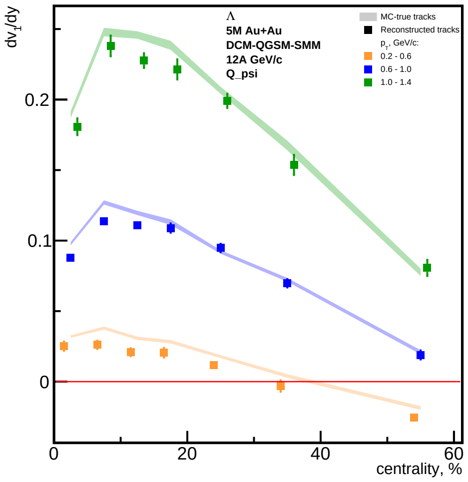

Figure 5.8: dv_1/dy of Λ-hyperons as a function of centrality: comparison of MC-tracks (filled lines) and reconstructed tracks (markers). Flow is calculated relative to MC-true reaction plane angle.

5.2.4 Parametrizations used in invariant mass fit method

Flow evaluation described in Sec. 4.4 has an assumption about shape of signal and background, and invariant mass dependence of background candidates flow. The choice of a double sided Crystal Ball function to fit signal distribution can bias the result of the invariant mass fit method.

This was found to have less significant impact compared to the rest sources of systematic uncertainties. In Fig. 5.9 the performance of invariant mass fit method is shown for three different HIC event generators and collision energy setups. Invariant mass fit procedure was not applied to Λ-hyperons for DCM-QGSM-SMM, $p_{\text{beam}} = 3.3A\,\text{GeV}/c$ due to the lack of statistics. Instead a high signal purity was achieved and flow coefficient was calculated for *all* Λ-candidates. It is also a fully data-driven approach where presence of background among all candidates stands for systematic uncertainties contributor. Within statistical uncertainties, the flow of signal evaluated with invariant mass fit method is consistent with calculations using MC-matching.

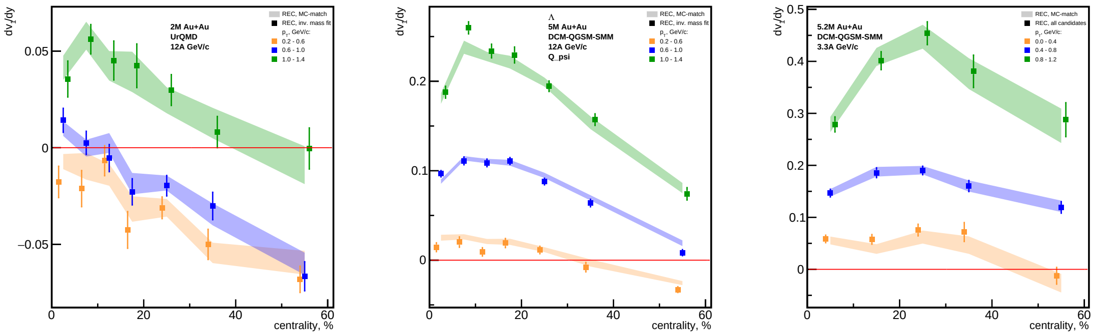

Figure 5.9: dv_1/dy of Λ-hyperons as a function of centrality: comparison of signal selected using MC-matching (filled lines) and extracted in data-driven approach (markers). The input is generated with (**left**) UrQMD, $p_{\text{beam}} = 12A\,\text{GeV}/c$, (**middle**) DCM-QGSM-SMM, $p_{\text{beam}} = 12A\,\text{GeV}/c$, (**right**) DCM-QGSM-SMM, $p_{\text{beam}} = 3.3A\,\text{GeV}/c$. Flow is calculated relative to MC-true reaction plane angle.

5.3 Performance for measurement of Λ and K^0_S directed flow at different beam momenta

5.3.1 Reaction plane resolution correction

Both spectators and produced particles can enter the acceptance of the PSD. Spectators have different masses (unbound nucleons or fragments). The composition of particle types varies with kinematics. Heavy fragments generally are in the acceptance of PSD1, light fragments - in all modules, and produced particles (mainly pions) usually hit the PSD3 module. Heavy fragments with masses close to projectile nucleus are lost in the PSD hole.

Resolution correction factor R_1 is proportional to the directed flow of reference particles. It is driven by their directed flow convoluted with PSD response in the scalar product (SP) method. In the event plane (EP) method R_1 additionally depends on the multiplicity of reference particles and is equal to an average cosine of the angle between the reaction plane and its estimate. Directed flow of spectators is positive [134, 135] while that of $\pi^{\pm}$ is negative at low p_T, which together results in a non-trivial dependence of the PSD response as a function of pseudorapidity. Directed flow depends on collision centrality. It vanishes in central events due to absence of any anisotropy, reaches maximum in midcentral and decreases in peripheral events - due to decreasing the size of the fireball.

There are effects which smear signal registered in the PSD. Magnetic field deflects charged particles in x-direction according to particle's charge-to-mass ratio. Hadronic showers originating in a PSD module spread into neighbouring ones.

In the following paragraphs the resolution dependence on centrality in different PSD submodules and performance of resolution determination with subevents approach are discussed.

MC-true resolution

Fig. 5.10 illustrates the centrality dependence of the MC-true resolution correction factor for the outer PSD submodule $R_1^{\mathrm{MC}}\{\mathrm{PSD3}\}$. Different event generators and beam momenta are compared. Left panel shows $R_1^{\mathrm{MC}}\{\mathrm{PSD3}\}$ calculated with normalization of Q_1-vectors by the sum of weights (SP) while right panel - with normalization by the magnitude (EP), for details see Sec. 4.2.

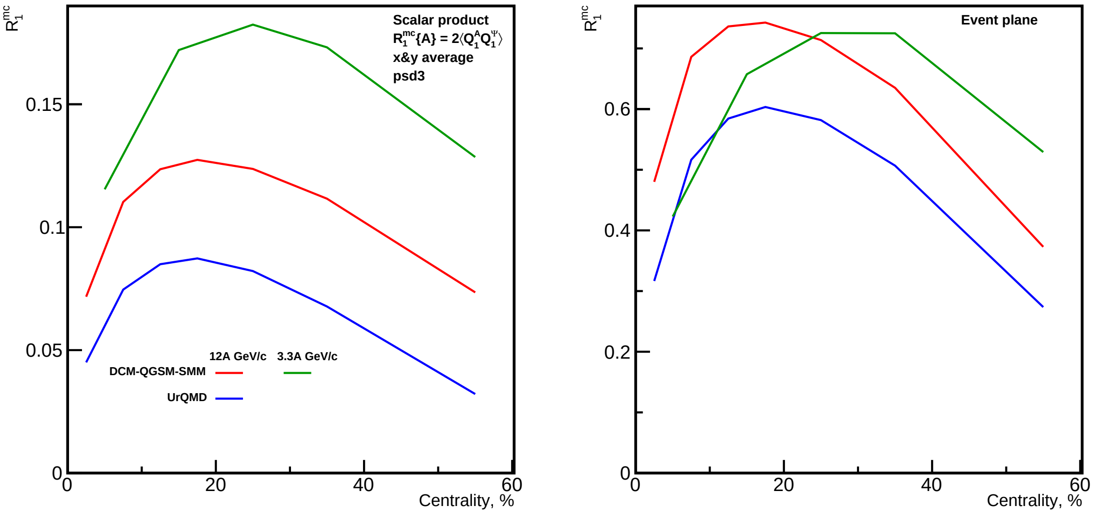

Figure 5.10: Centrality dependence of the MC-true resolution correction factor determined for 3-d PSD submodule: comparison of different beam momenta and event generators. Q_1-vector normalized by (**left**) sum of weights (scalar product method) and (**right**) magnitude (event plane method).

R_1 is a non-monotonic function with a maximum at mid-centrality. The resolution approaches zero in most central events because anisotropies disappear. It is decreasing towards peripheral events because the size of fireball pushing spectators apart becomes smaller.

R_1 at $12A\,\mathrm{GeV}/c$ shows higher values for DCM-QGSM-SMM simulations than for UrQMD (blue and red lines in Fig. 5.10, left). Besides different magnitudes of directed flow of separate nucleons in two models, the nucleon fragments are modelled only in DCM-QGSM-SMM. Smearing around reaction plane of azimuthal angle of individual nucleons is higher than of fragments, so directed flow of fragments is greater.

R_1 calculated for DCM-QGSM-SMM simulations shows higher values at lower momentum and vice versa (green and red lines in Fig. 5.10, left). For lower beam momentum the time of nuclei passing by each other is longer, therefore higher momentum is transferred from the fireball to spectators resulting in larger directed flow. At different beam momenta a certain module of the PSD registers spectators from different kinematical ranges, which in general have different directed flow.

In EP method R_1 calculated for DCM-QGSM-SMM at low and high beam momenta shows different behaviour in central and peripheral events, namely R_1 @3.3A GeV/c drops down in central events and becomes lower than @12A GeV/c (green and red lines in Fig. 5.10, right). In EP method R_1 depends on multiplicity of spectators (positively correlated), which becomes smaller in central events. UrQMD does not model spectators fragmentation and it is not considered in further resolution studies. Also only scalar product method, which has advantages over event plane method, see Sec. 4.2 and Sec. 5.2.1, paragraph "Fluctuations", is considered further.

Fig. 5.11 shows centrality dependence of resolution correction factor for different submodules of the PSD. Left panel represents averaged x- and y-components and right panel shows them separately.

R_1 changes non-monotonically from internal to external PSD submodules: $R_1\{PSD1\} < R_1\{PSD3\} < R_1\{PSD2\}$ (Fig. 5.11, left). A combination of two factors plays role here, one is spectators' flow which varies with kinematic, and another one is that a part of produced particles (mainly pions which have negative directed flow) gets into outer PSD submodule.

There is a splitting between x and y components of R_1, which has an opposite sign for inner and outer PSD modules (Fig. 5.11, right). A combination of several factors leads to such a non-trivial pattern. Magnetic field affects pions,

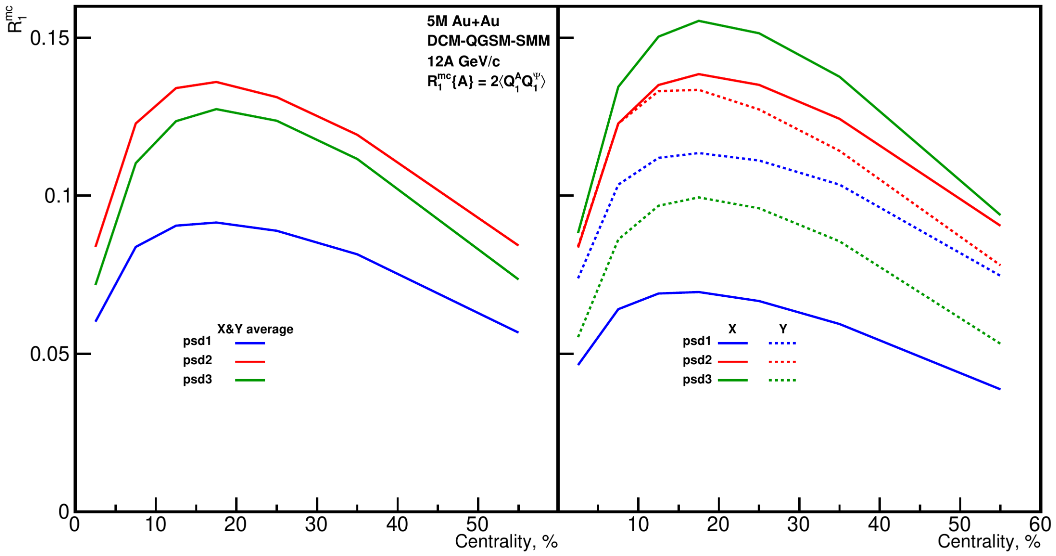

Figure 5.11: Centrality dependence of the MC-true resolution correction factor: comparison of different kinematic groups of spectators (subevents). R_1 (**left**) averaged $x-$ and y-components, (**right**) $x-$ and y-components separately. The input is generated with DCM-QGSM-SMM model at $12A\,\mathrm{GeV}/c$.

protons and fragments in x-direction with different relative strength (per unit of mass), while it does not affect neutrons. The outer PSD submodule has a non-symmetric shape (additional modules in horizontal direction, see Fig. 2.12, right), due to which fractions of particles getting into PSD3 differs for x and y. In the presented analysis, decoupling various contributions to the resolution of the PSD detector is complicated because it requires a matching between each spectator (and produced particle) and signal which it produces in the forward detector. In future studies with the FSD which will replace the PSD (for details see Sec. 2.2.2, paragraph “PSD”) resolution study will be more straightforward.

Resolution from 3-subevents method

Top panels of Fig. 5.12 show centrality dependence of $\mathbf{Q}_n$-vectors product which is used to test factorization according to Eq. 4.4. Bottom panels show centrality dependence of R_1 calculated with 3-subevents method compared to MC-true resolution.

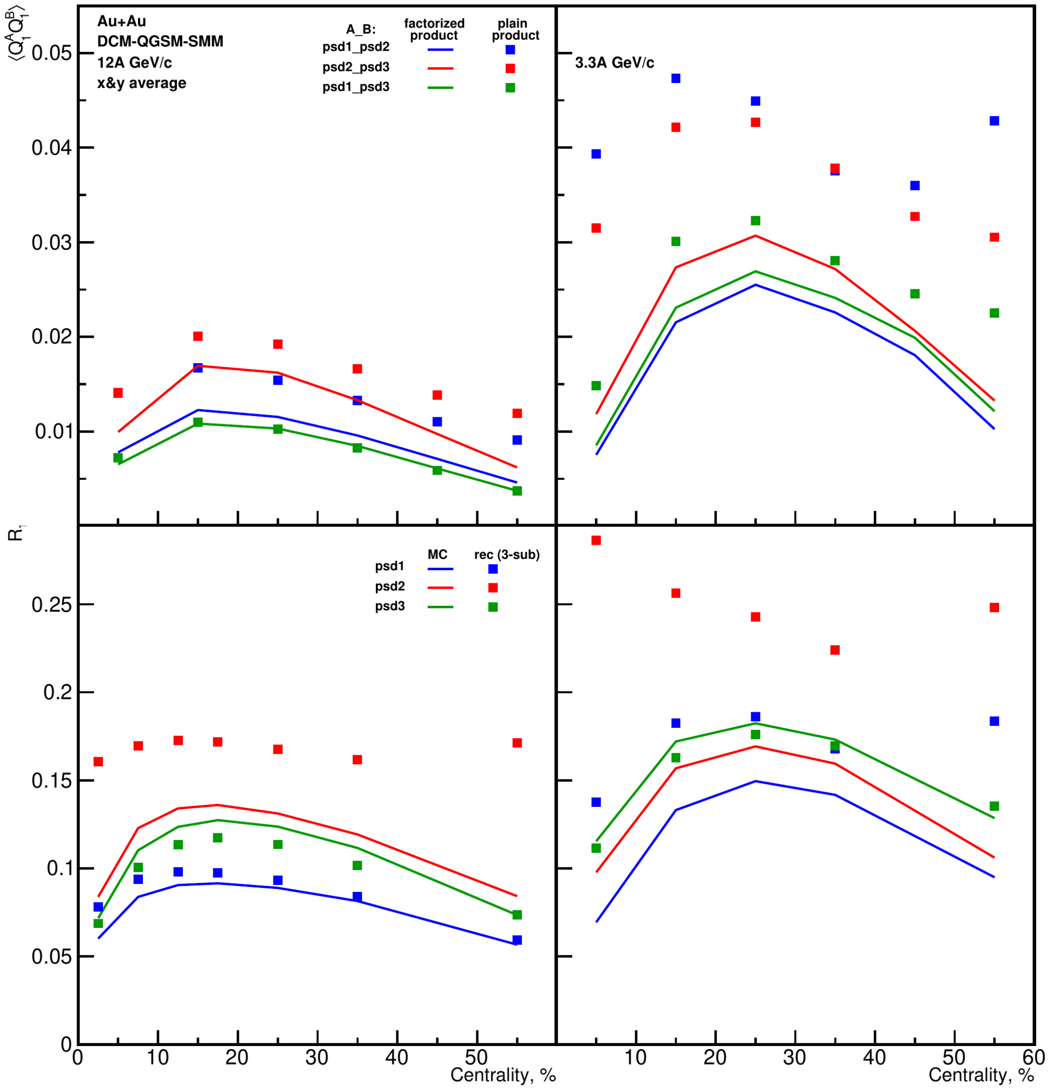

Figure 5.12: Centrality dependence of (**top**) Q_1-vectors product factorization (see Eq. 4.4: l.h.s. - markers, r.h.s. - lines), (**bottom**) resolution correction factor calculated with 3-subevent method (markers) compared to MC-true (lines). The input is generated with DCM-QGSM-SMM model at (**left**) $12A\,\mathrm{GeV}/c$ and (**right**) $3.3A\,\mathrm{GeV}/c$.

The $\langle \mathbf{QQ} \rangle$ is not factorized for pairs of neighbouring subevents PDS1-PSD2 and PSD2-PSD3 (Fig. 5.12, top panels, blue and red). Hadron showers originating in one module spread in transverse direction and therefore contribute into signal registered in the neighbouring module, see Sec. 5.2.2.

The $\langle \mathbf{QQ} \rangle$ factorization holds for non-neighbour subevents (PSD1-PSD3) in case of $12A$ GeV/c beam momentum and is not fulfilled for $3.3A$ GeV/c (Fig. 5.12, top panels, green). At lower beam momentum hadrons can scatter at higher angles, that is why transverse spread of showers becomes more significant and therefore leads to additional correlation between PSD1 and PSD3.

The $R_1\{PSD2\}$ is significantly overestimating the MC-true for both high and low beam momenta (Fig. 5.12, bottom panels, blue and green). In case of the PSD, Eq. 4.5 has both neighbouring pairs of subevents in numerator, and since $\langle \mathbf{QQ} \rangle$ is overestimated, R_1 is also biased.

For subevents except of PSD2 reconstructed R_1 does not reproduce MC-input, but is much closer to it than for PSD2 (Fig. 5.12, bottom panels, red). In Eq. 4.5 applied to PSD1 and PSD3 neighbouring pairs of subevents are located in numerator and denominator, and therefore biases of $\langle \mathbf{QQ} \rangle$ partially compensate each other.

Resolution from 4-subevents method

In order to avoid spurious correlation between $\mathbf{Q}_n$-vectors it is necessary to exclude pairs of neighbouring subevents (PSD1-PSD2 and PSD2-PSD3) from resolution determination. For this purpose one more subevent consisting of particles kinamatically separated from PSD-1,2,3 is introduced. Positively charged pions are used for 4-th subevent. π^+s are selected in the region of high enough absolute value of directed flow (see Fig. 5.13, left) and yield which minimizes statistical fluctuations in resolution determination and allows to avoid overlap with PSD acceptance which prevents from auto-correlation (see Fig. 5.13, right). Selection of π^+ is summarized in Tab. 5.2.

Left panel of Fig. 5.14 shows centrality dependence of $\mathbf{Q}_n$-vectors product which tests factorization according to Eq. 4.4. Right panel shows centrality dependence of R_1 calculated with 4-subevents method in comparison with MC-true resolution.

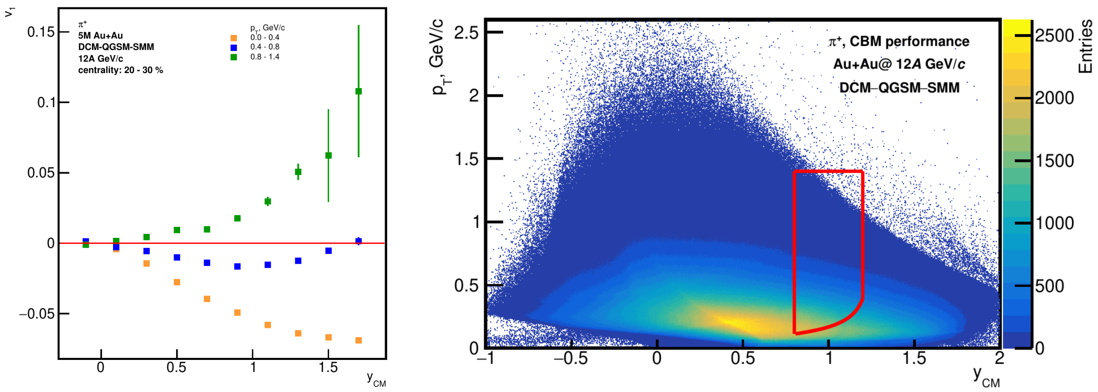

Figure 5.13: π^+ selection for 4-th subevent. (**left**) $v_1(y)$ for 20−30% central events in different p_T ranges; (**right**) population of reconstructed π^+ as a function of $p_T - y$, red frame shows kinematic selection of pions for 4-th subevent. The input is generated with DCM-QGSM-SMM at $12A$ GeV/c.

Setup	$\boldsymbol{p_T}$**, GeV/**$\boldsymbol{c}$	$\boldsymbol{y_{CM}}$	$\boldsymbol{\eta}$
u-12	$0 - 1$	$0.4 - 1.2$	< 2.88
d-12	$0 - 1.4$	$0.8 - 1.2$	
d-3	$0 - 0.4$	$0.4 - 1.6$	

Table 5.2: Kinematic selection of reconstructed π^+ used for 4-th subevent building in different setups.

Individual correlations $\langle \mathbf{QQ} \rangle$ are not factorized for PSD subevents and subevent built from pions. Discrepancy between l.h.s. and r.h.s. of Eq. 4.4 is more significant for outer PSD submodules than for inner ones (Fig. 5.14, left). An additional correlation between subevents is introduced by non-flow effects, in particular momentum conservation (see Sec. 5.2.1) and partial overlap of pions with PSD3 acceptance (see Sec. 5.2.2).

Reconstructed R_1 generally agrees with the MC-input (Fig. 5.14, right) despite of deviations from factorization. Discrepancies in factorization do not affect the resolution correction factor since non-flow effects largely cancel each other because they contribute both to numerator and denominator of Eq. 4.6.

Overall, the 4-subevents method of resolution determination has much better

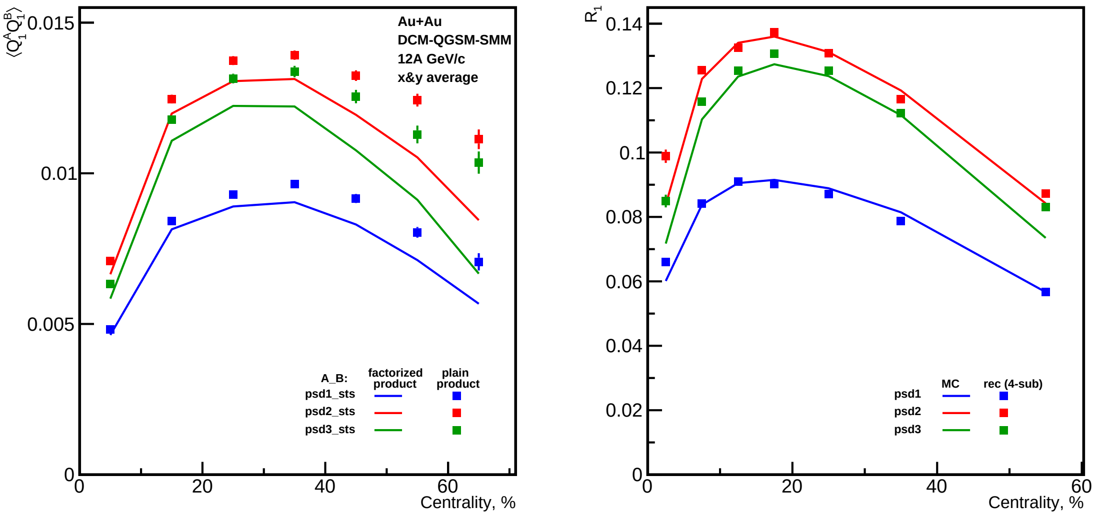

Figure 5.14: Centrality dependence of (**left**) Q_1-vectors product factorization (see Eq. 4.4: l.h.s. - markers, r.h.s. - lines), (**right**) resolution correction factor calculated with 4-subevent method (markers) compared to MC-true (lines). The input is generated with DCM-QGSM-SMM model at $12A\,\mathrm{GeV}/c$. In left panel graphs are multiplied by -1 to move them from negative side of the plot to positive (since directed flow of pions used for building of 4-th subevent is negative).

precision than 3-subevents method, and it is used to obtain flow results in this thesis. Compilation of the results for resolution correction factor is present in the App. C.

5.3.2 p_T, y and centrality dependence

Let us consider the mechanism of the anisotropic flow (in particular directed flow) development during the evolution of the collision. The collision has several stages (see Sec. 1.4), which all contribute to the anisotropic flow. When the colliding nuclei start to interact, dense matter in the nuclei overlap deflects the spectator nuclear matter. The deflection of the remnants of the incoming nucleus at positive rapidity is in the direction along impact parameter vector and vice versa. Also this mechanism applies to particles produced mainly from nucleons undergone an inelastic process and thus inherit nucleons dynamics - e.g. Λ-baryons.

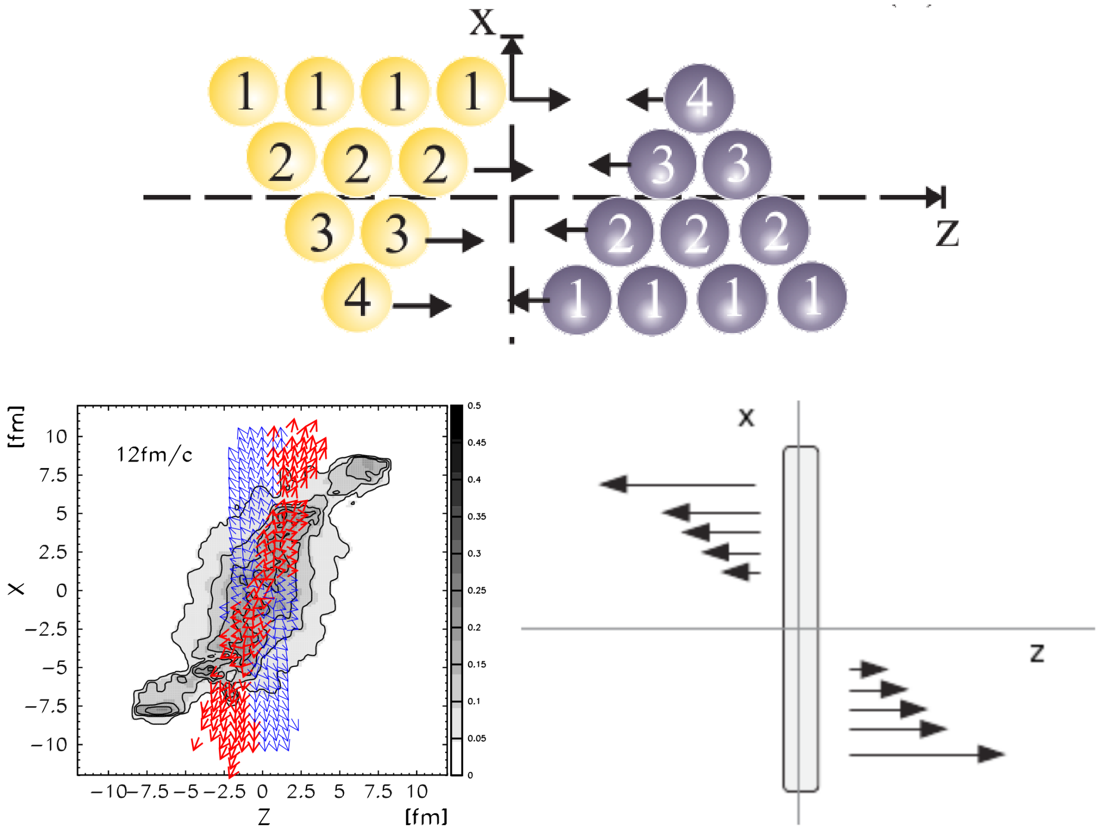

Figure 5.15: (**top**) A schematic sketch of a midcentral HIC. The overlap region is magnified and spectators are not shown [150]. (**bottom left**) Net-baryon density (grey filling) at $t = 12\ fm/c$ in the reaction plane with velocity arrows for midrapidity ($|y| < 0.5$) fluid elements: antiflow - blue arrows, normal flow - red arrows [151]. (**bottom right**) Initial longitudinal velocity profile in non-central nuclear collisions [152]. In all panels the beam axis is z and an impact parameter vector lies along x.

The distribution of the matter created in HIC (grey filling in Fig. 5.15, bottom left) has strong density gradients. Mesons produced in this medium ($\pi^{\pm}, K^{\pm}$ and relevant to the current thesis - K_S^0) with rapidity $y > 0$ and momenta along the direction of impact parameter vector ($+x$ in Fig. 5.15, bottom left) have higher probability to escape than those escaping in $-x$ direction. This is because the latter experience more scattering and their momentum is distributed among other particles. It leads to the dependence of directed flow on transverse momentum:

mesons with high p_T have positive v_1 while mesons with low p_T form so-called *antiflow* ($v_1 < 0$), see red and blue arrows in Fig. 5.15, bottom left. Another consequence of the density gradient along impact parameter is the presence of the longitudinal velocity gradient (see Fig. 5.15, bottom right), which leads to the directed flow of produced particles according to hydrodynamics calculations [152]. Angular momentum (see Eq. 1.2), and rotation of the fireball can also contribute to the directed flow [153].

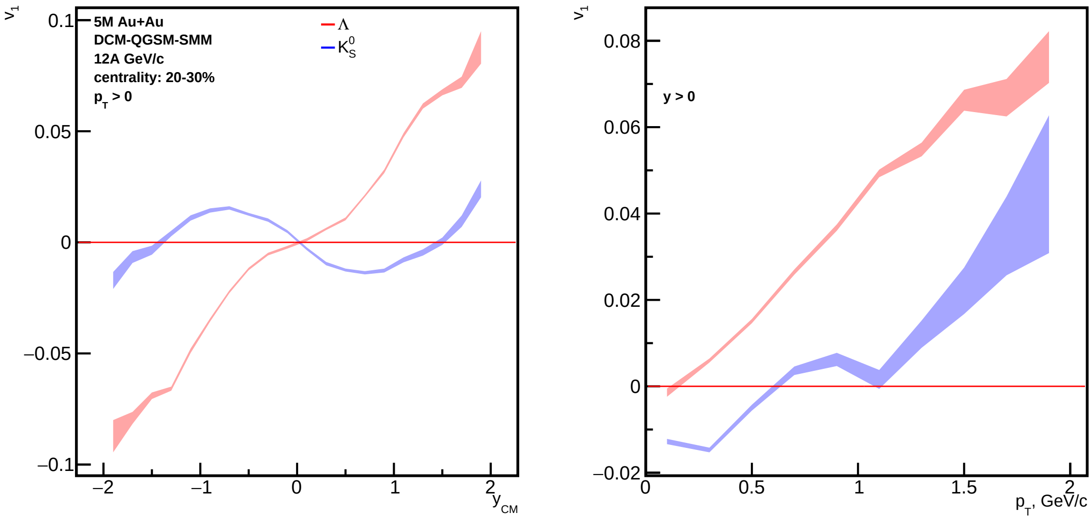

Figure 5.16: Directed flow of Λ-baryons and K^0_S-mesons dependence on (**left**) rapidity and (**right**) transverse momentum. The input is generated with DCM-QGSM-SMM at $12A\,\mathrm{GeV}/c$, $20-30\%$ central events are selected.

Fig. 5.16, left, shows directed flow dependence on rapidity simulated by DCM-QGSM-SMM model at $p_{\mathrm{beam}} = 12A\,\mathrm{GeV}/c$ for Λ-baryons and K^0_S-mesons (cf. Fig. 1.14). One can see a positive $v_1\{\Lambda\}$, in first approximation linear with y because Λs are mostly formed by nucleons from colliding nuclei, which experienced inelastic collision. The $v_1\{K^0_S\}$ has a wiggle dependence on rapidity, with the negative slope at midrapidity and positive at forward rapidity. This is driven by the interplay of scattering of produced mesons in the medium with non-uniform density (see Fig. 5.15, bottom left) and, when the K^0_S-meson is produced close to spectators, inheritance of their kinematics. Fig. 5.16, right, shows directed flow dependence on transverse momentum. The v_1 grows monotonically with p_T, starting from ≈ 0 in case of Λ-baryons and starting from negative v_1 and crossing zero in case of K_S^0-mesons. Similar to the trends observed in v_1 as a function of rapidity, this reflects the dynamics of produced and spectator hadrons resulting in their tendency to escape in a certain direction.

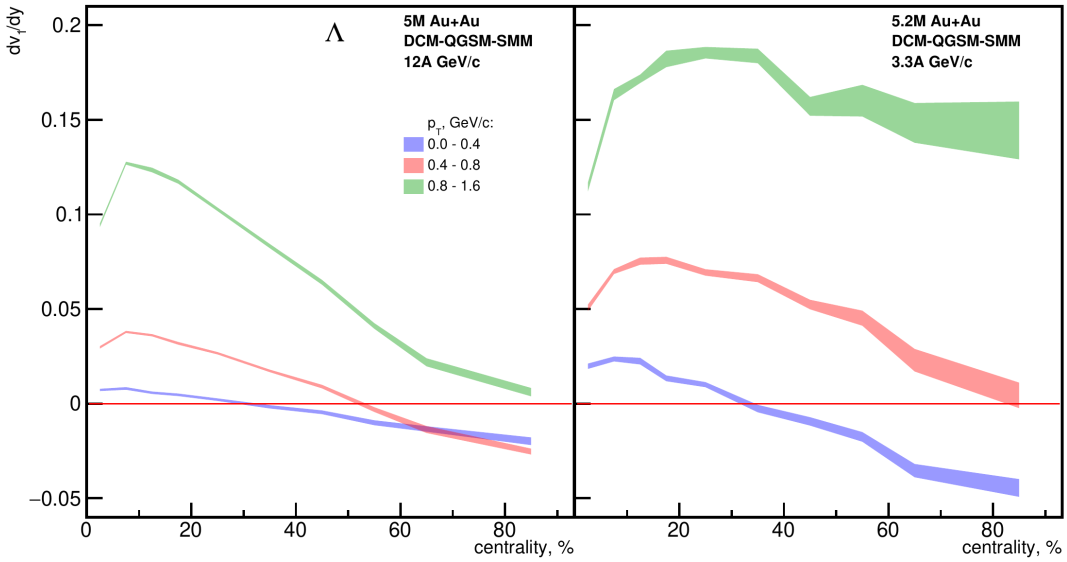

Figure 5.17: Centrality dependence of the directed flow slope dv_1/dy of Λ-baryons. The input is generated with DCM-QGSM-SMM model at (**left**) $12A$ GeV$/c$ and (**right**) $3.3A$ GeV$/c$.

Fig. 5.17 shows the directed flow slope dv_1/dy dependence on centrality for the highest and the lowest SIS-100 beam momenta (left and right panels respectively). The dv_1/dy vanishes in central events due to absence of any anisotropy, grows in magnitude with increasing centrality, and drops again and becomes negative in peripheral collisions. This is because of decreasing size of the fireball and shadowing by spectators. The dv_1/dy at beam momentum $3.3A$ GeV$/c$ is stronger than at $12A$ GeV$/c$ by a factor of 2. This can be explained by longer passing time of two nuclei, during which a directed flow is formed.

CBM performance for v_1 vs $p_T - y$

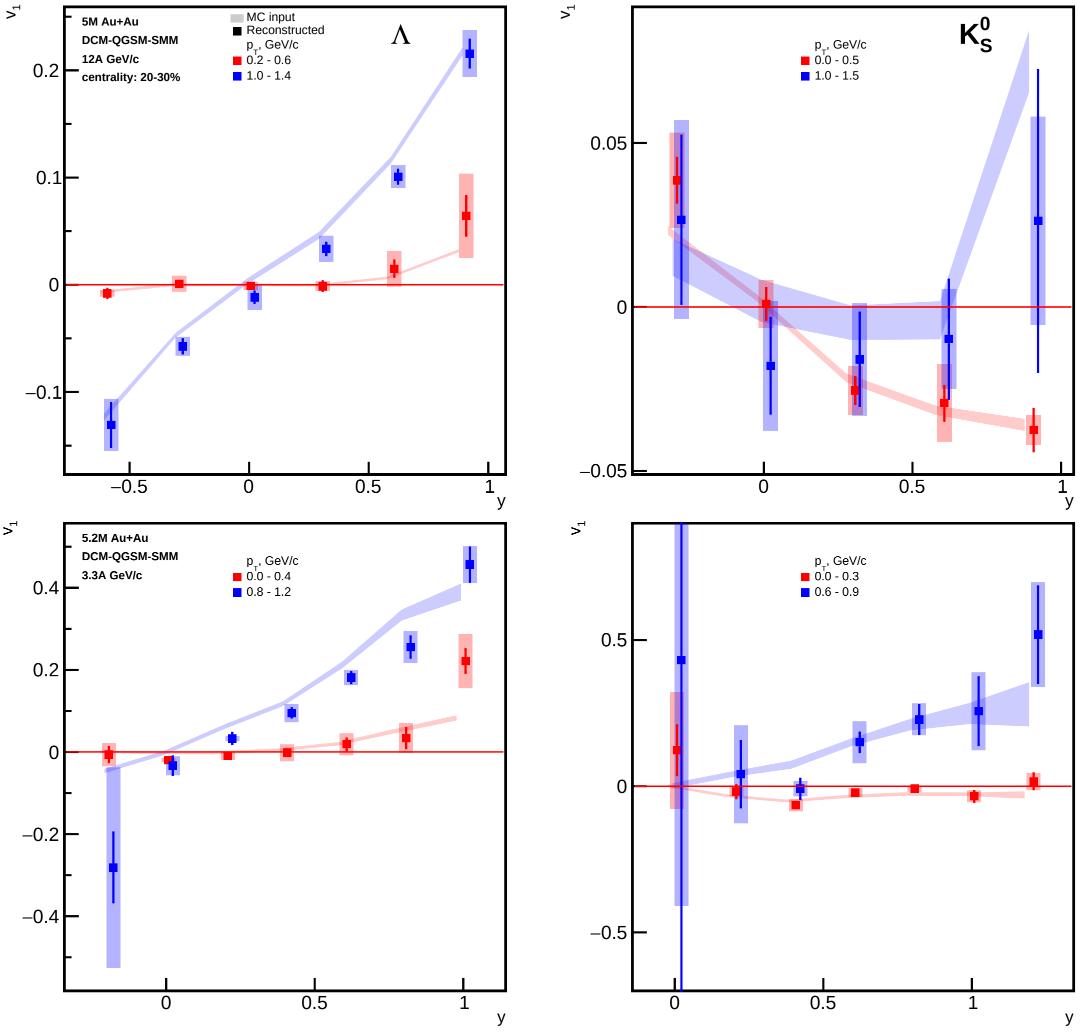

Figure 5.18: Rapidity dependence of the directed flow $v_1(y)$ of (**left**) Λ-hyperons and (**right**) K^0_S-mesons with low (red) and high (blue) transverse momentum. Flow is calculated relative to spectators registered in PSD with resolution determined via 4-subevents method. The input is generated with DCM-QGSM-SMM at (**top**) $12A\,\mathrm{GeV}/c$ and (**bottom**) $3.3A\,\mathrm{GeV}/c$.

Selection of decay candidates for directed flow calculations is specified in Tab. 3.1. Event plane is estimated with spectators registered in the PSD and resolution correction factor is determined via 4-subevents method using π^+ for 4-th subevent. A set of 6 measurements of v_1 is obtained: 2 components of v_1 (v_{1x} and v_{1y}) are calculated relative to spectators in 3 subevents (PSD1, PSD2 and PSD3). v_1 is calculated as a mean value of this set, and systematic uncertainty is estimated as a standard deviation of the set. Fig. 5.18 illustrates the directed flow of Λ and K^0_S as a function of rapidity $v_1(y)$ for 20-30% central events at low and high transverse momenta. The v_1 dependence on transverse momentum is shown in Fig. 5.19. Results at $p_{\text{beam}} = 12A\,\text{GeV}/c$ and $3.3A\,\text{GeV}/c$ are compared. Filled areas represent MC-true input with its statistical uncertainty, full squares - flow reconstructed in data-driven approach using methods described in Sec. 4.1-4.4. Error bars visualize statistical uncertainties, and filled semi-opaque rectangles represent systematic uncertainties.

Reconstructed v_1 mainly reproduces the MC input within statistical errors what shows that CBM is well suited for strange hadrons directed flow measurements. Reconstructed v_1 compared to the simulated input shifts down for all rapidities with maximal shift localized at high transverse momenta (blue points in Fig. 5.18, points in Fig. 5.19 at the right part of the plot). For details see discussion in Sec. 5.2.1. Reconstructed v_1 of Λ-baryons at forward rapidity and low transverse momentum is systematically above input values (red point at the right edge in Fig. 5.18, bottom left). For discussion of this bias see Sec. 5.2.2. Directed flow measurements at $p_{\text{beam}} = 3.3A\,\text{GeV}/c$ are challenging in backward- and mid-rapidity region. Kaons' v_1 has large statistical and systematic uncertainties at $y \approx 0$ (blue point at the left edge in Fig. 5.18, bottom right). It is because the CBM limits decays reconstruction in backward rapidity at low beam momenta, for details see Sec. 5.1.

Fig. 5.20 illustrates the directed flow of Λ-baryons and K^0_S-mesons predicted by DCM-QGSM-SMM model and reconstructed with the CBM. Also the performance of the CBM experiment is compared with that of STAR-FXT [56].

The CBM experiment has larger acceptance than the STAR-FXT. CBM covers partially backward rapidity what allows to reduce systematic uncertainties (see Sec. 5.2.1 for details). The CBM will be able to perform $v_1(y)$ measurements with

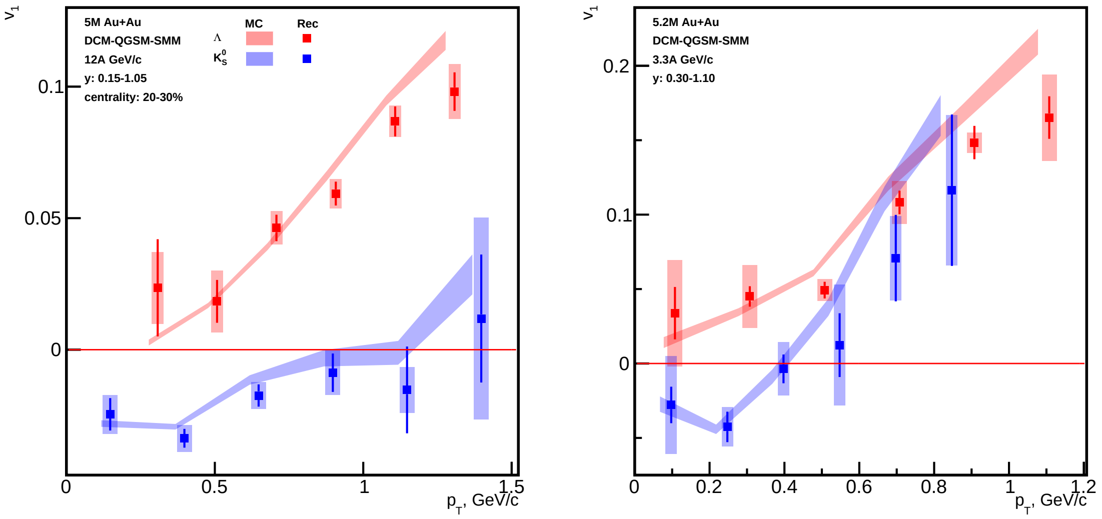

Figure 5.19: Transverse momentum dependence of the directed flow $v_1(p_T)$ of Λ-hyperons (red) and K^0_S-mesons (blue) integrated in the forward rapidity region. Flow is calculated relative to spectators registered in PSD with resolution determined via 4-subevents method. The input is generated with DCM-QGSM-SMM at (**left**) $12A\,\mathrm{GeV}/c$ and (**right**) $3.3A\,\mathrm{GeV}/c$.

higher precision when compared to the same number of collisions. The CBM has better reconstruction efficiency of Λ and K^0_S (of tens percents compared to a few percents at the STAR) and covers low-p_T, where a large fraction of particles is produced [154]. More details of the $p_T - y$ dependence of v_1 is present in App. C.

CBM performance for dv_1/dy slope and $v_1|_{y=0}$ offset vs centrality

Fig. 5.21 illustrates the directed flow slope (top panels) and offset (bottom panels) of Λ as a function of centrality for various transverse momenta. DCM-QGSM-SMM simulations at $p_{\mathrm{beam}} = 12A\,\mathrm{GeV}/c$ (left panels) and $p_{\mathrm{beam}} = 3.3A\,\mathrm{GeV}/c$ (right panels) are compared.

Overall, the reconstructed values of the slope of directed flow reproduce MC input within statistical errors. In some cases there are deviations due to limitations of the current corrections for efficiency of the decays reconstruction (Sec. 5.2.3) and breaking of factorization in resolution determination (Sec. 5.2.1 and 5.2.2).

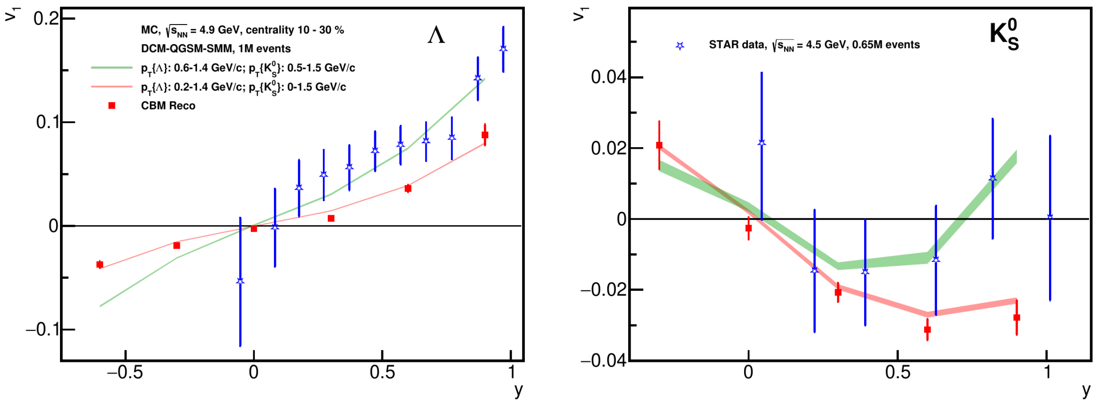

Figure 5.20: Directed flow as a function of rapidity for (**left**) Λ and (**right**) K^0_S: comparison of performance of the CBM and the STAR [56]. Tougher p_T-cut is used to mimic STAR's acceptance, and relaxed p_T-cut shows CBM's performance.

Statistically significant intercept given by non-zero directed flow at midrapidity is present in majority of kinematic and centrality regions. It is largest for high p_T particles and peripheral events, which indicates contribution due to momentum conservation. More details about centrality dependence of directed flow slope and offset, including K^0_S-mesons and calculations for the UrQMD model is present in App. C.

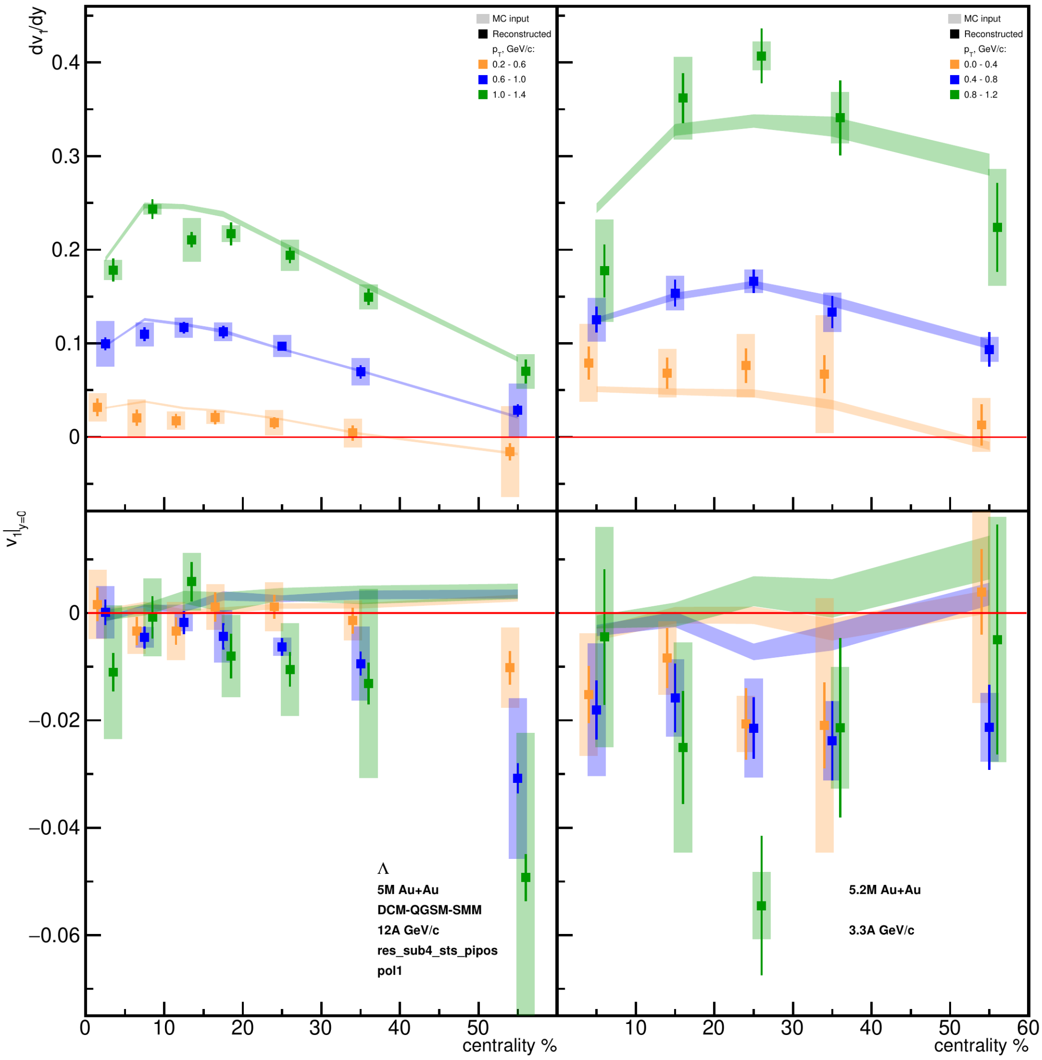

Figure 5.21: Centrality dependence of Λ-baryon's directed flow (**top**) slope dv_1/dy and (**bottom**) offset $v_1|_{y=0}$. The input is generated with DCM-QGSM-SMM model at (**left**) $12A\,\mathrm{GeV}/c$ and (**right**) $3.3A\,\mathrm{GeV}/c$.

5.3.3 Systematic uncertainties summary

Tab. 5.3 summarizes sources of systematic uncertainties in directed flow measurement and characteristic values for different beam momenta, particles species and kinematics, and event centrality. Systematic uncertainties are calculated as a difference between MC-true and reconstructed values of v_1 (R_1). When quantifying a given source of systematic uncertainty, all other effects were eliminated by using MC-true information.

Source	**p_{beam}, A GeV/c**	**Centrality, %**	**p_T, GeV/c**	**Value**
Hadronic showers & momentum conservation (resolution calculation)	12	10-40	n.a.	≈0%
		0-10, 40-70		7%
	3.3	10-40		10%
		0-10, 40-70		40%
Auto-correlation[1]	12	0-10	$\lesssim 0.8$	120%
		10-40		80%
	3.3	0-10		70%
		10-40		30%
Momentum conservation, non-flow[2]	3.3, 12	0-40	$\gtrsim 0.4$	≈ -0.01
		40-70		≈ -0.04
Non-uniformities of acceptance	3.3, 12	All	$\gtrsim 0.4$	$\lesssim 5\%$
			$\lesssim 0.4$	$\approx 30\%$
Parametrizations in invariant mass fit	All			$\lesssim 1\%$

[1] This effect is relevant only for v_1 of Λ-baryons with rapidity $y \approx 1$ calculated with the PSD2 and PSD3 subevents. In peripheral events the v_1 of Λs is small and the autocorrelation effect is dominant, therefore they are not shown in the table.

[2] Systematic uncertainties due to momentum conservation and non-flow are given as a value of $v_1|_{y=0}$ offset, since expected value of v_1 at midrapidity is 0, and relative error is not defined.

Table 5.3: Characteristic values of systematic uncertainties in flow extraction.

5.4 Statistical uncertainties projections for Λ, $\bar{\Lambda}$, Ξ^- dv_1/dy and hyperon global polarization

The CBM is designed to perform measurements at extremely high interaction rate, so the collected statistics during the first run is expected to reach $2 \cdot 10^{10}$ events. On the other hand, production of multi-strange hyperons is rare. This subsection presents the statistical uncertainties projections for (multi-)strange hadrons directed flow and polarization measurements at CBM.

The directed flow slope dv_1/dy projections are obtained following the steps:

1. The dv_1/dy and its statistical uncertainty are calculated with existing MC simulations for Λ- and Ξ^--baryons at the highest SIS-100 beam momentum ($12A\,\mathrm{GeV}/c$) and only for Λ-baryon for the lowest beam momentum ($3.3A\,\mathrm{GeV}/c$);
2. The dv_1/dy of $\bar{\Lambda}$-baryon is assumed to be the same as for Λ;
3. The dv_1/dy of Ξ^--baryon at $3.3A\,\mathrm{GeV}/c$ is calculated assuming that the ratio to Λ's dv_1/dy is the same as at $12A\,\mathrm{GeV}/c$.
4. Yields of $\bar{\Lambda}$-baryon at both beam momenta and of Ξ^--baryon at $3.3A\,\mathrm{GeV}/c$ are predicted by thermal model [155];
5. Statistical uncertainties of dv_1/dy are assumed to be inversely proportional to the square root of number of particles.

Magnitudes of dv_1/dy calculated in items 2 and 3 are are used to visualize the projected uncertainties.

Projections for the global polarization P_H are calculated in the following way:

1. Magnitudes of P_H are given by extrapolation of existing data for FAIR energies and particles species according to theoretical calculations, for details see Tab. 5.4;

2. Since global polarization is very similar to the directed flow from the formulaic point of view (cf. Eq. 1.5 and 4.15) accurate to a constant factor and replacing cosine with sine, the statistical uncertainty of P_H is assumed to be the same as of v_1.

The assumptions listed above for directed flow slope and global polarization are summarized in Tab. 5.4.

Fig. 5.22 represents CBM projections for measurements of dv_1/dy (left) and P_H (right) together with the world data. World data are shown in empty markers, error bars denote statistical uncertainties, while semi-opaque rectangles represent systematic uncertainties. CBM projections for directed flow slope and global polarization are visualized with full markers. Statistical uncertainties are shown for 20 billion events unless denoted otherwise.

Following conclusions about CBM performance are made:

- dv_1/dy of (anti-)Λ- and Ξ^--baryons at $12A\,\mathrm{GeV}/c$ can be measured with extremely low statistical uncertainties;
- dv_1/dy of Λ- and Ξ^- baryons at $3.3A\,\mathrm{GeV}/c$ can be measured with statistical uncertainties less than 10%;
- Measurement of dv_1/dy of $\bar{\Lambda}$-baryons at $3.3A\,\mathrm{GeV}/c$ will require 10^{12} events;
- P_H of (anti-)Λ- and Ξ^--baryons at $12A\,\mathrm{GeV}/c$ can be measured with statistical uncertainty less than 10% (Λ - with negligible uncertainty);
- P_H of Λ-baryons at $3.3A\,\mathrm{GeV}/c$ can be measured with extremely small statistical uncertainty;
- Measurement of P_H of Ξ^-- and $\bar{\Lambda}$-baryons at $3.3A\,\mathrm{GeV}/c$ will require 10^{13} and $2 \cdot 10^{13}$ events respectively.

$\sqrt{s_{NN}}$, GeV	**Particle**	**Assumptions**	
		Magnitude	**Stat. uncertainty**
dv_1/dy			
2.86	$\boldsymbol{\Lambda}$	DCM-QGSM-SMM model, CBM Geant4 simulation	DCM-QGSM-SMM model, CBM Geant4 simulation, $\sigma_{stat} \sim 1/\sqrt{N}$
	$\boldsymbol{\bar{\Lambda}}$	The same as Λ	Yields predicted by [155], $\sigma_{stat} \sim 1/\sqrt{N}$
	$\boldsymbol{\Xi^-}$	Ratio to Λ the same as @4.93 GeV	
4.93	$\boldsymbol{\Lambda}$	DCM-QGSM-SMM model, CBM Geant4 simulation	DCM-QGSM-SMM model, CBM Geant4 simulation, $\sigma_{stat} \sim 1/\sqrt{N}$
	$\boldsymbol{\bar{\Lambda}}$	The same as Λ	Yields predicted by [155], $\sigma_{stat} \sim 1/\sqrt{N}$
	$\boldsymbol{\Xi^-}$	DCM-QGSM-SMM model, CBM Geant4 simulation	DCM-QGSM-SMM model, CBM Geant4 simulation, $\sigma_{stat} \sim 1/\sqrt{N}$
P_H			
2.86, 4.93	$\boldsymbol{\Lambda}$	Interpolation of HADES and STAR data	$\sigma_{stat}\{\langle\cos\varphi\rangle\} =$ $\sigma_{stat}\{\langle\sin\varphi\rangle\}$, Yields predicted by [155], $\sigma_{stat} \sim 1/\sqrt{N}$
	$\boldsymbol{\bar{\Lambda}}$	Ratio to Λ the same as in (11.5-39)GeV measured by STAR [54]	
	$\boldsymbol{\Xi^-}$	Ratio to Λ predicted by [156]	

Table 5.4: Assumptions made in statistical uncertainties projections for dv_1/dy and hyperon global polarization.

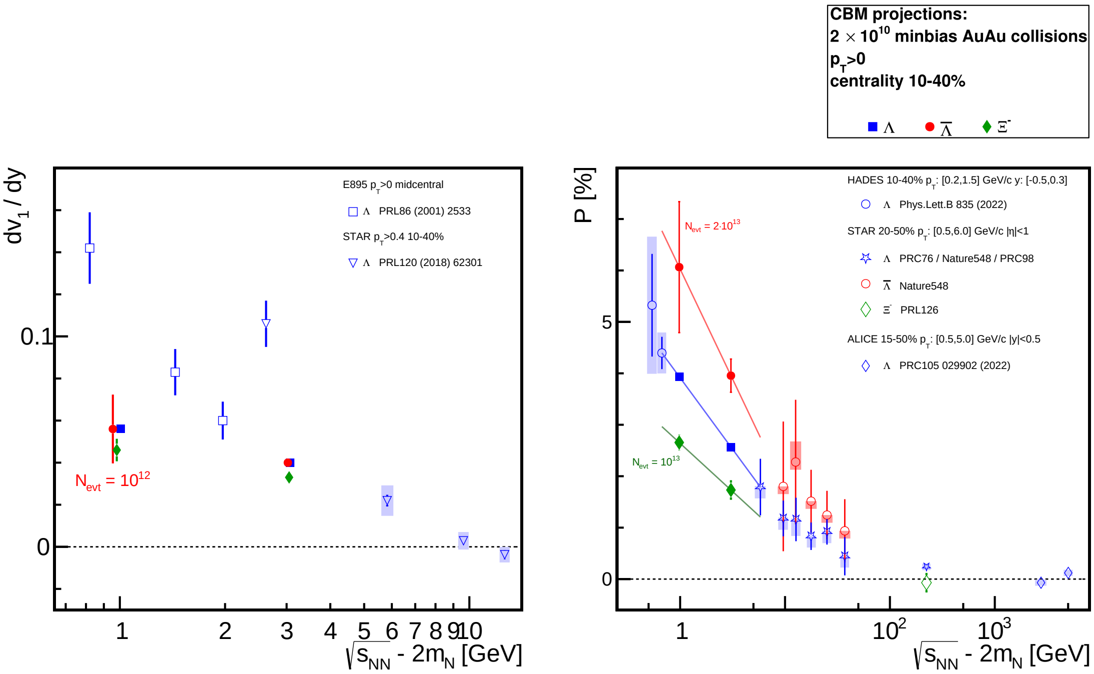

Figure 5.22: (**left**) Directed flow slope dv_1/dy and (**right**) global polarization coefficient of (multi)strange hadrons as a function of collision energy minus two nucleon masses - world data and expected CBM performance (the outside legend is common for both plots).

Chapter 6

Summary and conclusions

The strong force is one of the four fundamental interactions, and the theory of it is called Quantum Chromodynamics (QCD). Extraction of the properties of the QCD matter, such as compressibility, viscosity and various susceptibilities, and its Equation of State (EoS) is an important aspect of the QCD matter study. The region of the QCD phase diagram, where matter is compressed to densities of a few times normal nuclear density is characterized with baryonic chemical potential μ_B of several hundreds MeV. Search for a possible phase transition and a critical point in this region of the QCD phase diagram is one of the main goals of the near future explorations.

In the laboratory a scan of the QCD phase diagram can be performed via heavy-ion collisions. The QCD matter created in the overlap region of colliding nuclei (fireball) is rapidly expanding during the collision evolution. There are strong temperature and pressure gradients, extreme electromagnetic fields and an exchange of angular momentum and spin between the system constituents. These effects result in collective phenomena, such as an anisotropic flow and a global polarization of particles.

Anisotropic flow is quantified by the coefficients v_n from a Fourier decomposition of the azimuthal angle distribution of emitted particles. The directed flow characterized by the first harmonic coefficient v_1 can shed light on the properties of the QCD matter and its EoS. In particular, the change of the sign of v_1 in heavy-ion collisions at $\sqrt{s_{NN}}$ of several GeV is attributed to a softening of the EoS, and thus can be an evidence of the first order phase transition. The global polarization coefficient P_H probes the QCD matter vorticity and mechanism of orbital momentum transfer into the spin of produced particles. In collisions at $\sqrt{s_{NN}}$ of several GeV hadrons with strange quarks are produced near the threshold, what makes their yield and emission anisotropy sensitive to the density of the fireball.

The Compressed Baryonic Matter (CBM) experiment at the Facility of Antiproton and Ion Research (FAIR) will perform heavy-ion collisions at $\sqrt{s_{NN}} = 2.9 - 4.9\,\text{GeV}$. Multidifferential measurements of yields and especially of azimuthal modulations (flow) of rarely produced multi-strange hadrons will become available with CBM thanks to its operation at the peak interaction rate of 10^7 Hz. The current doctoral work presents the results for the CBM performance for measurements of anisotropic flow and global polarization of Λ, $\bar{\Lambda}$ and multistrange Ξ^- hyperons.

In the CBM short-lived particles are reconstructed via their decay products. PFSimple package, developed as a part of current doctoral work, allows to reconstruct two-body (Λ, K^0_S) and cascade (Ξ^-, Ω^-) decay candidates and optimize their selection criteria. Besides being used in the current work, it has been already applied in the CBM collaboration to perform other studies and was extended in [131, 132] for 3-body decays reconstruction, e.g. hypernuclei.

Using the Geant4 simulation of the CBM detector response, the CBM acceptance and reconstruction efficiency for Λ, K^0_S and Ξ^- as a function of transverse momentum and rapidity were obtained at the highest (4.9 GeV) and lowest (2.9 GeV) collision energies achievable with the SIS-100 accelerator. Using PFSimple, configured for selection of decay candidates with high signal-to-background ratio (5 for Λ, 2 for K^0_S, 15 for Ξ^-), it was demonstrated that the CBM acceptance covers both midrapidity and forward rapidity $y \in (0; 1)$ regions in transverse momentum range $p_T \in (0; 1.5)\,\mathrm{GeV}/c$. The acceptance coverage of backward rapidity region depends on the collision energy and is the largest at $\sqrt{s_{NN}} = 4.9\,\mathrm{GeV}$. Coverage of mid- and forward-rapidity is necessary for flow measurements, in particular for extraction of the slope dv_n/dy and offset v_n at $y = 0$. Coverage of the backward-rapidity region allows to reduce systematic uncertainties in directed flow measurement caused by correlations due to global momentum conservation, using the anti-symmetry of v_1 as a function of rapidity. Reconstruction efficiency reaches values up to 50% for Λ and K^0_S, and up to 20% for Ξ^- in the whole range of SIS-100 collision energy range. At $\sqrt{s_{NN}} = 4.9\,\mathrm{GeV}$ the maximum of reconstruction efficiency is located near midrapidity, while at $\sqrt{s_{NN}} = 2.9\,\mathrm{GeV}$ the maximum is shifted to forward rapidities ($y \approx 1$). At $\sqrt{s_{NN}} = 2.9\,\mathrm{GeV}$ the reconstruction efficiency at midrapidity and backward rapidity is low ($\lesssim 10\%$), especially for $p_T > 0.5\,\mathrm{GeV}/c$.

In order to measure anisotropic flow coefficients one needs to estimate the reaction plane of the collision, which is spanned by beam axis and impact parameter vector. It is done using nucleons not participating in the collision (spectators), registered with the Projectile Spectator Detector (PSD), which is a hadronic calorimeter. Imperfections in the reaction plane estimation are taken into account by the resolution correction factor R_1, evaluated using three- and four-subevents methods. Produced particles and their decay products entering the acceptance of the PSD bias the measured value of flow. Spread of hadronic shower in the calorimeter in transverse to the beam direction results in spurious correlations between particles used in the subevents methods. Azimuthal non-uniformity of the reconstruction efficiency and effects of magnetic field are corrected for using the procedure described in [133]. Magnitudes of corrections for azimuthal non-uniformity in decays reconstruction are of the order of a few percents. The corrections for the PSD non-uniformities are of the order of several percents in the direction perpendicular to the CBM magnetic field and one order of magnitude less for the direction along it. Combinatorial background contribution to flow is subtracted with invariant mass fit method, which is implemented within current doctoral work as the QnDiscriminator extension to the QnTools software package.

Anisotropic flow coefficients are calculated by correlating azimuthal angles of particles whose flow is measured and particles used for reaction plane estimation, which are reconstructed in different kinematic regions. Azimuthal correlations can originate not only due to common anisotropy with respect to the reaction plane but also due to other physics phenomena and detector effects such as:

- Short-range correlations and resonance decays (non-flow);
- Global transverse momentum conservation;
- Event-by-event fluctuations in nucleons positions (flow fluctuations);
- Auto-correlations imposed by the same particle (or particle and its decay product) traversing acceptance of multiple CBM subsystems;
- Transverse spread of hadronic showers across multiple modules of the PSD calorimeter.

Estimating magnitude of these correlations is important for proper evaluation of systematic uncertainties in flow measurement.

The 3-subevents method for resolution correction factor R_1 calculation suffers from spurious correlation due to transverse spread of hadronic showers in the PSD calorimeter which results in the discrepancy of R_1 from the MC-true value. In the case of 4-subevents method where positively charged pions used to form the 4-th subevent, the calculated values of R_1 reproduce the MC-true values at $\sqrt{s_{NN}} = 4.9\,\mathrm{GeV}$. Due to much broader spread of the hadronic showers at $\sqrt{s_{NN}} = 2.9\,\mathrm{GeV}$ there is a remaining bias in R_1 evaluation of 10% in mid-central events and up to 40% in central and peripheral events.

Reconstructed v_1 with 4-subevent method reproduces the MC values within statistical errors in $-0.5 < y < 0.7$ rapidity range at $\sqrt{s_{NN}} = 4.9\,\mathrm{GeV}$, while at $\sqrt{s_{NN}} = 2.9\,\mathrm{GeV}$ the v_1 is biased by discrepancies in R_1 reconstruction. At high transverse momenta discrepancies originate due to non-flow correlation and global momentum conservation. The v_1 at forward rapidity and low transverse momentum is overestimated for Λ-baryons due to decay proton getting into the PSD acceptance. The CBM experiment has larger acceptance than STAR fixed target setup - in the backward rapidity region and for low transverse momenta ($p_T \lesssim 0.5\,\mathrm{GeV}/c$). Statistical uncertainties of $v_1(y)$ at CBM are expected to be much lower than at STAR for equivalent number of heavy-ion collisions due to higher reconstruction efficiency and wider acceptance in p_T.

In $10-40\%$ central events reconstructed values of the directed flow slope reproduce the MC values within statistical errors. In other centrality regions the contributor to discrepancy is a spurious correlation between subevents in resolution correction factor determination. Momentum conservation results in a non-zero intercept of v_1 at midrapidity, which is larger for high p_T and peripheral events.

Statistical uncertainties of (multi-)strange hadrons directed flow slope dv_1/dy and polarization P_H measurements are estimated for the expected first CBM data taking period ($2 \cdot 10^{10}$ events) both for the lowest and the highest SIS-100 collision energies. The measurement of dv_1/dy of $\bar{\Lambda}$ at $\sqrt{s_{NN}} = 2.9\,\mathrm{GeV}$ requires 10^{12} collisions; P_H of $\bar{\Lambda}$ and Ξ^- at $3.3A\,\mathrm{GeV}/c$ require $2 \cdot 10^{13}$ and 10^{13} events respectively. The relative error will be of order of 25% that will allow CBM to perform an energy scan of dv_1/dy and P_H of (multi-)strange hadrons, and provide an experimental data to discriminate between models implementing EoS with and without first order phase transition. The measurements of the particle-antiparticle difference of flow and polarization will be possible, which are needed to quantify the magnitude and evolution of the magnetic field in a heavy-ion collision.

A first study of the CBM performance for (multi-)strange hadrons flow and polarization measurements presented in this thesis can be further extended in several directions. Firstly, a study of systematic effects in multi-differential flow evaluation with high-statistics Monte-Carlo simulations will help to understand their nature and how to reduce them. Secondly, study of the CBM performance with the Forward Spectator Detector (replacement of the PSD) is required. The FSD will allow to avoid autocorrelations and spurious correlations between subevents. Finally, the CBM performance for measurements of other flow harmonics (v_2, v_3) of multi-strange hyperons will be investigated.

Publications and presentations

Results of this doctoral work were published in the following papers:

- O. Lubynets, I. Selyuzhenkov and V. Klochkov, Particles 4 (2021) no.2, 288-295 doi:10.3390/particles4020025
- O. Lubynets and I. Selyuzhenkov [CBM], PoS FAIRness2022 (2023), 034 doi:10.22323/1.419.0034

Author contributed to papers published with primary authorship of collaborators:

- I. Segal, O. Lubynets, I. Selyuzhenkov, V. Klochkov [CBM], J. Phys. Conf. Ser. 1690 (2020) no.1, 012107 doi:10.1088/1742-6596/1690/1/012107
- S. Khan, V. Klochkov, O. Lavoryk, O. Lubynets, A. I. Khan, A. Dubla and I. Selyuzhenkov, EPJ Web Conf. 259 (2022), 13008 doi:10.1051/epjconf/202225913008.

Results of this thesis were presented by author at following conferences and workshops:

- DPG Spring meeting (Dresden 2023) - parallel talk;
- FAIR Next Generation Scientists Workshop (Paralia 2022) - talk;
- Quark Matter conference (Krakow 2022) - poster;
- DPG Spring meeting (online 2022) - parallel talk;

- Workshop “Physics Performance Studies at FAIR and NICA” (online 2021) - talk;
- International conference “NUCLEUS” (online 2021) - parallel talk;
- DPG Autumn meeting (online 2021) - parallel talk;
- FAIR-NICA centrality and flow workshop (online 2020) - talk.

Author contributed to results presented by collaborators at following events:

- Quark Matter conference (Houston 2023) - poster;
- Strangeness in Quark Matter conference (online 2021) - parallel talk.

Appendix A

Box selection optimization

In this appendix the procedure of selection criteria optimization is described. It is illustrated with an example of $\Lambda \to p\pi^-$ decay reconstruction in 100k Au-Au collisions with beam momentum $12A\,\mathrm{GeV}/c$ simulated with UrQMD model.

At the first stage all possible candidates are reconstructed witout any selection on them. Then distribution for each topological variable is built both for signal and background, and background distribution is normalized on the same integral with signal (see Fig. A.1). Some topological variables have different shapes for signal and background (χ^2_{prim}, $L/\Delta L$, $\cos\alpha\{\Lambda,\ p\}$) and therefore can serve as a good discriminator between them, while other variables have very similar shapes for signal and background (χ^2_{geo}, DCA, χ^2_{topo}) and are not good for separation between signal and background (at least at this stage). This fact can be also expressed in terms of relation between efficiency and background rejection, see Fig. A.2. Here we define efficiency ε as a function of topological variable X as a ratio between signal S preserved with certain cut on topological variable to the total amount of signal without any cuts: $\varepsilon(X) = S_{\text{remain}}(X)/S_{\text{total}}$. Analogically background rejection BR is defined as a ratio between amount of background B rejected with certain cut and the total amount of background without any cuts: $BR(X) = B_{\text{rejected}}(X)/B_{\text{total}}$. Perfect selection corresponds to the point $(1; 1)$ on the $\varepsilon - BR$ plot while 45°-line corresponds to the fully luck choose when topological variable has no discriminating power. As one can see in Fig. A.2 χ^2_{geo}, DCA, χ^2_{topo} topological variables have $\varepsilon - BR$ trajectories close to upper right corner therefore we apply selection on them at the first stage.

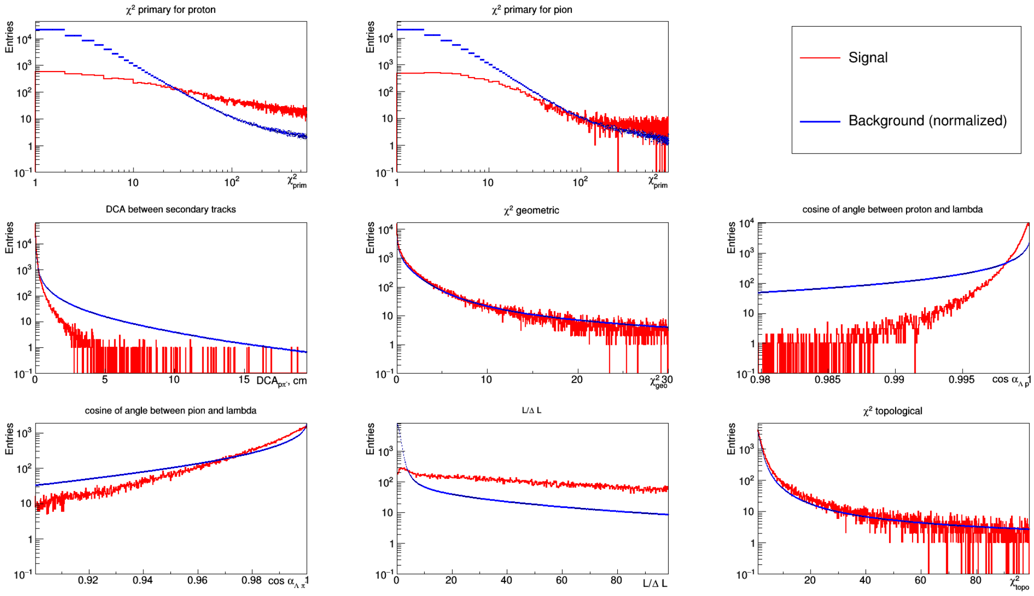

Figure A.1: Topological variables distribution without any selection. Background normalization coefficient $2.7 \cdot 10^{-4}$.

Fig. A.3, left, shows $\chi^2_{\text{prim},\ p}$ distribution for signal and background. A lower-value cut is applied in order to reject combinatorial background formed with primary protons having low χ^2_{prim} (some signal is also lost after this selection, but it is unavoidable). Numerical value $\chi^2_{\text{prim},\ p} = 26$ of this cut (and all the rest) is chosen in the point of crossing signal and normalized background distributions. This criterion corresponds to the maximization of $\varepsilon^2 + BR^2$ that is quite logical since one wants to have both efficiency and background rejection high enough. In Fig. A.3 and further application of the cut is illustrated by crossing out the region which is rejected by this cut.

Fig. A.3, right, shows $\chi^2_{\text{prim},\ \pi^-}$ distribution for signal and background. A lower-value cut 110 is applied on this variable. It is worth noting that numerical

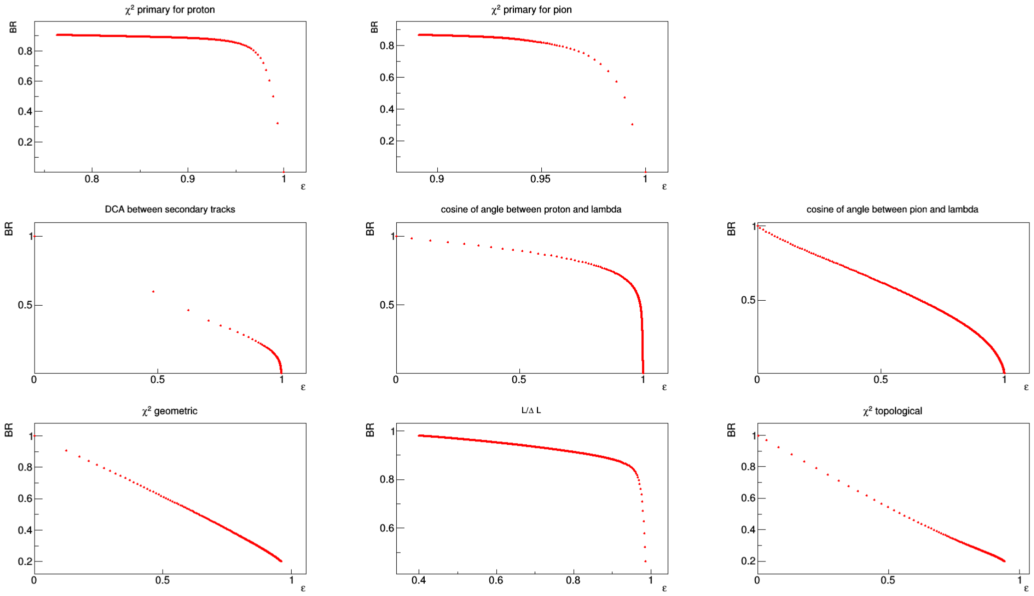

Figure A.2: Efficiency vs background rejection relation for topological variables. No selection applied.

values of χ^2_{prim} cuts for proton and pion are different because of different mass, and therefore kinematics, of these particles: pion is softer while proton is more straightforward particle.

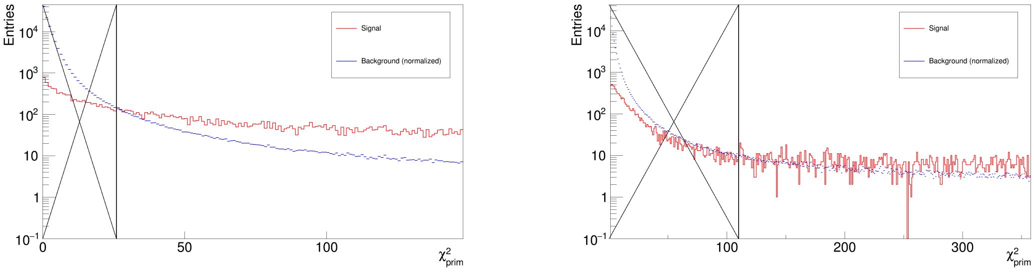

Figure A.3: (**left**) $\chi^2_{\text{prim},\ p}$, (**right**) $\chi^2_{\text{prim},\ \pi^-}$ distribution without any selection. Cut off values with $\chi^2_{\text{prim},\ p} > 26$, $\chi^2_{\text{prim},\ \pi^-} > 110$.

Fig. A.4, left, shows a distribution of the cosine of the angle between Λ and proton momenta. Due to kinematics reasons (that $m_p \approx 0.85 m_\Lambda$ and that CBM is a fixed target experiment) protons originating from Λ decay in general have momentum closer to mother particle than protons participating in construction of background Λ-candidate. A lower-value cut $\cos\alpha\{\Lambda, p\} = 0.99825$ is applied. It should be noted that $\cos\alpha\{\Lambda, p\}$ is implicitly correlated with kinematics of the Λ-candidate (momentum, rapidity, invariant mass) and therefore one needs to be careful with cutting on this variable to avoid spoiling the shape of the invariant mass distribution of background candidates (i.e. obtaining non-smooth structures in the region of the signal peak) or rejecting all signal candidates in a certain kinematic range. Fig. A.4, right, shows a distribution of the cosine of the angle between Λ and pion momenta. These distributions for signal and background are very similar because pion is much lighter than Λ-baryon, thus it is much softer than proton and does not have preferential direction of its momentum along mother particle momentum. That is why no cuts on this variable are applied.

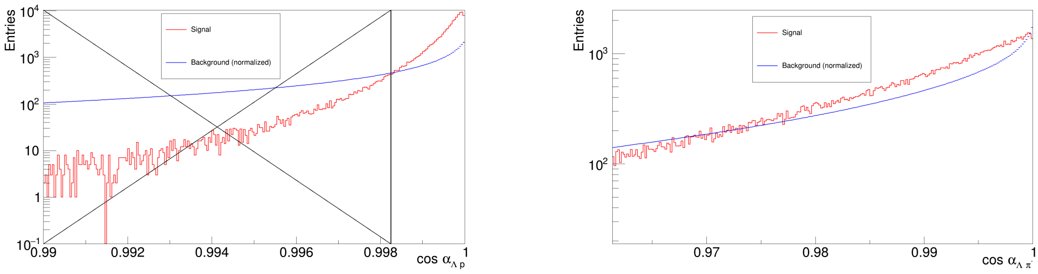

Figure A.4: (**left**) $\cos\alpha\{\Lambda, p\}$, (**right**) $\cos\alpha\{\Lambda, \pi^-\}$ distribution without any selection. Cut off values with $\cos\alpha\{\Lambda, p\} < 0.99825$, no cut off on $\cos\alpha\{\Lambda, \pi^-\}$.

In Fig. A.5 a distribution of $L/\Delta L$ is shown. A lower-value cut $L/\Delta L = 4$ is applied to this quantity in order to reject Λ-candidates constructed mostly from primary protons and pions.

After the first set of cuts is applied, all the distributions of topological variables are modified, see Fig. A.6. One can see that those of them which at the first step were not effective discriminators between signal and background, now can be successfully used in candidates selection.

Fig. A.7, left, shows the DCA distribution of signal and background after ap-

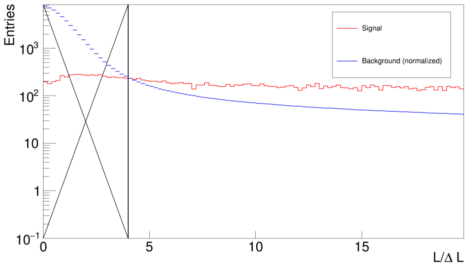

Figure A.5: $L/\Delta L$ distribution without any selection. Cut off values with $L/\Delta L < 4$.

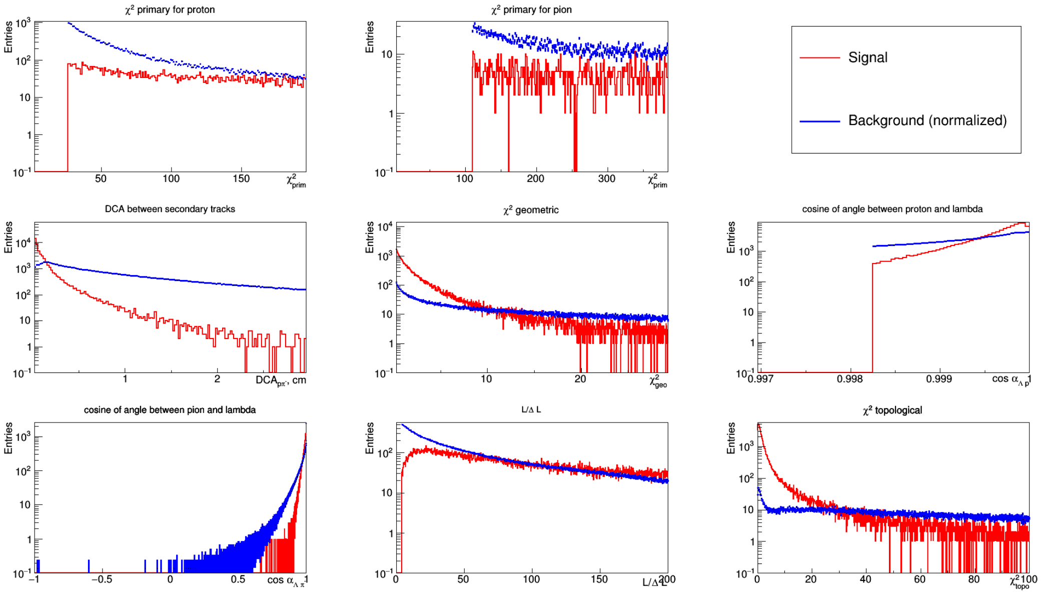

Figure A.6: Topological variables distribution after application of the first set of selection cuts. Background normalization coefficient $7.1 \cdot 10^{-3}$.

plication the first set of selection cuts. An upper-value cut $DCA = 0.15\,\mathrm{cm}$ is applied in order to reject those $p\pi^-$ pairs which do not approach close to each other and therefore probably do not originate from a Λ-decay. For the same reasons a χ^2_{geo}, which is in some sense a dimensionless distance between daughter tracks, is cut at 11 with an upper-value cut, see Fig. A.7, right.

Finally, in Fig. A.8, left, a distribution of χ^2_{topo} is shown, which describes how closely to the primary vertex an extrapolated mother's trajectory approaches. An upper-value cut at $\chi^2_{\mathrm{topo}} = 29$ is applied to this variable in order to reject

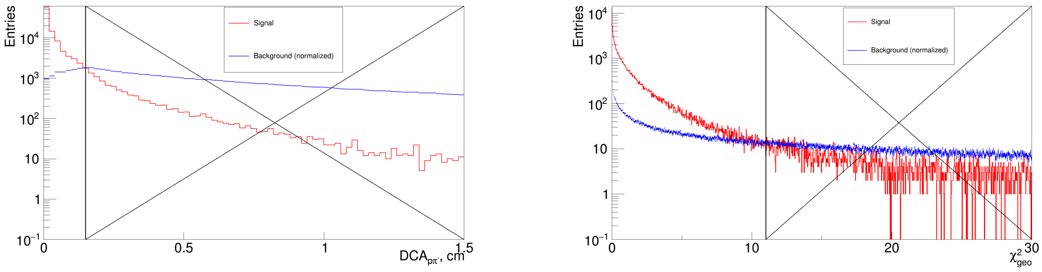

Figure A.7: (**left**) DCA, (**right**) χ^2_{geo} distribution after application of the first set of selection cuts. Cut off values with $DCA > 0.15\,\text{cm}$, $\chi^2_{\text{geo}} > 11$.

Λ-candidates originating not from the primary vertex and most probable being background. It should be noted that χ^2_{topo} is also a discriminator between primary and secondary Λs (e.g. originating from the decay of multi-strange hyperon). That is why cut on this variable can be used for feed-down suppression or vice versa for selection of secondary Λ-candidates for cascade decays reconstruction.

Fig. A.8, right, shows an invariant mass distribution of Λ-candidates selected both with standard selection cuts present in KFParticleFinder and cuts optimized according to the procedure described in this appendix. As one can see this procedure allows to improve signal-to-background ratio from 9 to 48.

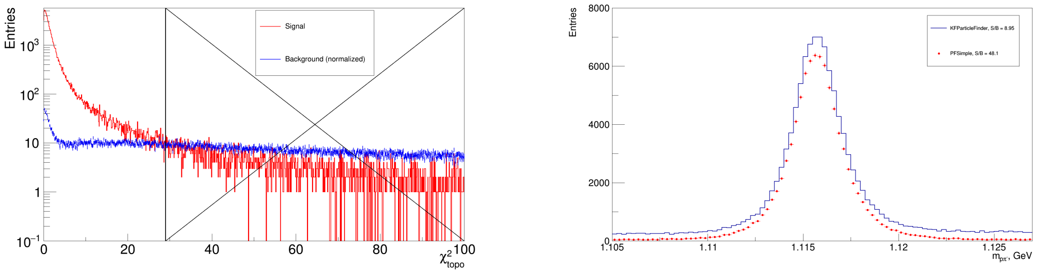

Figure A.8: (**left**) χ^2_{topo} distribution after application of the first set of selection cuts. Cut off values with $\chi^2_{\text{topo}} > 29$. (**right**) Invariant mass distribution with default selection criteria (blue lines) and optimized according to the current procedure (red circles).

Appendix B

Q-vectors and corrections

Fig. B.1, left, shows the distribution of x- and y-components of $\mathbf{Q}_1$-vectors of reconstructed Λ-baryons in a certain p_T-y-centrality bin. They have maxima at ±1 because of transition from uniform (in first approximation) azimuthal angle φ distribution to distributions of $\cos\varphi$ and $\sin\varphi$ which are distributed by $\sim 1/\sqrt{1-\xi^2}$, where ξ stands for $\cos\varphi$ and $\sin\varphi$[1]. Existing modulations of x- and y-components distributions originate from non-uniformities of φ distribution. Fig. B.1, right, illustrates the distribution of x- and y-components of the $\mathbf{Q}_1$-vector of particles getting into the PSD2 submodule. The distribution of $\mathbf{Q}_1$-vector looks different from that of Λ-baryons because unlike Λs the signal in the PSD2 is formed by a lot of particles, and the $\mathbf{Q}_1$-vector is normalized by sum of weights. The x- and y- components of the $\mathbf{Q}_1$ look different: the x is shifted to left side and has more smooth shape on the top - due to magnetic field applied in y-direction.

Fig. B.2, left and middle, shows the values of corrections for the $\mathbf{Q}_1$-vector of reconstructed Λ-baryons as a function of centrality in a certain kinematics bin.

---

[1] For understanding the shape of the distribution it is important to keep in mind that Λ-baryons are relatively rare, and in a single event in a certain kinematics bin usually there is no more than one entry - therefore $\mathbf{Q}_1$-vector normalizations by magnitude, by sum of weights, or absence of normalization are effectively identical. For more abundant particles (e.g. pions) the shape would be different, as well as for the PSD - see Fig. B.1, right.

Notations $\bar{c}_i(\bar{s}_i)$ are taken from [133] and are equal to i-th cosine (sine) term of the acceptance function Fourier decomposition. Coefficients $\bar{c}_1$ and $\bar{s}_1$ are related to recentering while $\bar{c}_2$ and $\bar{s}_2$ - to twist and rescaling of the $\mathbf{Q}_1$. Azimuthal corrections for reconstructed Λ are of order of few percents. Fig. B.2, right, illustrates the values of recentering corrections applied to the $\mathbf{Q}_1\{PSD\}$ (twist and rescaling are not applied to it). The recentering correction for x-direction is of order of few percents and increases for more peripheral collisions, while correction for y-direction is lower by one order of magnitude.

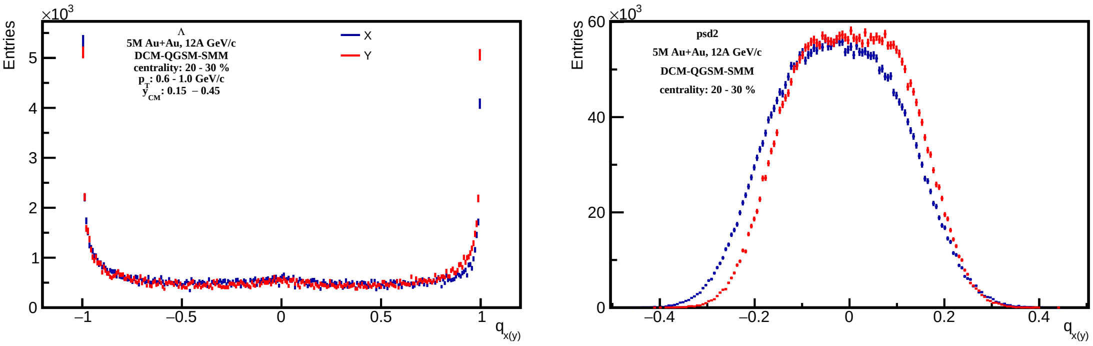

Figure B.1: Distribution of the $\mathbf{Q}_1$-vector of (**left**) reconstructed Λ-baryons (**right**) particles getting into the PSD.

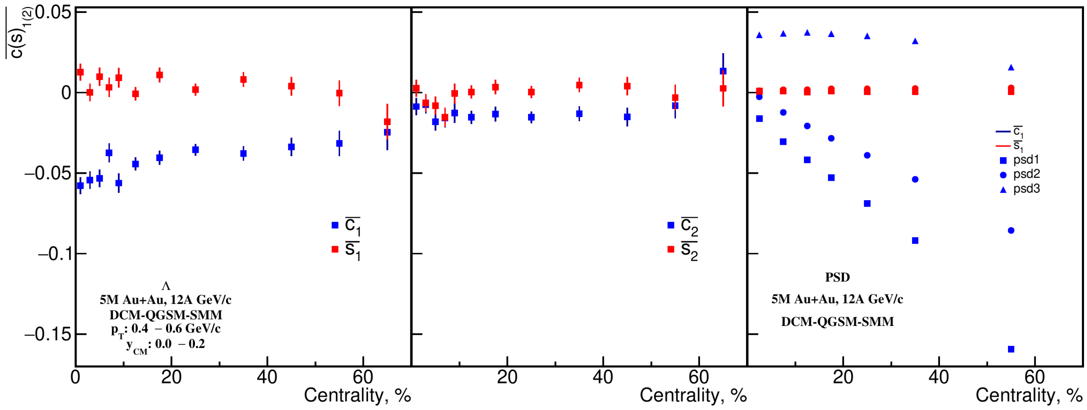

Figure B.2: Corrections values for the $\mathbf{Q}_1$-vectors a function of centrality: (**left**) of reconstructed Λ-baryons, first harmonic, (**middle**) second harmonic, (**right**) of particles getting into the PSD2 submodule, first harmonic.

Appendix C

Compilation of flow results

Resolution studies

Fig. C.1 illustrates the centrality dependence of the resolution correction factor R_1 (MC-true resolution) for different event generators and beam momenta. Top panels show R_1 calculated in the event plane mode (with $\mathbf{Q}_n$-vector normalization on its magnitude), while bottom panels show R_1 calculated in the scalar product mode (with $\mathbf{Q}_n$-vector normalization on its sum of weights).

The 1-st and 2-nd rows of Fig. C.2 show centrality dependence of $\mathbf{Q}_n$-vectors product for the 3- and 4-subevents methods respectively and demonstrate whether its factorization is fulfilled (according to Eq. 4.4). The 3-d and 4-th rows of the same figure show centrality dependence of R_1 calculated with 3- and 4-subevents methods respectively compared to the MC-true resolution. Estimates of systematic uncertainties as differences between reconstructed and MC-true values of R_1 (in percents of MC-true value) are shown in Tab. C.1.

$p_T - y$ dependence of v_1, dv_1/dy slope and $v_1|_{y=0}$ offset vs centrality

Three simulation setups are compared (varying event generators and beam momenta). *Note:* UrQMD simulations are performed in EOS=0 mode (pure cascade mode, no potentials), and in this approach the directed flow of Λ-hyperons is not

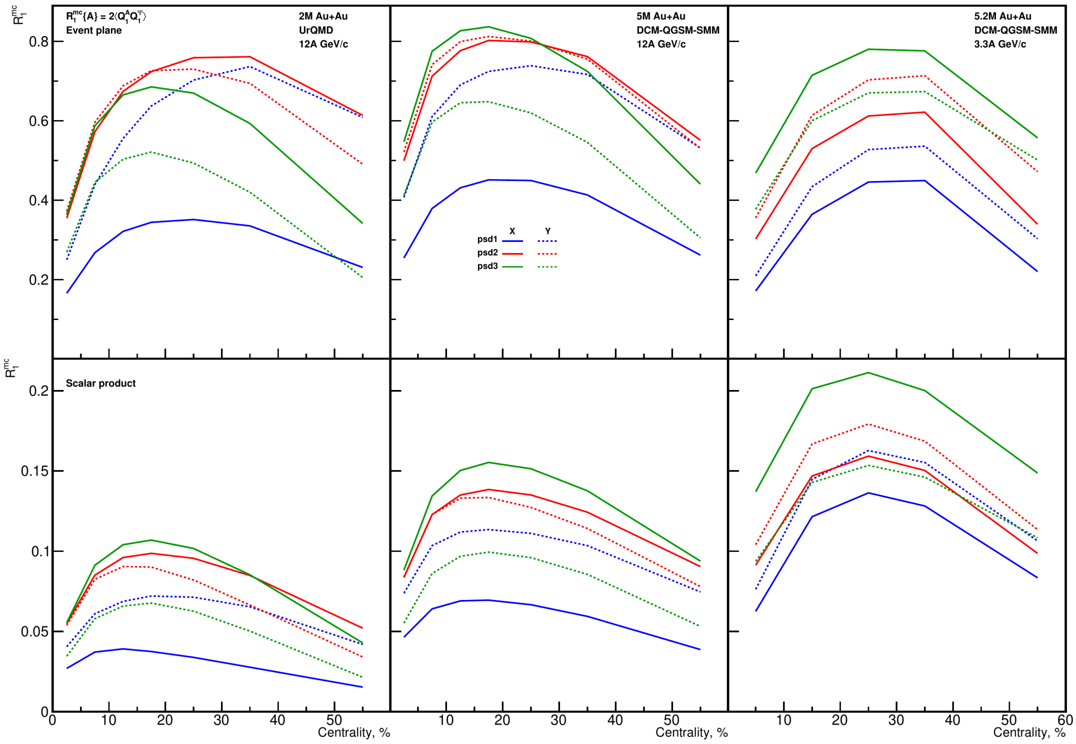

Figure C.1: Centrality dependence of the MC-true resolution correction factor determined in (**top**) event plane mode, (**bottom**) scalar product mode. The input is generated with (**left**) u-12, (**middle**) d-12, (**right**) d-3.

consistent with experimental data.

Fig. C.3, C.4 illustrate the directed flow of Λ-hyperons and K_S^0-mesons dependence on rapidity and transverse momentum respectively for 20-30% central events. The $v_1(y)$ dependence is fitted with the 3-d order polynomial function. Directed flow of simulated particles is calculated relative to the MC-true reaction plane. Filled areas represent v_1 value with its statistical uncertainty.

Fig. C.5 illustrates the directed flow of Λ and K_S^0 as a function of rapidity for 20-30% central events in different transverse momentum ranges. Directed flow of reconstructed particles is calculated relative to the event plane estimated with spectators registered in the PSD. The resolution correction factor is determined via 4-subevents method using π^+ for 4-th subevent. A set of 6 measurements of v_1 is obtained: 2 components of v_1 (v_{1x} and v_{1y}) are calculated relative to spec-

Sub-event	**Comp.**	**12A GeV/c**			**3.3A GeV/c**		
		Centrality					
		0-10%	**10-40%**	**40-70%**	**0-10%**	**10-40%**	**40-70%**
PSD1	x	37	17	43	119	30	158
	y	9	-2	-15	81	23	43
PSD2	x	70	37	117	220	58	201
	y	50	23	88	170	40	76
PSD3	x	-13	-13	-10	-8	-5	11
	y	2	-1	17	3	-2	-2
Average		26	10	40	97	24	81

Sub-event	**Comp.**	**12A GeV/c**			**3.3A GeV/c**		
		Centrality					
		0-10%	**10-40%**	**40-70%**	**0-10%**	**10-40%**	**40-70%**
PSD1	x	6	-1	10	47	13	74
	y	4	-3	-5	41	11	21
PSD2	x	9	-1	8	44	10	68
	y	8	-1	-2	40	10	18
PSD3	x	12	2	18	37	10	64
	y	7	0	5	33	9	16
Average		8	-0	6	40	10	44

Table C.1: Discrepancies (%) of resolution determination with (**top**) 3- (**bottom**) 4-subevents method.

tators in 3 subevents (PSD1, PSD2 and PSD3). v_1 is calculated as a mean value of this set, and systematic uncertainty is estimated as a standard deviation of the set. Filled areas represent MC-true input with its statistical uncertainty, full squares - flow reconstructed in data-driven approach using methods described in Sec. 4.1-4.4. Error bars visualize statistical uncertainties, and filled semi-opaque rectangles represent systematic uncertainties.

Figures C.6, C.7 illustrate the directed flow slope and offset for Λ-hyperons and K^0_S-mesons respectively reconstructed in a data-driven approach. Polynomial fit of 3-d order for the slope and offset extraction was used.

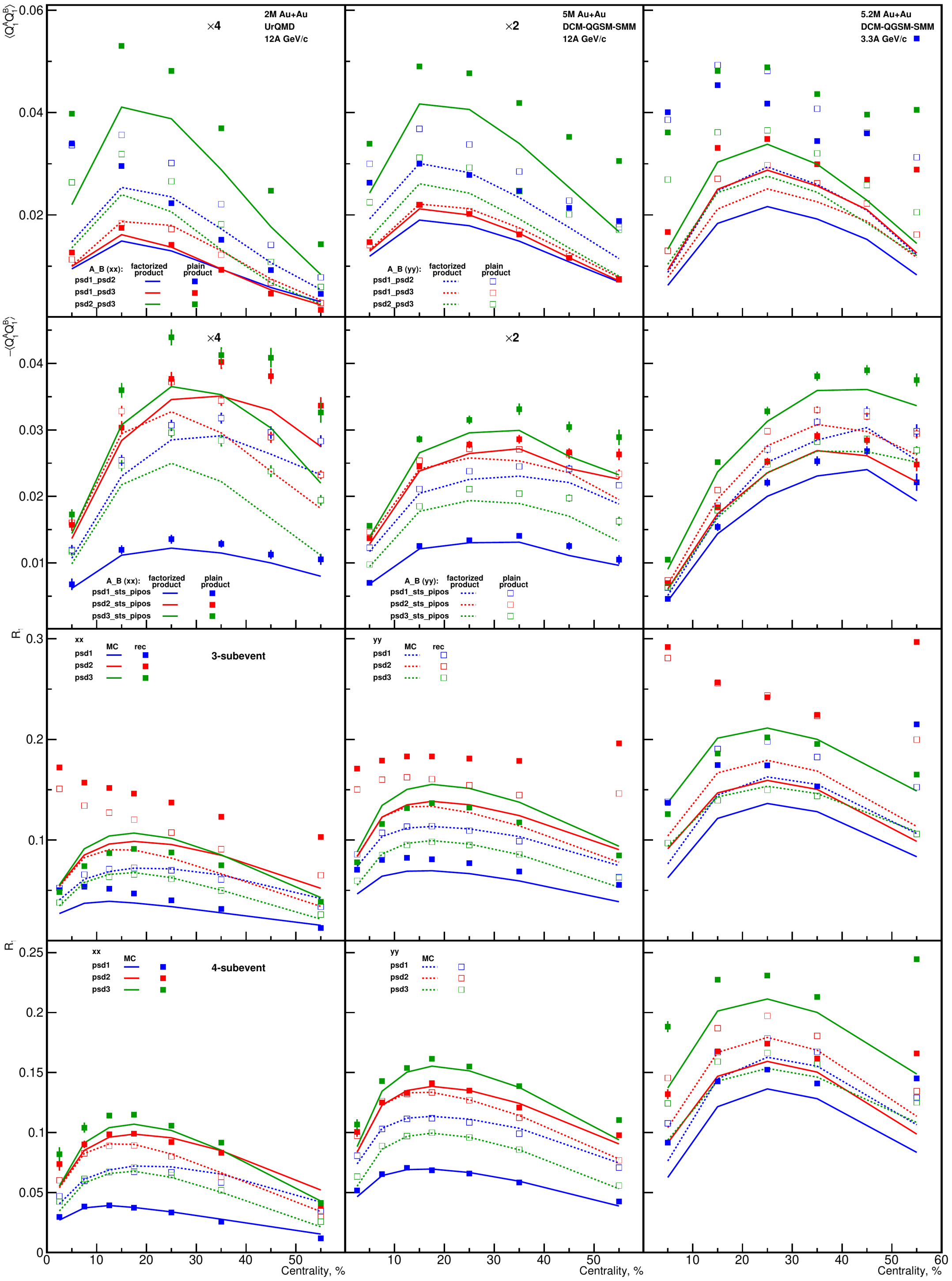

Figure C.2: Centrality dependence of Q_1-vectors product factorization (see Eq. 4.4: l.h.s. - markers, r.h.s. - lines) for (**1-st row**) 3- **2-nd row**) 4-subevents method and resolution correction factor calculated with (**3-d row**) 3- (**4-th row**) 4-subevents method (markers) compared to MC-true (lines). The input is generated with (**left**) u-12, (**middle**) d-12, (**right**) d-3.

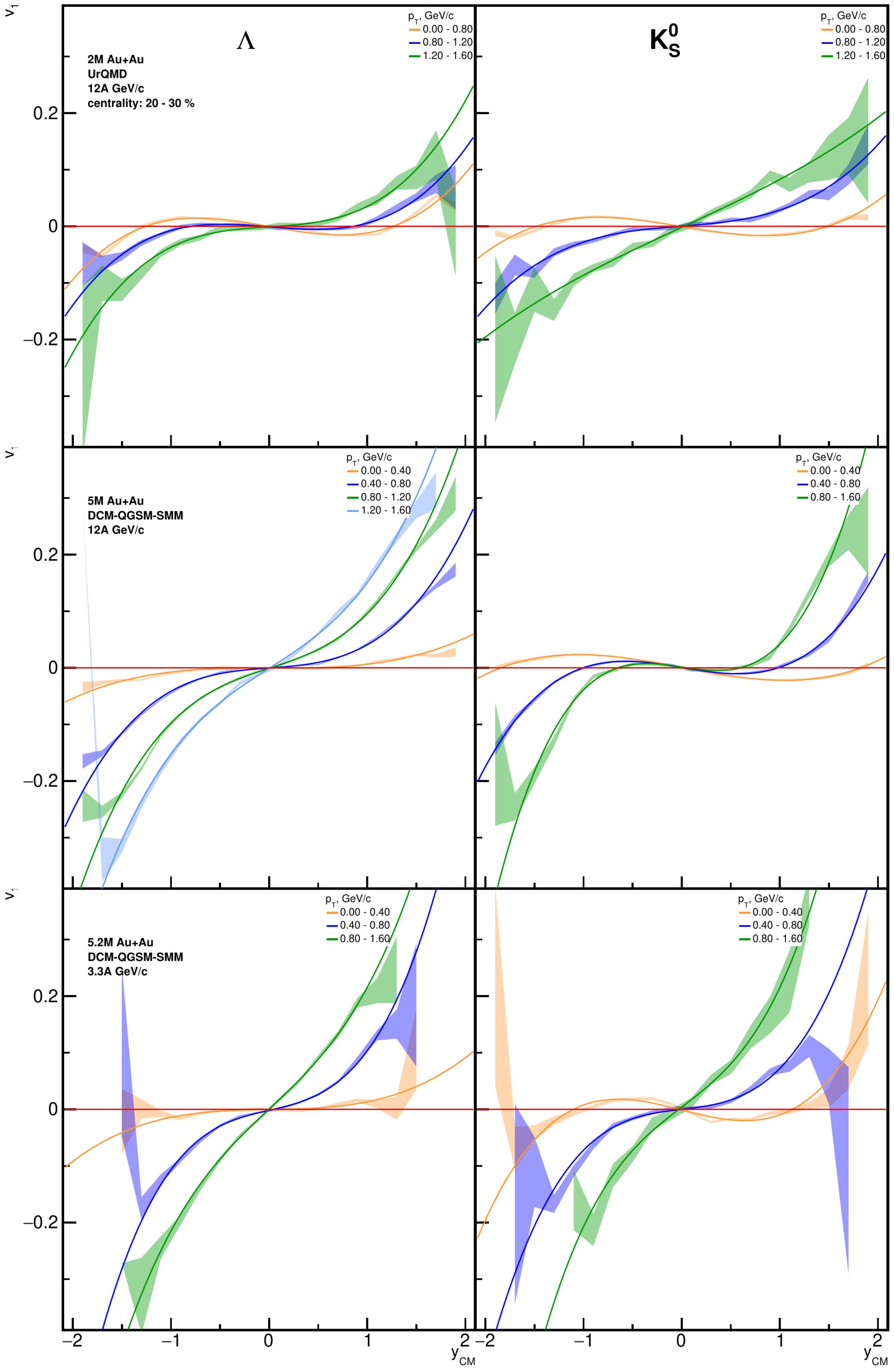

Figure C.3: Simulated $v_1(y)$ of (**left**) Λ-baryons and (**right**) K^0_S calculated relative to the MC-true reaction plane. $20-30\%$ central events are selected. The input is generated with (**top**) u-12, (**middle**) d-12 and (**bottom**) d-3. Performed pol3 fit in rapidity range $y \in [-2;\ 2]$.

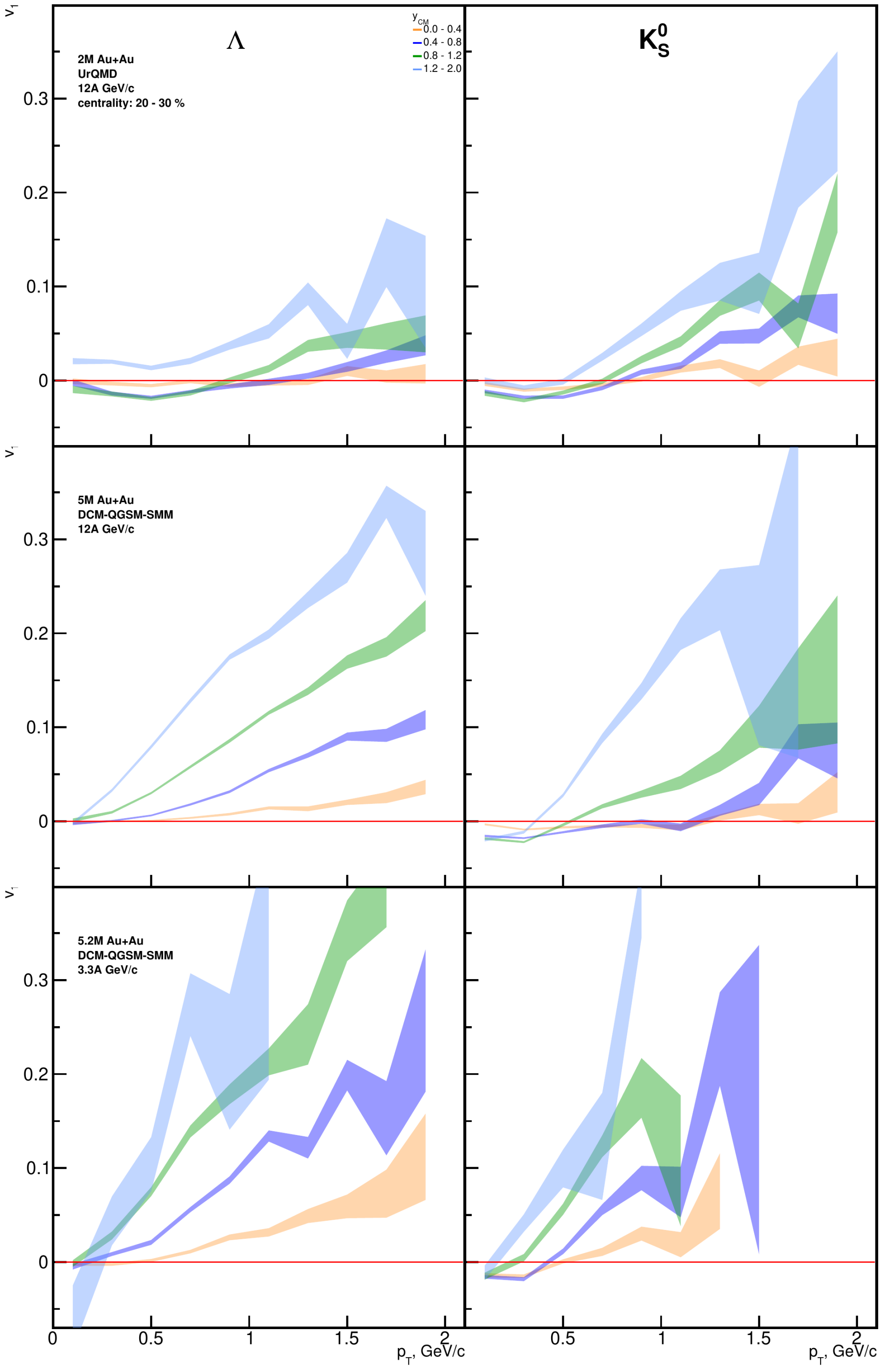

Figure C.4: Simulated $v_1(p_T)$ of (**left**) Λ-baryons and (**right**) K^0_S calculated relative to the MC-true reaction plane. $20-30\%$ central events are selected. The input is generated with (**top**) u-12, (**middle**) d-12 and (**bottom**) d-3.

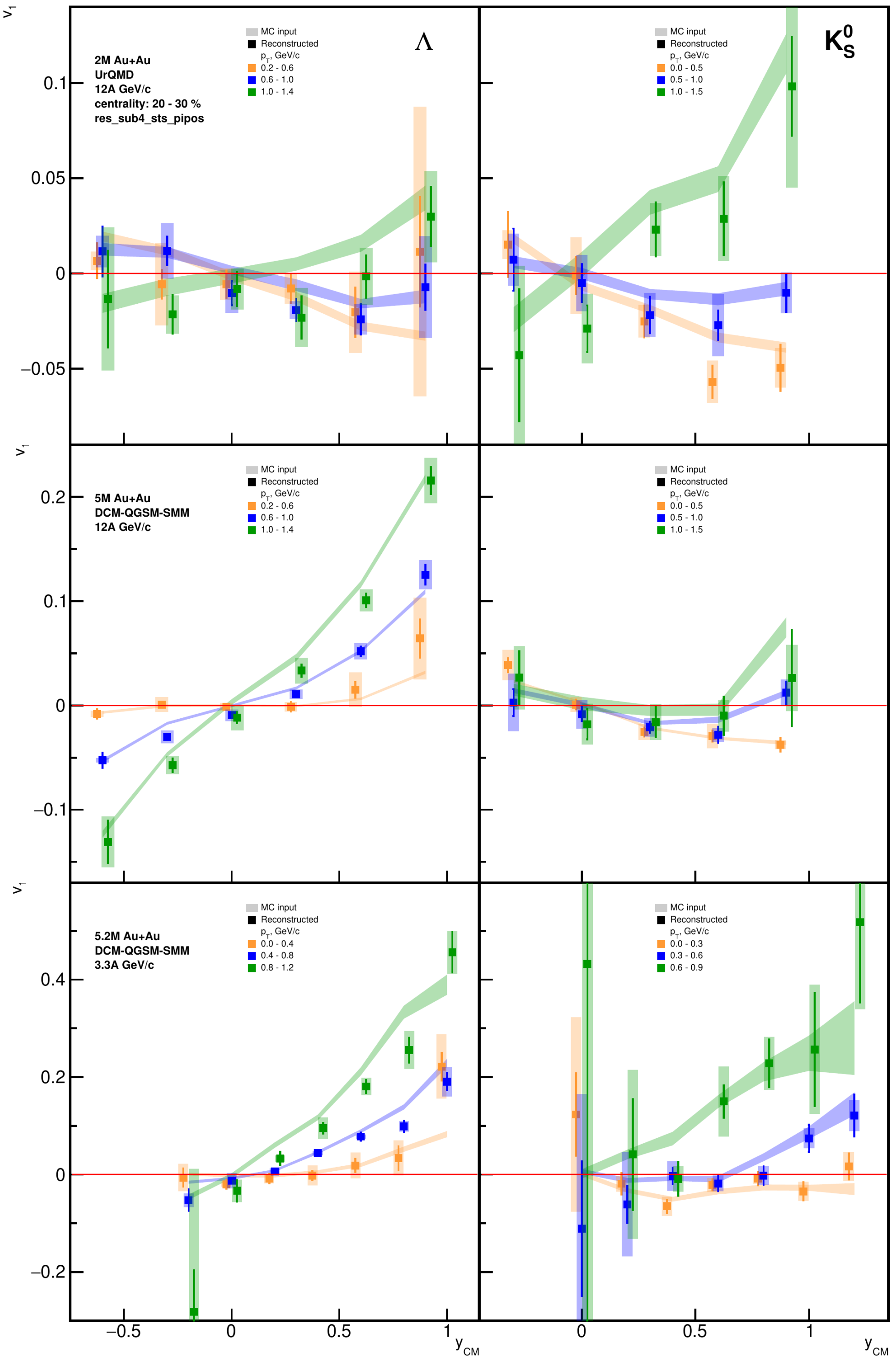

Figure C.5: $v_1(y)$ measured relative to spectators registered in PSD with resolution determined via 4-subevents method. The input is generated with (**top**) u-12, (**middle**) d-12 and (**bottom**) d-3 for (**left**) Λ and (**right**) K^0_S.

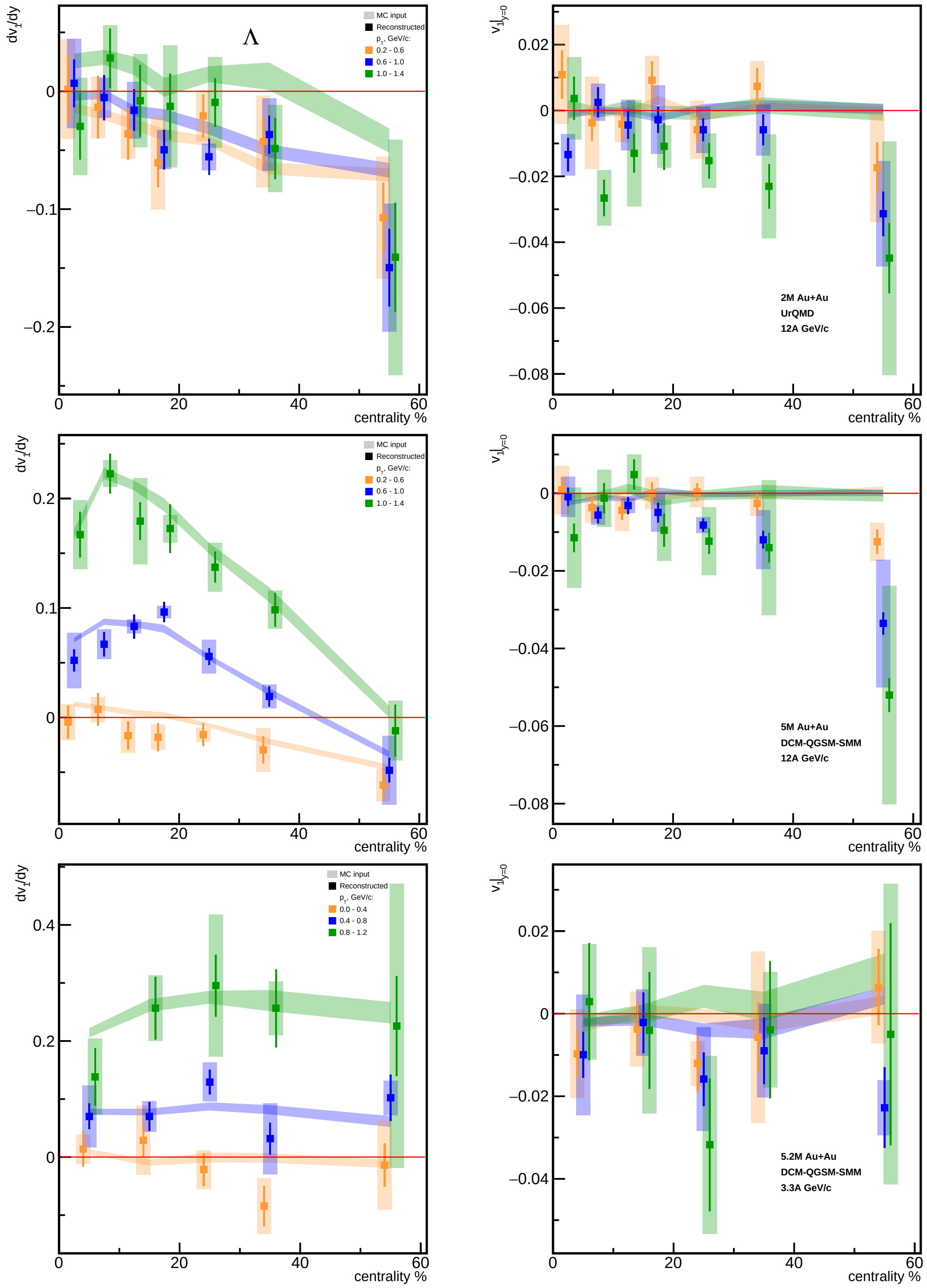

Figure C.6: (**left**) Directed flow slope dv_1/dy and (**right**) intercept $v_1|_{y=0}$ of Λ-baryons as a function of centrality. v_1 is calculated relative to spectators registered in the PSD with resolution determined via 4-subevents method. The input is generated with (**top**) u-12, (**middle**) d-12and (**bottom**) d-3. Performed pol3 fit.

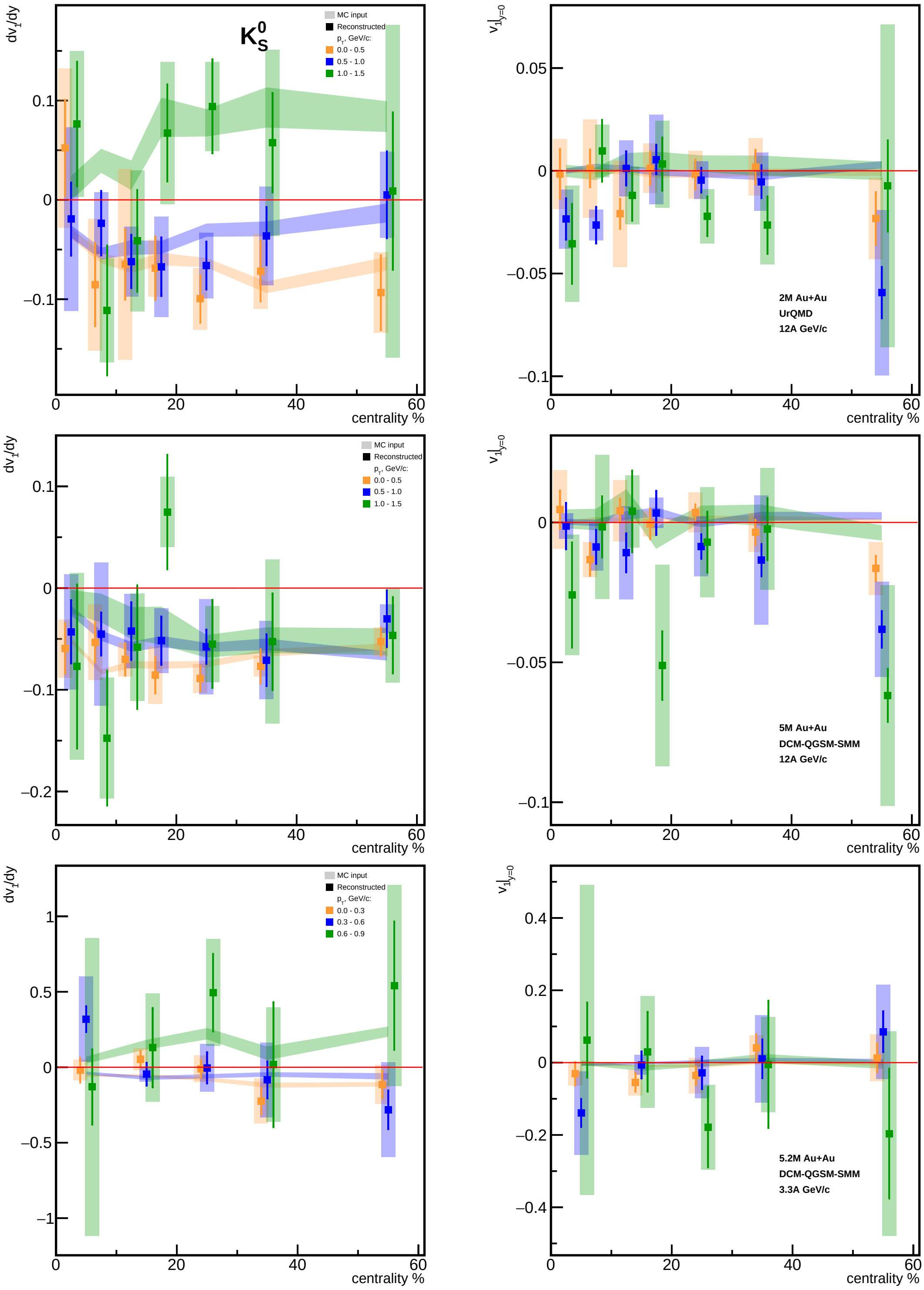

Figure C.7: (**left**) Directed flow slope dv_1/dy and (**right**) intercept $v_1|_{y=0}$ of K^0_S-mesons as a function of centrality. v_1 is calculated relative to spectators registered in the PSD with resolution determined via 4-subevents method. The input is generated with (**top**) u-12, (**middle**) d-12and (**bottom**) d-3. Performed pol3 fit.

Bibliography

[1] C. S. Wu, et al. Experimental test of parity conservation in beta decay. *Phys. Rev.*, 105:1413–1415, Feb 1957.

[2] S. Weinberg. A model of leptons. *Phys. Rev. Lett.*, 19:1264–1266, Nov 1967.

[3] A. Salam et al. Weak and electromagnetic interactions. *Nuovo Cim.*, 11:568–577, 1959.

[4] S. L. Glashow. The renormalizability of vector meson interactions. *Nucl. Phys.*, 10:107–117, 1959.

[5] D. J. Gross et al. Ultraviolet Behavior of Nonabelian Gauge Theories. *Phys. Rev. Lett.*, 30:1343–1346, 1973.

[6] H. D. Politzer. Reliable Perturbative Results for Strong Interactions? *Phys. Rev. Lett.*, 30:1346–1349, 1973.

[7] F. Gao et al. Chiral phase structure and critical end point in QCD. *Phys. Lett. B*, 820:136584, 2021.

[8] G. Baym, et al. From hadrons to quarks in neutron stars: a review. *Rept. Prog. Phys.*, 81(5):056902, 2018.

[9] C. Reed. Penn State University.

[10] D. Berry. NASA/Swift.

[11] I. Selyuzhenkov. Strangeness in Quark Matter. Status of the CBM experiment at FAIR. `https://indico.cern.ch/event/755366/contributions/3428155/`, 2019. Accessed: 2024-01-10.

[12] J. R. Oppenheimer et al. On massive neutron cores. *Phys. Rev.*, 55:374–381, 1939.

[13] K. Gendreau et al. Searching for a pulse. *Nature Astronomy*, 1(12):895–895, 2017.

[14] X. Roca-Maza, et al. Influence of the nuclear symmetry energy on the structure and composition of the outer crust. 9 2011.

[15] P. Demorest, et al. Shapiro Delay Measurement of A Two Solar Mass Neutron Star. *Nature*, 467:1081–1083, 2010.

[16] B. P. Abbott et al. Observation of Gravitational Waves from a Binary Black Hole Merger. *Phys. Rev. Lett.*, 116(6):061102, 2016.

[17] B. P. Abbott et al. GW170817: Observation of Gravitational Waves from a Binary Neutron Star Inspiral. *Phys. Rev. Lett.*, 119(16):161101, 2017.

[18] B. P. Abbott et al. Multi-messenger Observations of a Binary Neutron Star Merger. *Astrophys. J. Lett.*, 848(2):L12, 2017.

[19] M. Hanauske, et al. Concluding Remarks: Connecting Relativistic Heavy Ion Collisions and Neutron Star Mergers by the Equation of State of Dense Hadron- and Quark Matter as signalled by Gravitational Waves. *J. Phys. Conf. Ser.*, 878(1):012031, 2017.

[20] J. Rafelski, editor. *Melting Hadrons, Boiling Quarks - From Hagedorn Temperature to Ultra-Relativistic Heavy-Ion Collisions at CERN: With a Tribute to Rolf Hagedorn*. Springer, 2016.

[21] BNL webpage. `https://www.bnl.gov/world/`. Accessed: 2023-06-22.

[22] JINR webpage. `http://www.jinr.ru/main-en/`. Accessed: 2023-06-22.

[23] Y. J. Kim. Flow of strange particles from FOPI at SIS. *Int. J. Mod. Phys. A*, 22:608–611, 2007.

[24] W. Grimus et al. On a model with two zeros in the neutrino mass matrix. *J. Phys. G*, 31(7):693–702, 2005.

[25] HADES webpage. `https://hades.gsi.de/`. Accessed: 2023-06-22.

[26] M. N. Kapishin. The Fixed Target Experiment for Studies of Baryonic

Matter at the Nuclotron (BM@N). *Yad. Fiz.*, 7(6):543–550, 2016.

[27] M. Kapishin. Studies of baryonic matter at the BM@N experiment (JINR). *Nucl. Phys. A*, 982:967–970, 2019.

[28] N. Abgrall et al. NA61/SHINE facility at the CERN SPS: beams and detector system. *JINST*, 9:P06005, 2014.

[29] STAR webpage. `https://www.star.bnl.gov/`. Accessed: 2023-06-22.

[30] K. Aamodt et al. The ALICE experiment at the CERN LHC. *JINST*, 3:S08002, 2008.

[31] N. S. Geraksiev. The Nuclotron-based Ion Collider Facility Project. The Physics Programme for the Multi-Purpose Detector. *J. Phys. Conf. Ser.*, 1023(1):012030, 2018.

[32] H. Sako et al. Towards the heavy-ion program at J-PARC. *Nucl. Phys. A*, 931:1158–1162, 2014.

[33] B. Kardan. Centrality determination at 1.23 AGeV Gold-Gold collision and readout-electronics for the HADES electromagnetic calorimeter. Master's thesis, Goethe-Universität, Frankfurt, Germany, June 2015.

[34] R. L. Workman et al. Review of Particle Physics. *PTEP*, 2022:083C01, 2022.

[35] P. Koch, et al. Strangeness in Relativistic Heavy Ion Collisions. *Phys. Rept.*, 142:167–262, 1986.

[36] V. Koch et al. Equilibrium in heavy ion collisions. *Acta Physica Hungarica A) Heavy Ion Physics*, 21(2-4):273–278, nov 2004.

[37] S. V. Afanasiev et al. Energy dependence of pion and kaon production in central Pb + Pb collisions. *Phys. Rev. C*, 66:054902, 2002.

[38] F. Antinori et al. Enhancement of hyperon production at central rapidity in 158-A-GeV/c Pb-Pb collisions. *J. Phys. G*, 32:427–442, 2006.

[39] P. Braun-Munzinger, et al. Chemical equilibration in Pb + Pb collisions at the SPS. *Phys. Lett. B*, 465:15–20, 1999.

[40] G. Agakishiev et al. Statistical hadronization model analysis of hadron

yields in p + Nb and Ar + KCl at SIS18 energies. *Eur. Phys. J. A*, 52(6):178, 2016.

[41] W. Scheid, et al. Nuclear Shock Waves in Heavy-Ion Collisions. *Phys. Rev. Lett.*, 32:741–745, 1974.

[42] R. Stock et al. Emission Patterns in Central and Peripheral Relativistic Heavy Ion Collisions. *Phys. Rev. Lett.*, 44:1243–1246, 1980.

[43] H. A. Gustafsson et al. Collective Flow Observed in Relativistic Nuclear Collisions. *Phys. Rev. Lett.*, 52:1590–1593, 1984.

[44] Ilya Selyuzhenkov. Global polarization measurement in Au + Au collisions. *J. Phys. G*, 32:S557–S562, 2006.

[45] I. Selyuzhenkov. Centrality dependence of hyperon global polarization in Au+Au collisions at RHIC. *J. Phys. G*, 34:S1099–1102, 2007.

[46] I. Selyuzhenkov. Anti-Lambda hyperon global polarization in Au+Au collisions at RHIC. In *International Workshop on Hadron Physics and Property of High Baryon Density Matter*, 2 2007.

[47] B. I. Abelev et al. Global polarization measurement in Au+Au collisions. *Phys. Rev. C*, 76:024915, 2007. [Erratum: Phys.Rev.C 95, 039906 (2017)].

[48] J. Steinheimer, et al. Examination of directed flow as a signal for a phase transition in relativistic nuclear collisions. *Phys. Rev. C*, 89(5):054913, 2014.

[49] S. J. Barnett. Magnetization by rotation. *Phys. Rev.*, 6:239–270, Oct 1915.

[50] A. Einstein. Experimenteller nachweis der ampereschen molekularströme. *Naturwissenschaften*, 3(19):237–238, 1915.

[51] R. Takahashi, et al. Spin hydrodynamic generation. *Nature Physics*, 12(1):52–56, 2016.

[52] J. Kessler. *Polarized Electrons*, chapter Description of Polarized Electrons, pages 7–20. Springer Berlin, Heidelberg, 1976.

[53] F. Becattini et al. Polarization and Vorticity in the Quark–Gluon Plasma. *Ann. Rev. Nucl. Part. Sci.*, 70:395–423, 2020.

[54] L. Adamczyk et al. Global Λ hyperon polarization in nuclear collisions: evidence for the most vortical fluid. *Nature*, 548:62–65, 2017.

[55] O. Vitiuk, et al. Is different Λ and $\bar{\Lambda}$ polarization caused by different spatio-temporal freeze-out picture? *Phys. Lett. B*, 803:135298, 2020.

[56] J. Adam et al. Flow and interferometry results from Au+Au collisions at $\sqrt{s_{NN}} = 4.5$ GeV. *Phys. Rev. C*, 103(3):034908, 2021.

[57] F. J. Kornas. *Global polarization of Λ hyperons as a probe for vortical effects in A+A collisions at HADES.* PhD thesis, Darmstadt U., 2021. Chapter 7.1.

[58] R. Abou Yassine et al. Measurement of global polarization of Λ hyperons in few-GeV heavy-ion collisions. *Phys. Lett. B*, 835:137506, 2022.

[59] E. C. Halbert. Density patterns and energy-angle distributions from a simple cascade scheme for last Ne-20 + U-238 collisions. *Phys. Rev. C*, 23:295–330, 1981.

[60] B. Andersson, et al. A General Model for Jet Fragmentation. *Z. Phys. C*, 20:317, 1983.

[61] V. D. Toneev et al. Particle Emission in Light and Heavy Ion Reactions. *Nucl. Phys. A*, 400:173C–190C, 1983.

[62] J. Steinheimer, et al. Hypernuclei, dibaryon and antinuclei production in high energy heavy ion collisions: Thermal production versus Coalescence. *Phys. Lett. B*, 714:85–91, 2012.

[63] J. P. Bondorf, et al. Statistical multifragmentation of nuclei. *Phys. Rept.*, 257:133–221, 1995.

[64] N. Bohr. Neutron Capture and Nuclear Constitution. *Nature*, 137:344–348, 1936.

[65] J. Weil et al. Particle production and equilibrium properties within a new hadron transport approach for heavy-ion collisions. *Phys. Rev. C*, 94(5):054905, 2016.

[66] W. Cassing et al. Parton transport and hadronization from the dynamical

quasiparticle point of view. *Phys. Rev. C*, 78:034919, 2008.

[67] W. Cassing et al. Parton-Hadron-String Dynamics: an off-shell transport approach for relativistic energies. *Nucl. Phys. A*, 831:215–242, 2009.

[68] S. Gläßel, et al. Cluster and hypercluster production in relativistic heavy-ion collisions within the parton-hadron-quantum-molecular-dynamics approach. *Phys. Rev. C*, 105(1):014908, 2022.

[69] A. S. Botvina et al. Multifragmentation of spectators in relativistic heavy ion reactions. *Nucl. Phys. A*, 584:737–756, 1995.

[70] M. Baznat, et al. Monte-Carlo Generator of Heavy Ion Collisions DCM-SMM. *Phys. Part. Nucl. Lett.*, 17(3):303–324, 2020.

[71] N. S. Amelin, et al. Strangeness production in proton and heavy ion collisions at 200-A-GeV. *Phys. Rev. C*, 47:2299–2307, 1993.

[72] S. A. Bass et al. Microscopic models for ultrarelativistic heavy ion collisions. *Prog. Part. Nucl. Phys.*, 41:255–369, 1998.

[73] M. Bleicher et al. Relativistic hadron hadron collisions in the ultrarelativistic quantum molecular dynamics model. *J. Phys. G*, 25:1859–1896, 1999.

[74] C. Pinkenburg et al. Elliptic flow: Transition from out-of-plane to in-plane emission in Au + Au collisions. *Phys. Rev. Lett.*, 83:1295–1298, 1999.

[75] S. Soff, et al. Directed and elliptic flow. 3 1999.

[76] L. Fabbietti, et al. Study of the Strong Interaction Among Hadrons with Correlations at the LHC. *Ann. Rev. Nucl. Part. Sci.*, 71:377–402, 2021.

[77] T. Galatyuk. Future facilities for high μ_B physics. *Nucl. Phys. A*, 982:163–169, 2019.

[78] L. Adamczyk et al. Beam-Energy Dependence of the Directed Flow of Protons, Antiprotons, and Pions in Au+Au Collisions. *Phys. Rev. Lett.*, 112(16):162301, 2014.

[79] J. Thäder. Higher Moments of Net-Particle Multiplicity Distributions. *Nucl. Phys. A*, 956:320–323, 2016.

[80] M. A. Stephanov. On the sign of kurtosis near the QCD critical point. *Phys. Rev. Lett.*, 107:052301, 2011.

[81] J.-W. Chen, et al. Baryon susceptibilities, non-Gaussian moments, and the QCD critical point. *Phys. Rev. D*, 92(5):054019, 2015.

[82] J. Adam et al. Nonmonotonic Energy Dependence of Net-Proton Number Fluctuations. *Phys. Rev. Lett.*, 126(9):092301, 2021.

[83] P. M. Hohler et al. Is ρ-Meson Melting Compatible with Chiral Restoration? *Phys. Lett. B*, 731:103–109, 2014.

[84] R. Rapp et al. Thermal Dileptons as Fireball Thermometer and Chronometer. *Phys. Lett. B*, 753:586–590, 2016.

[85] T. Matsui et al. J/ψ Suppression by Quark-Gluon Plasma Formation. *Phys. Lett. B*, 178:416–422, 1986.

[86] M. C. Abreu et al. Anomalous J / psi suppression in Pb - Pb interactions at 158 GeV/c per nucleon. *Phys. Lett. B*, 410:337–343, 1997.

[87] A. Adare et al. J/ψ Production vs Centrality, Transverse Momentum, and Rapidity in Au+Au Collisions at $\sqrt{s_{NN}} = 200$ GeV. *Phys. Rev. Lett.*, 98:232301, 2007.

[88] Betty Abelev et al. J/ψ suppression at forward rapidity in Pb-Pb collisions at $\sqrt{s_{NN}} = 2.76$ TeV. *Phys. Rev. Lett.*, 109:072301, 2012.

[89] A. Andronic, et al. Production of light nuclei, hypernuclei and their antiparticles in relativistic nuclear collisions. *Phys. Lett. B*, 697:203–207, 2011.

[90] J. K. Ahn et al. Double-Λ hypernuclei observed in a hybrid emulsion experiment. *Phys. Rev. C*, 88(1):014003, 2013.

[91] A. S. Botvina, et al. Formation of hypermatter and hypernuclei within transport models in relativistic ion collisions. *Phys. Lett. B*, 742:7–14, 2015.

[92] J. Schaffner, et al. Metastable exotic multihypernuclear objects. *Phys. Rev. C*, 46:322–329, 1992.

[93] J. Schaffner, et al. Strange hadronic matter. *Phys. Rev. Lett.*, 71:1328–1331, 1993.

[94] Interaction rates of HIC experiments T. Galatyuk. https://github.com/tgalatyuk/interaction_rate_facilities/blob/main/hist_rates_detectors_2023_aug.pdf. Accessed: 2023-12-12.

[95] J. Heuser, et al., editors. *[GSI Report 2013-4] Technical Design Report for the CBM Silicon Tracking System (STS).* GSI, Darmstadt, 2013.

[96] J. Stroth et al. Technical Design Report for the CBM: Micro Vertex Detector (MVD). Technical Report 1, 2022.

[97] A. Malakhov et al., editors. *Technical Design Report for the CBM Superconducting Dipole Magnet.* GSI, Darmstadt, 2013.

[98] P. Gasik. CERN detector seminar: Towards the CBM experiment at FAIR. `https://indico.cern.ch/event/1346892/`, 2023. Accessed: 2023-12-14.

[99] Technical Design Report for the CBM Ring Imaging Cherenkov Detector. Technical report, 2013.

[100] S. Chattopadhyay, et al., editors. *Technical Design Report for the CBM : Muon Chambers (MuCh).* GSI, Darmstadt, 2015.

[101] The Transition Radiation Detector of the CBM Experiment at FAIR : Technical Design Report. Technical report, Darmstadt, 2018.

[102] N. Herrmann, editor. *Technical Design Report for the CBM Time-of-Flight System (TOF).* GSI, Darmstadt, 2014.

[103] F. Guber et al., editors. *Technical Design Report for the CBM Projectile Spectator Detector (PSD).* GSI, Darmstadt, 2015.

[104] M. Gardner. Mathematical games. *Scientific American*, 223(4):120–123, 1970.

[105] R. E. Kalman. A New Approach to Linear Filtering and Prediction Problems. *Journal of Basic Engineering*, 82(1):35–45, 03 1960.

[106] V. Akishina. *Four-dimensional event reconstruction in the CBM experiment.* PhD thesis, Goethe U., Frankfurt (Main), 2017.

[107] J. Adam et al. Particle identification in ALICE: a Bayesian approach. *Eur. Phys. J. Plus*, 131(5):168, 2016.

[108] V. Klochkov et al. Particle Identification Framework. `https://github.com/HeavyIonAnalysis/Pid`.

[109] I. Segal, et al. Using multiplicity of produced particles for centrality determination in heavy-ion collisions with the CBM experiment. *J. Phys. Conf. Ser.*, 1690(1):012107, 2020.

[110] V. Klochkov et al. Centrality Framework. `https://github.com/HeavyIonAnalysis/Centrality`.

[111] Fair Root Group. FairSoft repository. `https://github.com/FairRootGroup/FairSoft`.

[112] Fair Root Group. FairRoot repository. `https://github.com/FairRootGroup/FairRoot`.

[113] CbmRoot repository. `https://git.cbm.gsi.de/computing/cbmroot`.

[114] J. Allison et al. Geant4 developments and applications. *IEEE Trans. Nucl. Sci.*, 53:270, 2006.

[115] J. Allison et al. Recent developments in Geant4. *Nucl. Instrum. Meth. A*, 835:186–225, 2016.

[116] S. Agostinelli et al. GEANT4–a simulation toolkit. *Nucl. Instrum. Meth. A*, 506:250–303, 2003.

[117] S. Gorbunov. *On-line reconstruction algorithms for the CBM and ALICE experiments*. PhD thesis, Goethe U., Frankfurt (Main), Frankfurt U., 2013.

[118] S. Gorbunov et al. KFParticle package. `https://github.com/cbmsw/KFParticle`.

[119] M. Kretz. *Extending C++ for explicit data-parallel programming via SIMD vector types*. doctoralthesis, Universitätsbibliothek Johann Christian Senckenberg, 2015.

[120] VC library. `https://github.com/VcDevel/Vc`.

[121] M. Zyzak. *Online selection of short-lived particles on many-core computer architectures in the CBM experiment at FAIR*. PhD thesis, Goethe U., Frankfurt (Main), Frankfurt U., 2016.

[122] O. Lubynets et al. PFSimple package. https://github.com/HeavyIonAnalysis/PFSimple.

[123] V. Klochkov et al. AnalysisTree data format. https://github.com/HeavyIonAnalysis/AnalysisTree.

[124] R. Brun et al. Root – an object oriented data analysis framework. *Nuclear Instruments and Methods in Physics Research Section A: Accelerators, Spectrometers, Detectors and Associated Equipment*, 389(1):81–86, 1997. New Computing Techniques in Physics Research V.

[125] ROOT framework. https://github.com/root-project/root.

[126] V. Klochkov et al. AnalysisTree QA package. https://github.com/HeavyIonAnalysis/AnalysisTreeQA.

[127] T. Chen et al. XGBoost: A scalable tree boosting system. In *Proceedings of the 22nd ACM SIGKDD International Conference on Knowledge Discovery and Data Mining*, KDD '16, pages 785–794, New York, NY, USA, 2016. ACM.

[128] XGBoost library. https://github.com/dmlc/xgboost.

[129] S. Khan. *CBM Performance for Λ^0 Hyperon Yield Measurements Using Machine Learning Techniques*. PhD thesis, U. Tubingen, 2023.

[130] S. Khan, et al. Machine Learning Application for Λ Hyperon Reconstruction in CBM at FAIR. *EPJ Web Conf.*, 259:13008, 2022.

[131] S. Gläßel et al. *CBM Progress Report 2020*, chapter Reconstruction of hypernuclei with PFSimple, page 183. Number 2021-00421 in CBM Progress Report. GSI, Darmstadt, 2021.

[132] S. Gläßel et al. *CBM Progress Report 2022*, chapter Reconstruction of hypernuclei with PFSimple, pages 168–169. Number CBM PR 2022. GSI, Darmstadt, 2022.

[133] I. Selyuzhenkov et al. Effects of non-uniform acceptance in anisotropic flow measurement. *Phys. Rev. C*, 77:034904, 2008.

[134] R. C. Lemmon et al. Direct observation of the inversion of flow. *Phys. Lett.*

B, 446:197–202, 1999.

[135] S. Voloshin et al. Ultrarelativistic nuclear collisions: Direction of spectator flow. *Phys. Rev. C*, 94(2):021901, 2016.

[136] B. Alver et al. System size, energy, pseudorapidity, and centrality dependence of elliptic flow. *Phys. Rev. Lett.*, 98:242302, 2007.

[137] M. Luzum et al. Eliminating experimental bias in anisotropic-flow measurements of high-energy nuclear collisions. *Phys. Rev. C*, 87(4):044907, 2013.

[138] B. Efron et al. An introduction to the bootstrap. *Statist. Sci.*, 57(1):54–75, 1986.

[139] L. Kreis et al. QnTools Framework. `https://github.com/HeavyIonAnalysis/QnTools`.

[140] E. Kashirin et al. QnAnalysis Interface. `https://github.com/HeavyIonAnalysis/QnAnalysis`.

[141] J. E. Gaiser. *Charmonium Spectroscopy From Radiative Decays of the J/ψ and ψ'*. PhD thesis, Stanford University, August 1982. App. F.1, page 178.

[142] O. Lubynets et al. QnDiscriminator Framework. `https://github.com/lubynets/qn_discriminator`.

[143] R. Feynman et al. *The Feynman lectures in physics. The new millenium edition*, volume III, chapter The disintegration of the Λ^0, pages 17–21 — 17–28. Hachette Book Group, 1290 Avenue of the Americas, New York, NY 10104, 2013.

[144] S. Voloshin, et al. Collective phenomena in non-central nuclear collisions. *Landolt-Bornstein*, 23:293–333, 2010.

[145] N. Borghini, et al. Are flow measurements at SPS reliable? *Phys. Rev. C*, 62:034902, 2000.

[146] P. M. Dinh, et al. Effects of HBT correlations on flow measurements. *Phys. Lett. B*, 477:51–58, 2000.

[147] A. Bilandzic, et al. Flow analysis with cumulants: Direct calculations.

Phys. Rev. C, 83:044913, 2011.

[148] N. Borghini, et al. Effects of momentum conservation on the analysis of anisotropic flow. *Phys. Rev. C*, 66:014901, 2002.

[149] M. L. Miller, et al. Glauber modeling in high energy nuclear collisions. *Ann. Rev. Nucl. Part. Sci.*, 57:205–243, 2007.

[150] R. J. M. Snellings, et al. Novel rapidity dependence of directed flow in high-energy heavy ion collisions. *Phys. Rev. Lett.*, 84:2803–2805, 2000.

[151] J. Brachmann, et al. Antiflow of nucleons at the softest point of the EoS. *Phys. Rev. C*, 61:024909, 2000.

[152] F. Becattini, et al. Angular momentum conservation in heavy ion collisions at very high energy. *Phys. Rev. C*, 77:024906, 2008.

[153] S. M. Troshin et al. Directed flow as effect of transient matter rotation in hadron and nucleus collisions. *Int. J. Mod. Phys. E*, 17:1619–1633, 2008.

[154] K. Meehan. STAR Results from Au + Au Fixed-Target Collisions at $\sqrt{s_{NN}} = 4.5$ GeV. *Nucl. Phys. A*, 967:808–811, 2017.

[155] A. Andronic, et al. Hadron yields, the chemical freeze-out and the QCD phase diagram. *J. Phys. Conf. Ser.*, 779(1):012012, 2017.

[156] D.-X. Wei, et al. Thermal vorticity and spin polarization in heavy-ion collisions. *Phys. Rev. C*, 99(1):014905, 2019.

Zusammenfassung

Die starke Kraft ist eine der vier fundamentalen Wechselwirkungen und die zugehörige Theorie wird Quantenchromodynamik (QCD) genannt. Wichtige Aspekte beim Studium der QCD Materie sind ihre Zustandsgleichung (EoS vom englischen *equation of state*) sowie weitere Eigenschaften, wie die Kompressibilität, Viskosität und verschiedene Suszeptibilitäten. Der Bereich im QCD Phasendiagramm, wo Materie zum Vielfachen der normalen Grundzustandsdichte der Kernmaterie komprimiert wird, ist durch ein baryo-chemisches Potential μ_B von mehereren hundert MeV charakterisiert. Die Suche nach einem möglichen Phasenübergang und einem kritischen Punkt in dieser Region des Phasendiagramms ist einer der zentralen Zielsetzungen zukünftiger Forschung.

Im Labor kann ein Scan des QCD Phasendiagramms durch Schwerionenkollisionen durchgeführt werden. Die in der Überlappung der kollidierenden Atomkerne (Feuerball) erzeugte QCD Materie expandiert rapide während dem zeitlichen Fortgang der Kollision. Dabei entstehen hohe Temperaturen und Druckgradienten, extreme elektromagnetische Felder und es findet ein Austausch von Drehimpuls und dem Spin der Konstituenten des Systems statt. Aus diesen Effekten resultieren kollektive Phänomene, wie der anisotrope Fluss oder die globale Polarisation der Teilchen.

Der anisotrope Fluss wird durch die Koeffizienten v_n einer Fourierreihenentwicklung der azimuthalen Winkelverteilung der emittierten Teilchen quantitativ erfasst. Der direkte Fluss, charakterisiert durch den ersten harmonischen Koeffizienten v_1, kann Licht auf die Eigenschaften der QCD Materie und der EoS werfen. Insbesondere wird der Vorzeichenwechsel von v_1 in Schwerionenkollisionen von einigen GeV $\sqrt{s_{NN}}$ einem Aufweichen der EoS zugeschrieben und kann somit ein Beweis für einen Phasenübergang erster Ordnung sein. Der Koeffizient P_H der globalen Polarisation sondiert die Vortizität der QCD Materie und den Drehimpulsübertrag auf die Spins der erzeugten Teilchen. In Kollisionen von mehreren GeV $\sqrt{s_{NN}}$ werden Hadronen mit seltsamen Quarks nahe ihrer Produktionsschwelle erzeugt, wodurch ihre Häufigkeit sowie Emissionsanisotropie sensitiv auf die Dichte des Feuerballs sind.

Das *Compressed Baryonic Matter* (CBM) Experiment an der internationalen Teilchenbeschleunigeranlage FAIR wird Schwerionenkollisionen im Bereich $\sqrt{s_{NN}} = 2.9 - 4.9\,\mathrm{GeV}$ durchführen. Multi-differentielle Messungen der Teilchenanzahl und insbesondere der azimuthalen Modulationen (Fluss) von selten erzeugten mehrfach-seltsamen Hadronen wird durch CBM mit einer maximalen Interaktionsrate von 10^7 Hz möglich werden. Die vorliegende Dissertation präsentiert die Ergebnisse der Leistungsfähigkeit von CBM für Messungen des anisotropischen Flusses und der globalen Polarisation von $\Lambda, \bar{\Lambda}$ und mehrfach-seltsamen Ξ^- Hyperonen.

In CBM werden kurzlebige Teilchen durch ihren schwachen Zerfall rekonstruiert. Das PFSimple Softwarepaket, entwickelt im Rahmen dieser Doktorarbeit, erlaubt die Rekonstruktion von Zweikörperzerfällen (Λ, K^0_S) und Kaskaden (Ξ^-, Ω^-) sowie die Optimierung der Selektionskriterien. Abseits der Nutzung in der vorliegenden Arbeit, wurde es in der CBM Kollaboration auch schon in anderen Studien angewandt und durch [131, 132] für die Rekonstruktion von Dreikörperzerfällen erweitert, z. B. für Hypernuclei.

Unter Verwendung von GEANT4 Simulationen für das Ansprechverhalten des CBM Detektors wurde dessen Akzeptanz und Rekonstruktionseffizienz für Λ, K^0_S und Ξ^- als Funktion des transversalen Impulses und der Rapidität erzielt. Dabei wurde die höchste (4.9 GeV) und niedrigste (2.9 GeV) Kollisionsenergie studiert, die mit dem SIS-100 Beschleuniger erreichbar sind. Unter Verwendung von PF-Simple, konfiguriert für die Selektion von Zerfallskandidaten mit hohem Signal-zu-Untergrund Verhältnis (5 für Λ, 2 für K^0_S, 15 für Ξ^-), wurde gezeigt, dass die CBM Akzeptanz sowohl die Schwerpunktsrapidität als auch die vorwärtsgerichtete Rapidität im Bereich $y \in (0;1)$ bei einem tranversalen Impulsbereich von $p_T \in (0;1.5)\,\mathrm{GeV}/c$ abdeckt. Die Akzeptanz für den rückwärtsgerichteten Rapiditätsbereich hängt von der Kollisionsenergie ab und ist am größten für $\sqrt{s_{NN}} = 4.9\,\mathrm{GeV}$. Die Erfassung der Schwerpunkts- und vorwärtsgerichteten Rapidität ist für die Flussmessungen notwendig, insbesondere zur Bestimmung der Steigung dv_n/dy und des Versatzes von v_n beide bei $y = 0$. Die Erfassung des rückwärtsgerichteten Rapiditätsbereichs erlaubt eine Reduzierung der systematischen Unsicherheiten der Messungen des direkten Flusses, die durch Korrelationen mit der globalen Impulserhaltung entstehen, wobei die Antisymmetrie von v_1 als Funktionen der Rapidität genutzt wird. Die Rekonstruktionseffizienz erreicht Werte bis zu 50% für Λ und K^0_S, sowie bis zu 20% für Ξ^- in der gesamten Spannbreite an SIS-100 Kollisionsenergien. Bei $\sqrt{s_{NN}} = 4.9\,\mathrm{GeV}$ liegt das Maximum der Rekonstruktionseffizienz nahe Schwerpunktsrapidität, während bei $\sqrt{s_{NN}} = 2.9\,\mathrm{GeV}$ das Maximum zu positiven Rapiditäten von ($y \approx 1$) verschoben ist. Bei $\sqrt{s_{NN}} = 2.9\,\mathrm{GeV}$ ist die Rekonstruktionseffizienz für Schwerpunkts- und negative Rapiditäten niedrig ($\lesssim 10\%$), insbesondere im Bereich $p_T > 0.5\,\mathrm{GeV}/c$. Um die Koeffizienten des anisotropen Flusses zu bestimmen, muss die Reaktionsebene der Kollision, welche durch die Strahlachse und den Stoßparameter aufgespannt wird, angenähert werden. Dies wird über die Nukleonen gemacht, die nicht an der Kollision teilnehmen (Spektatoren). Diese werden mit einem hadronischen Kalorimeter, dem *Projectile Spectator Detektor* (PSD), registriert. Ungenauigkeiten in der Bestimmung der Reaktionsebene werden durch den Korrekturfaktor der Auflösung R_1 berücksichtigt, ausgewertet durch die Drei- und Vier-Subeventmethode. Erzeugte Teilchen und ihre Zerfallsprodukte, die in die Akzeptanz des PSD eintreten, beeinflussen den gemessenen Wert des Flusses. Die Streuung von hadronischen Schauern im Kalorimeter, transversal zur Strahlrichtung, resultiert in parasitären Korrelationen zwischen den Teilchen in der Subeventmethode. Azimuthale Ungleichmäßigkeiten der Rekonstruktionseffizienz und Effekte des magnetischen Feldes werden durch die in [133] beschriebene Prozedur korrigiert. Die Größenordnung der Korrekturen der azimuthalen Ungleichmäßigkeit bei der Rekonstruktion von Zerfällen liegt im niedrigen Prozentbereich. Die Korrekturen der PSD Ungleichmäßigkeiten sind im Bereich von mehreren Prozent in der zur in CBM verwendeten magnetischen Feld senkrechten Richtung und eine Größenordnung kleiner in der parallelen Richtung. Der Beitrag des kombinatorischen Untergrunds zum Fluss wird durch die Invariante-Massen-Fit-Methode subtrahiert. Diese wurde im Rahmen der vorliegenden Doktorarbeit als QnDiskriminator Erweiterung des Softwarepakets QnTools implementiert.

Die Koeffizienten des anisotropischen Flusses werden berechnet, indem die azimuthalen Winkel jener Teilchen korreliert werden, deren Fluss gemessenen wird mit jenen, die, in unterschiedlichen kinematischen Regionen rekonstruiert und zur Reaktionsebenenabschätzung verwendet werden. Azimuthale Korrelationen können nicht nur durch die allgemeine Anisotropie im Bezug auf die Reaktionsebene hervorgerufen werden, sondern auch durch andere physikalische Phänomene und Detektoreffekte, wie:

- Kurzreichweitige Korrelationen und Resonanzzerfälle (kein Fluss);
- Globale Transversalimpulserhaltung;
- Event-zu-Event Fluktuationen in der Position der Nukleonen (Fluktuationen des Flusses);
- Autokorrelationen hervorgerufen durch mehrere Teilchen (oder Teilchen und zugehörige Zerfallsprodukte), die in derselben Akzeptanz der verschiedenen CBM Subsysteme landen;
- Transversale Streuung von hadronischen Schauern über mehrere Module des PSD Kalorimeters.

Es ist wichtig, die Größenordnung dieser Korrelationen abzuschätzen, um die systematischen Unsicherheiten der Flussmessungen sauber zu bestimmen.

Die Drei-Subeventmethode zur Bestimmung des Korrekturfaktors der Auflösung R_1 leidet unter parasitären Korrelationen aufgrund der transversalen Streuung der hadronischen Schauer im PSD Kalorimeter, was in einer Abweichung der R_1 vom wahren, simulierten Wert resultiert. Im Falle der Vier-Subeventmethode, wo positiv geladene Pionen als viertes Subevent verwendet werden, reproduzieren die errechneten Werte von R_1 die wahren, simulierten Werte für $\sqrt{s_{NN}} = 4.9\,\mathrm{GeV}$. Aufgrund der viel breiteren Streuung der hadronischen Schauer bei $\sqrt{s_{NN}} = 2.9\,\mathrm{GeV}$, gibt es einen verbleibenden Einfluss von 10% auf die Bestimmung von R_1 in semizentralen und bis zu 40% in zentralen oder peripheren Kollisionen.

Die rekonstruierten v_1 mittels der Vier-Subeventmethode reproduzieren die MC Werte im Rahmen der statistischen Unsicherheiten im Rapiditätsbereich von $-0.5 < y < 0.7$ für $\sqrt{s_{NN}} = 4.9\,\mathrm{GeV}$, während bei $\sqrt{s_{NN}} = 2.9\,\mathrm{GeV}$ v_1 durch die Diskrepanz in der Rekonstruktion von R_1 beeinflusst sind. Die Diskrepanz bei hohen transversalen Impulsen resultiert aus Korrelationen, die nicht vom Fluss kommen, sowie der globalen Impulserhaltung. Die v_1 für vorwärtsgerichtete Rapidität und kleine Transversalimpulse werden im Fall von Λ Hyperonen überschätzt, aufgrund der Zerfallsprotonen, die in die PSD Akzeptanz fliegen. Das CBM Experiment hat eine größere Akzeptanz als der Aufbau des STAR Experiments mit festem Ziel - in der rückwärtsgerichteten Rapidität und für kleine Transversalimpulse ($p_T \lesssim 0.5\,\mathrm{GeV}/c$). Die statistischen Unsicherheiten von $v_1(y)$ werden für eine entsprechende Anzahl von Schwerionenkollisionen in CBM viel geringer erwartet als in STAR, wegen der höheren Rekonstruktionseffizienz und der größeren Akzeptanz in p_T.

Die rekonstruierten Werte des direkten Flusses für $10 - 40\%$ zentrale Ereignisse reproduzieren die MC Werte innerhalb statistischer Unsicherheiten. In anderen Zentralitätsbereichen kommt der Beitrag zur Diskrepanz von einer parasitären Korrelation zwischen den Subevents in der Bestimmung des Korrekturfaktors der Auflösung. Die Impulserhaltung führt zu einem nicht verschwindenden Achsenabschnitt des v_1 bei Schwerpunktsrapidität, welcher für hohe p_T und periphäre Kollisionen größer ist.

Die statistischen Unsicherheiten der gemessenen Steigung des direkten Flusses dv_1/dy und der gemessenen Polarisation P_H der (mehrfach-)seltsamen Hadronen werden für die erste Strahlzeit von CBM ($2 \cdot 10^{10}$ Ereignisse) abgeschätzt, für die niedrigste und höchste Kollisionsenergie des SIS-100. Die Messungen von dv_1/dy von $\bar{\Lambda}$ bei $\sqrt{s_{NN}} = 2.9\,\mathrm{GeV}$ benötigen 10^{12} Kollisionen; P_H von $\bar{\Lambda}$ und Ξ^- bei $3.3A\,\mathrm{GeV}/c$ benötigt $2 \cdot 10^{13}$, respektive 10^{13} Ereignisse. Die relative Unsicherheit wird in der Größenordnung von 25% sein, was CBM erlauben wird, einen Energiescan von dv_1/dy und P_H für (mehrfach-)seltsame Hadronen durchzuführen und experimentelle Daten zu liefern, um zwischen Modellen unter Verwendung der EoS mit und ohne Phasenübergang erster Ordnung zu unterscheiden. Die Messungen von Teilchen-Antiteilchen Unterschieden des Flusses und der Polarisation sind ebenfalls möglich, was notwendig sein wird, um die Stärke und Entwicklung des magnetischen Feldes der Schwerionenkollision zu quantifizieren.

Die erste Untersuchung der Leistungsfähigkeit von CBM für den Fluss- und die Polarisationsmessung von (mehrfach-)seltsamen Hadronen in dieser Arbeit, kann in verschiedene Richtungen erweitert werden. Erstens wird eine Untersuchung der systematischen Effekte für die multi-differentielle Flussbestimmung mit großer Statistik von Monte-Carlo Simulationen helfen, ihren Urprung zu verstehen und ihren Beitrag zu reduzieren. Zweitens ist es notwendig, die Leistungsfähigkeit von CBM mit dem *Forward Spectator Detektor* (der den PSD ersetzen wird) zu untersuchen. Mit dem FSD wird es möglich sein, Auto- und parasitäre Korrelationen zwischen Subevents zu vermeiden. Letztlich soll die Leistungsfähigkeit von CBM für Messungen anderer Flussharmoniken (v_2, v_3) von mehrfach-seltsamen Hyperonen untersucht werden.

Acknowledgements

I want to say the words of thanks to those people and organizations, without which my PhD project would not be possible. First of all I want to thank my direct supervisor and mentor, Dr. Ilya Selyuzhenkov. He kindly invited me to do doctoral project at CBM and guided my work, taught me to solve problems and formulate new ones. Instead of giving a ready answer for any physical questions Ilya pushed me to find it myself - either using external sources or doing some analytical considerations. And after that I remembered the answer much better, because it was found not for free but for the price of thinking efforts! Besides working affairs I would like to mention communication with Ilya in informal atmosphere with cup of tea that is very pleasant. Ilya, thank you very much! I am really glad to have you as my supervisor!

I am thankful to my university supervisors - Prof. Dr. Peter Senger and Prof. Dr. Christoph Blume for payed attention to my doctoral project, in particular for participation in PhD committee meetings and providing their feedback, which allowed to re-consider some aspects of the project and make it better.

I want to thank Dr. Iouri Vassiliev - my supervisor at GSI summer student program (my introduction to CBM starts at that point) - for the opportunity to realize first small scientific project and defend it.

I am thankful for experience exchange and friendship to my colleagues-friends Oleg Golosov, Evgeny Kashirin, Dr. Shahid Khan, Dr. Viktor Klochkov, Olha Lavoryk, Mikhail Mamaev and Ilya Segal (I want to emphasize Viktor for detailed explanations of features of physics analysis and programming, especially in the very beginning of my PhD study). Due to all of you guys the atmosphere in our office (and sometimes outside - in the beer garden) was really great! Our discussions organically combined different topics - from particle physics and code practices to about everything in the world, and I really enjoyed communication with you. I am looking forward to meeting with you all again!

Thanks to Dr. Frederic Linz for help with translation of the abstract and summary of my thesis into German language.

I want to mention my alma mater - Taras Shevchenko National University of Kyiv and its lecturers. Due to them I acquired strong knowledge and useful skills so necessary for scientific research. Special thanks to Prof. Dr. Stanislav Vilchynskii for invitation me to the Physics faculty and encouraging my wishes to become a physicist; to Dr. Oleg Bezshyyko and Dr. Larysa Golinka-Bezshyyko for the guidance of my scientific research and help in establishing connections with physics institutions and collaborations worldwide.

Thanks to Giersch Foundation, Goethe University and to GSI Helmholtz Centre for Heavy Ion Research for providing funding for my research project, without which it would be impossible to perform.

Thanks to everybody from CBM department and CBM collaboration whom I did not mention by name, but I am very glad that I worked with all these great people!